





DUDLEY KNOX LIBRARY  
NAVAL POSTGRADUATE SCHOOL  
MONTEREY CA 93943-5101









Approved for public release; distribution is unlimited.

A NUMERICAL STUDY OF  
INTERANNUAL WIND FORCING EFFECTS  
ON THE CALIFORNIA CURRENT SYSTEM, 1980-1983

by

Robert T. Haines  
Lieutenant, United States Coast Guard  
B. S. in Marine Science, U.S. Coast Guard Academy, 1986

Submitted in partial fulfillment of the  
requirements for the degree of

MASTER OF SCIENCE IN PHYSICAL OCEANOGRAPHY

from the

NAVAL POSTGRADUATE SCHOOL  
September, 1994

# **ABSTRACT**

A high resolution, multi-level, primitive equation ocean model is used to examine the response of an idealized, flat-bottomed, eastern boundary oceanic regime on a beta-plane to climatological average (1980-1989) and individual yearly (1980-1983) wind forcing. The focus of this study is the California Current System (CCS) along the coastal region, from  $35^{\circ}$  N to  $47.5^{\circ}$  N, of the Western United States. Five experiments were initialized from a state of rest and two from the fields remaining at day 360 from the climatological average wind forcing. With the climatological average wind forcing, a surface equatorward jet and poleward undercurrent are generated. Eddies form along the entire eastern boundary and a field of cyclonic eddies approximately 200 km in diameter remain at day 360. Results for the non-El Niño (1980-1981) years are very similar to the results for the climatological average wind forcing. Early in the year, the El Niño wind fields for 1983 are more intense than the average and 1980-1982 winds, and they have a much stronger poleward component. A surface poleward current develops over an equatorward undercurrent. After day 120 the winds have an equatorward component throughout the model domain, and eddies are generated, but the upwelling starts later and is weaker than in the non-El Niño years. When the 1980 winds are used to



REPORT DOCUMENTATION PAGE

Form Approved  
 OMB No 0704-0188

1a SECURITY CLASSIFICATION CLASSIFIED		1b RESTRICTIVE MARKINGS	
2a SECURITY CLASSIFICATION AUTHORITY		3 DISTRIBUTION / AVAILABILITY OF REPORT Approved for public release; distribution is unlimited	
2b CLASSIFICATION / DOWNGRADING SCHEDULE			
4a FORMING ORGANIZATION REPORT NUMBER(S) OC-94-003		5 MONITORING ORGANIZATION REPORT NUMBER(S)	
6a NAME OF PERFORMING ORGANIZATION Oceanography Dept. Naval Postgraduate School	6b OFFICE SYMBOL (If applicable) OC	7a NAME OF MONITORING ORGANIZATION Office of Naval Research	
7b ADDRESS (City, State, and ZIP Code) Monterey, CA 93943-5000		7c ADDRESS (City, State, and ZIP Code) 800 N. Quincy St., Arlington, VA 22217-5000	
8a NAME OF FUNDING / SPONSORING ORGANIZATION Office of Naval Research	8b OFFICE SYMBOL (If applicable)	9 PROCUREMENT INSTRUMENT IDENTIFICATION NUMBER O&MN, Direct Funding	
10a ADDRESS (City, State, and ZIP Code) 800 N. Quincy St., Arlington, VA 22217-5000		10 SOURCE OF FUNDING NUMBERS	
		PROGRAM ELEMENT NO	PROJECT NO
		TASK NO	WORK UNIT ACCESSION NO

11 ABSTRACT (Include Security Classification)  
 NUMERICAL STUDY OF INTERANNUAL WIND FORCING EFFECTS ON THE CALIFORNIA CURRENT SYSTEM, 1980-1983 (U)

12 AUTHOR(S) Robert T. Haines in conjunction with M.L. Batteen			
13a TITLE OF REPORT Robert's Thesis	13b TIME COVERED FROM _____ TO _____	14. DATE OF REPORT (Year, Month, Day) 1994 SEP	15 PAGE COUNT 138

16 REMARKS / NOTES  
 Views expressed in this thesis are those of the author and do not reflect the official policy or position of the Department of Defense or the United States Government.

COSATI CODES			18 SUBJECT TERMS (Continue on reverse if necessary and identify by block number) Primitive equation model, eddies, filaments, wind forcing, coastal jet and undercurrent, El Nino, California Current System
19a D	19b GROUP	19c SUB-GROUP	

19 ABSTRACT (Continue on reverse if necessary and identify by block number)  
 High resolution, multi-level, primitive equation ocean model is used to examine the response of an idealized, flat-bottomed, eastern boundary oceanic regime on a beta-plane climatological average (1980-1989) and individual yearly (1980-1983) wind forcing. Focus of this study is the California Current System (CCS) along the coastal region, 35°N to 47.5°N, of the Western United States. Five experiments were initialized at a state of rest and two from the fields remaining at day 360 from the climatological average wind forcing. With the climatological average wind forcing, a surface equatorward and poleward undercurrent are generated. Eddies form along the entire eastern boundary and a field of cyclonic eddies approximately 200 km in diameter remain at day 360. Results for the non-El Nino (1980-1981) years are very similar to the results for the climatological average wind forcing. Early in the year, the El Nino wind fields for 1982 are more intense than the average and 1980-1982 winds, and they have a much larger poleward component. A surface poleward current develops over an equatorward

20 DISTRIBUTION / AVAILABILITY OF ABSTRACT CLASSIFIED/UNLIMITED <input type="checkbox"/> SAME AS RPT <input type="checkbox"/> DTIC USERS		21 ABSTRACT SECURITY CLASSIFICATION UNCLASSIFIED	
22a NAME OF RESPONSIBLE INDIVIDUAL L. Batteen		22b TELEPHONE (Include Area Code) (408) 656-3265	22c OFFICE SYMBOL OC/Bv

1473, JUN 86

Previous editions are obsolete  
 S/N 0102-LF-014-6603

SECURITY CLASSIFICATION OF THIS PAGE  
 UNCLASSIFIED

19) undercurrent. After day 120 the winds have an equatorward component throughout the model domain, and eddies are generated, but the upwelling starts later and is weaker than in the non-El Nino years. When the 1980 winds are used to force with the fields left at day 360 from the climatological average wind forcing as initial conditions, the current and eddy system generated is more similar to CCS observations than the results of the experiments initialized from rest. Cold filaments form at the coast and extend to more than 400 km offshore. With the 1983 winds initialized from the climatological results, more poleward flow is seen at the surface early in the year. Cold filaments still develop, but later in the year and they do not extend as far offshore as in 1980. The overall current and eddy system is weaker and sea surface temperatures are warmer than in 1980. This leads to the conclusion that anomalous wind forcing is extremely important in generating CCS El Nino events.

force with the fields left at day 360 from the climatological average wind forcing as initial conditions, the current and eddy system generated is more similar to CCS observations than the results of the experiments initialized from rest. Cold filaments form at the coast and extend to more than 400 km offshore. With the 1983 winds initialized from the climatological results, more poleward flow is seen at the surface early in the year. Cold filaments still develop, but later in the year and they do not extend as far offshore as in 1980. The overall current and eddy system is weaker and sea surface temperatures are warmer than in 1980. This leads to the conclusion that anomalous wind forcing is extremely important in generating CCS El Niño events.

## TABLE OF CONTENTS

I.	INTRODUCTION.....	1
II.	BACKGROUND.....	3
	A. REGIONAL DESCRIPTION.....	3
	B. CLIMATOLOGICAL WINDS.....	6
	C. EL NIÑO.....	8
	D. NUMERICAL MODEL STUDIES.....	10
III.	MODEL DESCRIPTION.....	25
	A. MODEL EQUATIONS.....	25
	B. MODEL DOMAIN AND RESOLUTION.....	29
	C. FINITE DIFFERENCE SCHEME.....	30
	D. HEAT AND MOMENTUM DIFFUSION.....	30
	E. SURFACE THERMAL FORCING.....	31
	F. HORIZONTAL BOUNDARY CONDITIONS.....	31
	G. INITIAL CONDITIONS.....	32
	H. WIND DATA DESCRIPTION.....	33
	I. EXPERIMENTAL DESIGN.....	34
	J. ENERGY ANALYSIS TECHNIQUES.....	35
IV.	EXPERIMENT RESULTS.....	39
	A. RESULTS OF EXPERIMENTS STARTED FROM REST.....	39
	1. Experiment 1.....	39
	2. Experiments 2, 3 and 4.....	42
	3. Experiment 5.....	42

B.	RESULTS OF EXPERIMENTS SPUN UP FROM CLIMATOLOGICAL WINDS.....	44
1.	Experiment 6.....	44
2.	Experiment 7.....	46
C.	COMPARISON OF RESULTS WITH OBSERVATIONS OF THE CCS.....	47
V.	SUMMARY AND RECOMMENDATIONS.....	100
A.	SUMMARY.....	100
B.	RECOMMENDATIONS.....	101
	APPENDIX A: FIGURES FROM EXPERIMENTS 2, 3 AND 4.....	103
	LIST OF REFERENCES.....	118
	INITIAL DISTRIBUTION LIST.....	123



## LIST OF TABLES

Table 3.1 VALUES OF CONSTANTS USED IN THE MODEL .....	39
Table 4.1 INSTANTANEOUS COMPARISON OF EXPERIMENTS (EXP) WITH OBSERVATIONS (OBS) OF THE CCS.....	49
Table 4.2 COMPARISON OF OBSERVED (OBS) AND MODEL EXPERIMENT (EXP) QUALITATIVE CCS FEATURES SEEN DURING EL NIÑO YEARS..	50

## LIST OF FIGURES

Figure 2.1 Infrared satellite image of CCS from 18 June, 1993.....	14
Figure 2.2 Long-term mean atmospheric pressure at sea level for January and July (from Huyer, 1983).....	15
Figure 2.3 Climatological wind stress for June (from Nelson, 1977).....	16
Figure 2.4 Climatological wind stress for July (from Nelson, 1977).....	17
Figure 2.5 Climatological wind stress for August (from Nelson, 1977)....	18
Figure 2.6 Climatological wind stress curl for June (from Nelson, 1977).	19
Figure 2.7 Climatological wind stress curl for July (from Nelson, 1977).	20
Figure 2.8 Climatological wind stress curl for August (from Nelson, 1977). .....	21
Figure 2.9 Average distribution of atmospheric pressure at sea level during the winter seasons, December to February inclusive, of 1955-56 and 1956-57, before the East Pacific equatorial warming, and 1957-58 at the peak of that warming (from Bjerkness, 1966).....	22
Figure 2.10 A schematic diagram of the Pacific North American (PNA) pattern of middle- and upper-tropospheric geopotential height anomalies during a Northern Hemisphere winter that coincides with El Niño conditions in the tropical Pacific (from Philander, 1990).....	23
Figure 2.11 Latitude-time sections of the monthly mean wind stress from 1980 to 1986 eastward component zonally averaged for the Pacific Ocean: (a) total, contour 0.5 dyn cm <sup>2</sup> ; and (b) departures from the mean annual cycle, contour 0.25 dyn cm <sup>2</sup> . Negative values are stippled (from Trenberth et al., 1990).....	24
Figure 4.1a) Experiment 1: Wind forcing in m s <sup>-1</sup> at day 60.....	51
Figure 4.1b) Experiment 1: Wind forcing in m s <sup>-1</sup> at day 120.....	52
Figure 4.1c) Experiment 1: Wind forcing in m s <sup>-1</sup> at day 180.....	53
Figure 4.1d) Experiment 1: Wind forcing in m s <sup>-1</sup> at day 240.....	54
Figure 4.1e) Experiment 1: Wind forcing in m s <sup>-1</sup> at day 300.....	55
Figure 4.2a) Experiment 1: Surface velocity at day 60.....	56
Figure 4.2b) Experiment 1: Surface temperature at day 60.....	57
Figure 4.3 Experiment 1: Surface zonal velocity at day 120.....	58
Figure 4.4 Experiment 1: Surface temperature at day 144.....	59
Figure 4.5 Experiment 1: Cross-section of velocity at day 120.....	60
Figure 4.6a) Experiment 1: Surface temperature at day 285.....	61

Figure 4.6b) Experiment 1: Surface dynamic height at day 285.....	62
Figure 4.6c) Experiment 1: Surface zonal velocity at day 285.....	63
Figure 4.7a) Experiment 1: Baroclinic energy transfer days 120-126.....	64
Figure 4.7b) Experiment 1: Barotropic energy transfer days 120-126.....	65
Figure 4.8 Experiment 1: Barotropic energy transfer days 345-351.....	66
Figure 4.9 Experiment 1: Cross-section of velocity at day 345.....	67
Figure 4.10 Experiment 1: Surface zonal velocity at day 345.....	68
Figure 4.11a) Experiment 5: Wind forcing in $\text{m s}^{-1}$ at day 60.....	69
Figure 4.11b) Experiment 5: Wind forcing in $\text{m s}^{-1}$ at day 90.....	70
Figure 4.11c) Experiment 5: Wind forcing in $\text{m s}^{-1}$ at day 120.....	71
Figure 4.11d) Experiment 5: Wind forcing in $\text{m s}^{-1}$ at day 180.....	72
Figure 4.11e) Experiment 5: Wind forcing in $\text{m s}^{-1}$ at day 240.....	73
Figure 4.11f) Experiment 5: Wind forcing in $\text{m s}^{-1}$ at day 300.....	74
Figure 4.12a) Experiment 5: Surface zonal velocity at day 66.....	75
Figure 4.12b) Experiment 5: Surface temperature at day 66.....	76
Figure 4.12c) Experiment 5: Surface velocity at day 66.....	77
Figure 4.12d) Experiment 5: Surface dynamic height at day 66.....	78
Figure 4.13a) Experiment 5: Baroclinic energy transfer days 66-72.....	79
Figure 4.13b) Experiment 5: Barotropic energy transfer days 66-72.....	80
Figure 4.14 Experiment 5: Cross-section of velocity at day 66.....	81
Figure 4.15a) Experiment 5: Surface zonal velocity at day 159.....	82
Figure 4.15b) Experiment 5: Surface dynamic height at day 159.....	83
Figure 4.16) Experiment 5: Cross-section of velocity at day 159.....	84
Figure 4.17a) Experiment 5: Baroclinic energy transfer days 159-165.....	85
Figure 4.17b) Experiment 5: Barotropic energy transfer days 159-165.....	86
Figure 4.18 Experiment 6: Surface zonal velocity at day 60.....	87
Figure 4.19a) Experiment 6: Baroclinic energy transfer days 60-66.....	88
Figure 4.19b) Experiment 6: Barotropic energy transfer days 60-66.....	89
Figure 4.20 Experiment 6: Surface velocity at day 60.....	90

Figure 4.21 Experiment 6: Cross-section of velocity at day 60.....	91
Figure 4.22a) Experiment 6: Surface temperature at day 150.....	92
Figure 4.22b) Experiment 6: Surface velocity at day 150.....	93
Figure 4.23 Experiment 7: Cross-section of velocity day 66.....	94
Figure 4.24a) Experiment 7: Baroclinic energy transfer days 66-72.....	95
Figure 4.24b) Experiment 7: Barotropic energy transfer days 66-72.....	96
Figure 4.25 Experiment 7: Surface velocity at day 66.....	97
Figure 4.26a Experiment 7: Surface temperature at day 150.....	98
Figure 4.27b) Experiment 7: Surface velocity at day 150.....	99
Figure A.1 Experiment 2: Surface velocity at day 90.....	103
Figure A.2 Experiment 2: Surface temperature at day 90.....	104
Figure A.3 Experiment 2: Surface zonal velocity at day 90.....	105
Figure A.4 Experiment 2: Baroclinic energy transfer days 90-96.....	106
Figure A.5 Experiment 2: Barotropic energy transfer days 90-96.....	107
Figure A.6 Experiment 3: Surface velocity at day 99.....	108
Figure A.7 Experiment 3: Surface temperature at day 99.....	109
Figure A.8 Experiment 3: Surface zonal velocity at day 99.....	110
Figure A.9 Experiment 3: Baroclinic energy transfer days 96-102.....	111
Figure A.10 Experiment 3: Barotropic energy transfer days 96-102.....	112
Figure A.11 Experiment 4: Surface velocity at day 114.....	113
Figure A.12 Experiment 4: Surface temperature at day 114.....	114
Figure A.13 Experiment 4: Surface zonal velocity at day 114.....	115
Figure A.14 Experiment 4: Baroclinic energy transfer days 114-120.....	116
Figure A.15 Experiment 4: Barotropic energy transfer days 114-120.....	117

## ACKNOWLEDGMENTS

The author wishes to thank Dr. Mary Batteen for her patience and guidance, especially in helping to finish and process this report after departing NPS early. Her expertise in both oceanography and writing scientific papers helped to ease the way and made this a valuable learning experience. Thanks also to Dr. Collins and Dr. Bourke for their encouragement and assistance in finalizing this report from a distance. The many hours of assistance in computer programming and debugging by Pedro Tsai was invaluable to the completion of this thesis and are very gratefully acknowledged. Finally, I would like to thank my wife, Catherine, and my son, Tristan for their support and understanding over these past two years.



## I. INTRODUCTION

The California Current System (CCS) is a complex system of eddies and meandering jets superimposed on a mean equatorward surface flow which extends approximately 1000 km westward from the coast. There have been several major observational experiments focusing on the CCS in the past decade, including the Coastal Upwelling Experiments (CUE-I and CUE-II), Coastal Ocean Dynamics Experiment (CODE), Ocean Prediction through Observations, Modeling and Analysis (OPTOMA), and Coastal Transition Zone (CTZ).

In order to get an accurate picture of the mesoscale variability of the CCS, an observational experiment requires a very fine (~25-50 km) mesh covering most of the west coast of the United States, a prohibitively expensive endeavor. In this light, much of the current work on the CCS consists of attempts to model the features seen in the extensive observational experiments that have already been conducted. Batteen et al. (1989) demonstrated how a steady equatorward wind forcing a non-linear primitive equation (PE) model could generate a reasonable coastal equatorward jet, poleward undercurrent and eddy field similar to the CCS. This study extends their process-oriented work by forcing the same model with yearly instead of steady winds. It is designed to explain the role of interannual variability in wind-forced generation

of the eddies and filaments that have been observed in the CCS. Yearly winds from 1980 through 1983 are used in the study. This particular period of time is chosen in order to also examine the response of the CCS to changes in wind forcing during an El Niño event. In addition, a set of climatological average winds from the period 1980-1989 is used to force the model, in order to generate a baseline average CCS and to spin up the model for two experiments.

This thesis is organized as follows. Chapter II describes the background for the region being modeled as well as the type of winds used to force the model. It also briefly discusses some models used in the past to simulate eastern boundary current systems. Chapter III describes the model and the experimental design. Results are presented in Chapter IV. Chapter V consists of a summary of the results, conclusions and recommendations for future work.

## II. BACKGROUND

### A. REGIONAL DESCRIPTION

The California Current System (CCS) is a classical eastern boundary current system. The climatological mean CCS consists of four currents: the California Current, the Davidson Current, the California Undercurrent and the Southern California Countercurrent (Hickey, 1979). The California Current (CC) is a broad, slow ( $\sim 10 \text{ cm s}^{-1}$ ) surface equatorward flow that can extend 1000 km offshore. It represents the eastern limb of the North Pacific gyre (Lynn and Simpson, 1987), and is driven by the semi-permanent North Pacific High (Huyer, 1983). It is a shallow (300 m) current, characterized by low temperature, low salinity and high dissolved oxygen (Lynn and Simpson, 1987). The core of the CC is located between 100-200 km from the coast, with average current speeds of less than  $25 \text{ cm s}^{-1}$ , but core velocities in excess of  $75 \text{ cm s}^{-1}$  have been observed (Brink et al., 1991).

It is generally recognized that flow within 100 km of the coast is part of a separate current (Chelton, 1984; Hickey, 1979). This current is notable in its seasonable variability. From February to September it flows equatorward, and merges with the CC flow. From November to February, however, the current reverses direction and flows poleward in the region between Pt. Conception and Cape Mendocino (Hickey, 1979).

During its poleward phase it is known as the Davidson Current (Chelton, 1984; Hickey, 1979). It should be emphasized that this picture of the nearshore flow is true only in the interannual mean sense, and northward flow has been observed during all months of the year (Chelton *et al.*, 1988; Freitag and Halpern, 1981).

The third major current in the CCS is the poleward flowing California Undercurrent (CU). The CU is found over the continental shelf, usually near the shelf break, at an average depth of 200-250 m, with a vertical extent of approximately 300 m (Wickham *et al.*, 1987; Hickey, 1979). The flow varies in width from 20-70 km (Hickey, 1979; Reid, 1962). The average core velocity is greater than  $15 \text{ cm s}^{-1}$ , with instantaneous observations over  $40 \text{ cm s}^{-1}$  (Hickey, 1979; Reid, 1962). As the CU progresses poleward it appears to strengthen, and has a vertical extent in excess of 500 m off the Washington coast (Reed and Halpern, 1976). In the wintertime the CU shoals and merges with the Davidson Current and poleward flow is seen from the surface to the bottom over the continental shelf (Huyer *et al.*, 1989).

The Southern California Countercurrent (SCC) is an area of semi-permanent eddy-like circulation in the California Bight, and appears to be formed by wind patterns off Pt. Conception and bottom topography in the area (Lynn and Simpson, 1987). This current is south of the area modeled in this study and will not be discussed further.

Recent observations have shown that the CCS is more appropriately described by a series of highly energetic mesoscale eddies, meandering jets and filaments superimposed on the classical broad, slow surface equatorward current (Bernstein et al., 1977; Chelton, 1984; Mooers and Robinson, 1984). Irregularities in the CCS flow were noted as early as 1950 (Reid, 1988), but it took the advent of satellite technology to truly appreciate the variability of the CCS (Fig. 2.1). The core of the CC takes on the form of a meandering jet, with wavelengths of 300-500 km (Bernstein et al., 1977). The meanders are associated with cyclonic and anticyclonic eddy pairs, and with cold filaments extending away from the coast. The filaments can extend up to several hundred kilometers offshore, with widths of 30 km and temperature changes of 1-3°C across their boundaries (Bernstein et al., 1977). Peak current speeds in the filaments have been measured at 80 cm s<sup>-1</sup> (Kosro and Huyer, 1986). These features add up to a more realistic description of the CCS as a constantly evolving system of currents with filamented jets and mesoscale eddies modifying the mean equatorward flow (Mooers and Robinson, 1984).



## B. CLIMATOLOGICAL WINDS

Interaction between the North Pacific High and the southwest United States thermal low (Fig. 2.2) establishes the summer wind patterns seen in the CCS (Nelson, 1977; Halliwell and Allen, 1987). The wind regime is complicated on shorter scales by interaction with atmospheric disturbances propagating through the area (Halliwell and Allen, 1987), and with other atmospheric mesoscale phenomena (Huyer, 1983). Within 100-200 km of the shore, the winds are also affected by coastal atmospheric boundary layer processes, resulting in measured wind fluctuations strongly polarized in the alongshore direction (Halliwell and Allen, 1987).

The climatological average summer wind stress near the shore is equatorward, and thus is favorable for coastal upwelling. An alongshore wind stress time series compiled over nine years by Strub et al. (1987) clearly depicts the dominance of equatorward wind stress during the summer. Halpern (1976) found similar conditions of equatorward wind stress during July and August in a study conducted off the coast of Oregon. Climatological wind stress fields for the months of June, July and August (Figs. 2.3, 2.4, and 2.5, respectively) show the regions of maximum wind stress (shaded) that extend along the California coast from Cape Mendocino to Point Conception. The maximum in wind stress is located off Point Conception in March (not shown), and migrates to the north as the North Pacific High moves northward, reaching Cape

Mendocino in June (Fig. 2.3) or July (Fig. 2.4). In the winter (Fig. 2.2), the Aleutian Low moves to the southeast, and there is a split in the winds near Cape Mendocino (approximately  $40^{\circ}\text{N}$ ), with poleward winds to the north of the Cape and equatorward winds to the south.

Smith (1968) showed that open ocean upwelling can occur if there is positive wind stress curl away from a coast. There is positive wind stress curl at the west coast during all months of the year, with the strongest curl occurring from May to September (Nelson, 1977; Halpern, 1976). Wind stress curl fields for the months of June, July and August (Figs. 2.6, 2.7, and 2.8, respectively) show the shift from positive wind stress curl near the coast to negative curl farther offshore. The transition zone, located approximately 200-300 km offshore, is associated with the offshore maximum of the alongshore wind stress. Bakun and Nelson (1991) found that the cyclonic curl nearshore leads to divergent Ekman surface transport, upward Ekman pumping, oceanic upwelling and poleward Sverdrup flow. In the offshore (anticyclonic curl) region, they found convergent Ekman transport, downward Ekman pumping and equatorward Sverdrup flow.

The importance of wind stress and wind stress curl in the current dynamics and upwelling of the CCS is well documented (e.g., Huyer, 1983; Nelson, 1977; Chelton, 1984; Hickey, 1979). Edson (1989) found that when the wind stress curl is dominant over the wind stress itself, as in the wintertime, a

surface poleward flow develops nearshore, with equatorward flow offshore. When the wind stress is dominant, as in the summertime, a coastal surface jet develops over a poleward undercurrent. Wind stress data have been correlated with satellite infrared imagery of eddies and filaments, illustrating the possible importance of wind stress in these mesoscale processes (Wickham et al., 1987). Other modeling studies have supported this idea, and the thrust of this research is to continue to study the role of wind forcing in eddy and jet formation, focusing on the interannual variability of monthly mean wind stress fields.

### C. EL NIÑO

The El Niño/Southern Oscillation (ENSO) phenomenon has been extensively studied for many years. It has long been recognized that an equatorial El Niño signal can propagate from the tropics northward to the northeastern Pacific Ocean. There are two possible teleconnections between these two regions. The first is an oceanic teleconnection, consisting of poleward propagating coastal Kelvin waves that are generated when the eastward traveling equatorial Kelvin waves turn poleward at the South American coast (Rienecker and Mooers, 1986).

The second teleconnection is an atmospheric one, where tropical sea surface temperature (SST) anomalies are linked to the Aleutian Low by momentum transfer through an intensified

Hadley circulation (Bjerknes, 1966; Philander, 1990). The Aleutian Low deepens and moves to the southeast, displacing the North Pacific High, which moves offshore and weakens (Figs. 2.9, 2.10). This results in strong poleward wind stress at the coast north of approximately  $36^{\circ}\text{N}$ . Trenberth et al. (1990) found that the Aleutian Low was much deeper than normal in the winter of 1982-1983, and that the maximum positive wind stress anomalies were seen between  $35^{\circ}$  and  $45^{\circ}\text{N}$  (Fig. 2.11). Simpson (1983) concluded that the 1982-83 Californian El Niño was probably linked to the concurrent equatorial El Niño mainly through the atmospheric teleconnection. (This study isolates the response of the CCS to changes in wind forcing only, and should show at least the qualitative response of the CCS to the changes in atmospheric forcing during the 1982-1983 El Niño.)

The 1982-1983 El Niño was perhaps the most intense El Niño observed during this century. SST anomalies were first seen in autumn 1982 off the California coast, increasing to a positive peak in March-April 1983 (Rienecker and Mooers, 1986). The properties of the anomalous water mass along the California coast indicate that it came from the south and west, and was associated with onshore transport. Thus the 1982-1983 California El Niño could not have been solely due to the poleward propagation of coastal trapped waves, as they have no cross-shore component of velocity (Simpson, 1984). Negative subsurface salinity anomalies in the same time period could



have been caused either by depression of the thermocline due to the offshore propagation of Rossby waves, or to increased onshore advection from the anomalous wind fields. This indicates that the El Niño signal seen off California is at least partly due to the anomalous atmospheric forcing. The wind fields used in this study show strong poleward winds over the entire model domain for the first three months of 1983 (Fig. 4.11a), consistent with a picture of enhanced onshore advection due to Ekman veering.

#### **D. NUMERICAL MODEL STUDIES**

Over the past 25 years, there have been numerous attempts at modeling eastern boundary current systems, and the CCS in particular has been the focus of many modeling studies. A brief discussion of some of the more relevant studies follows.

Philander and Yoon (1982) studied the response of an eastern boundary current system to equatorward curl-free winds that varied on a period related to that of both Rossby waves and coastal trapped (Kelvin) waves moving through the current system. They found that at wind fluctuations with a period between that of a Kelvin wave and a Rossby wave, the current response was trapped within a baroclinic radius of deformation (~30 km at our study latitude) of the coast. When the wind fluctuations were of a longer period than that of Rossby waves (200 days), the offshore length scale increased to the



distance a Rossby wave could travel in that period of time, and the resultant current system resembled that of the CCS.

McCreary et al. (1987) forced two linear models, one with a flat bottom and the other with an idealized continental shelf, with various wind fields. Steady, equatorward, curl-free winds resulted in an equatorward surface jet and a poleward undercurrent. Steady, equatorward winds with positive curl developed a deep, broad poleward surface current near the coast, as predicted by Sverdrup theory. This experiment also generated equatorward flow farther offshore, but still in the region with positive wind curl. An idealized form of the observed wind fields off California resulted in a modeled CCS that agreed well with observations, but only if the forcing included remote winds off Baja California (outside the region being modeled). The results of this experiment suggested that the Davidson Current is a result of the wind stress curl dominating in the winter time, and the equatorward jet and poleward undercurrent are generated when the wind stress is stronger than the curl. Their model used Laplacian diffusion, and did not develop eddies or filaments.

Batteen et al. (1989) used a primitive equation, multi-level model with biharmonic heat and momentum diffusion, and the wind forcing again was steady and equatorward, with or without alongshore variability. As before, the constant wind stress resulted in an equatorward jet overlying a poleward undercurrent. The biharmonic diffusion allowed the development

of eddies and filaments when the baroclinic shear between the jet and the undercurrent became strong enough. The winds that varied in the alongshore direction led to preferential geographic areas for eddy/filament generation. No experiments were run with winds that contained a wind stress curl component.

Pares-Sierra and O'Brien (1989) forced a reduced gravity model with either wind stress, remote forcing from results from an equatorial model, or both. Their objective was to examine the oceanic connection between the CCS and the equatorial region, and also to investigate the relative dominance of either the atmospheric or oceanic teleconnection in an El Niño event. They found that most of the interannual variability in sea level at the coast is determined by the remote forcing, while the seasonal variability is due to local wind forcing. This suggests that the oceanic teleconnection is mainly responsible for the propagation of equatorial El Niño events up the coast.

Mitchell (1993) continued the work of Batteen *et al.* (1989) by forcing that model with different sets of temporally and/or spatially averaged winds. He found that the most realistic results were obtained by forcing the model with a set of full climatological, seasonally varying wind fields.

This study will extend the work of Batteen *et al.* (1989) and Mitchell (1993) by enlarging the model domain from ~500 x 1000 km to ~1000 x 1500 km, and forcing the model with

interannual rather than steady or seasonal wind forcing. Even though the model domain is almost doubled, the resolution is similar (8 x 13 km versus 8 x 17 km for Mitchell). Winds before and during the 1982-83 El Niño event were chosen for the study. The study period encompasses a time of abnormally large interannual variability, and is well suited to observing the CCS response to those changes. In addition, it is anticipated that the El Niño signature due to the atmospheric teleconnection will be observed in the 1982 and 1983 experiments.



18 June, 1993  
12Z

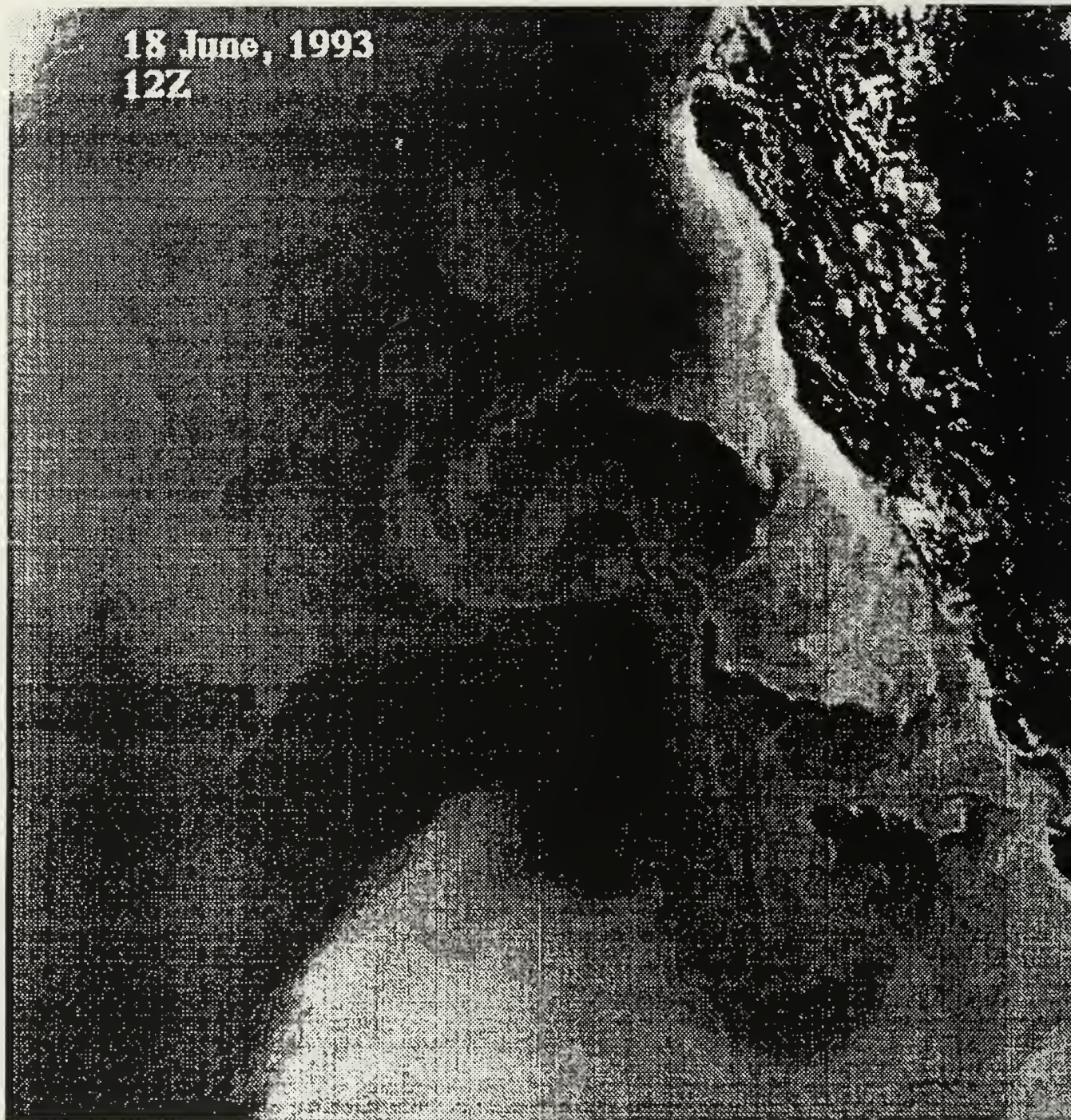


Figure 2.1: Infrared satellite image of CCS from 18 June, 1993, extending from approximately 36°-40°N Latitude, 121°-128°W Longitude

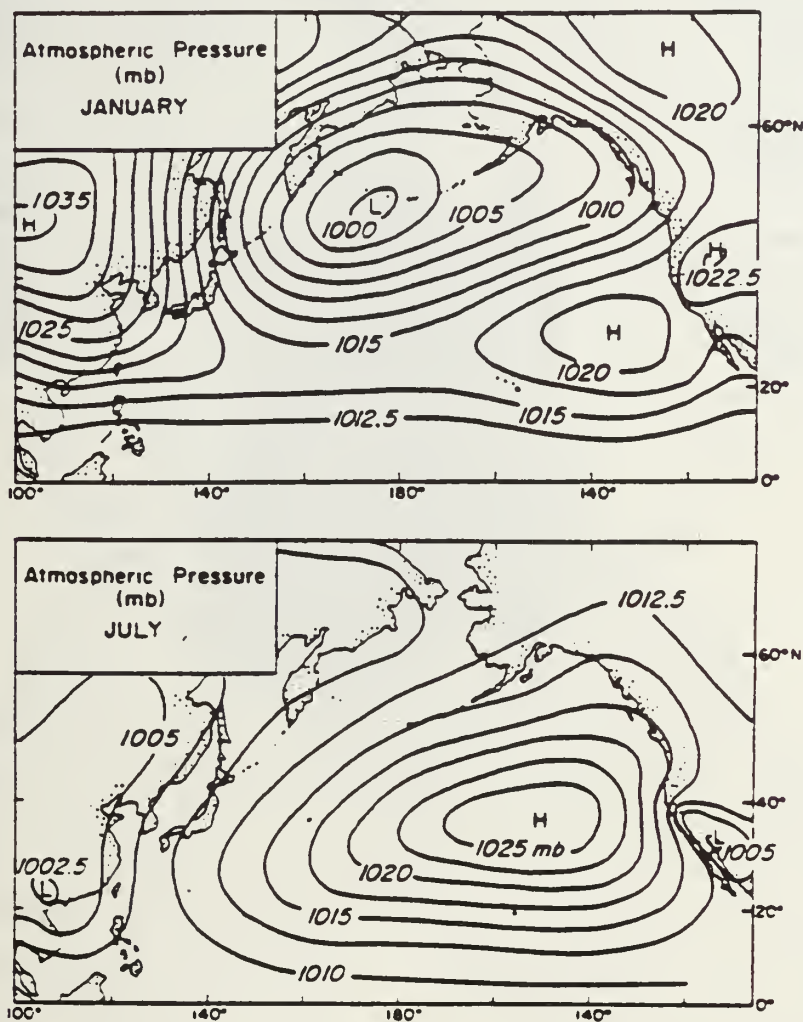


Figure 2.2) Long-term mean atmospheric pressure at sea level for January and July (from Huyer, 1983).



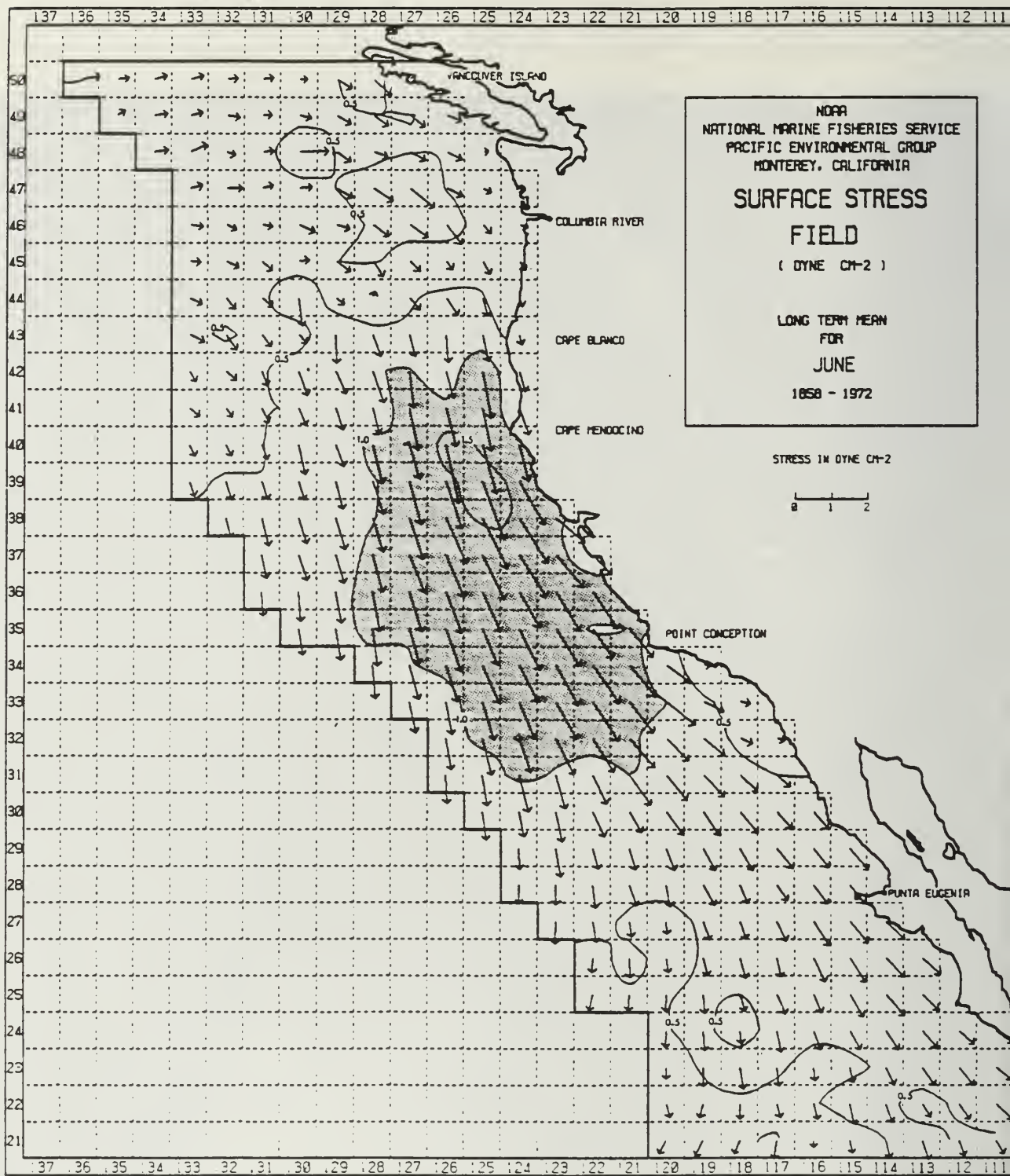


Figure 2.3) Climatological wind stress vectors for June (from Nelson, 1977).

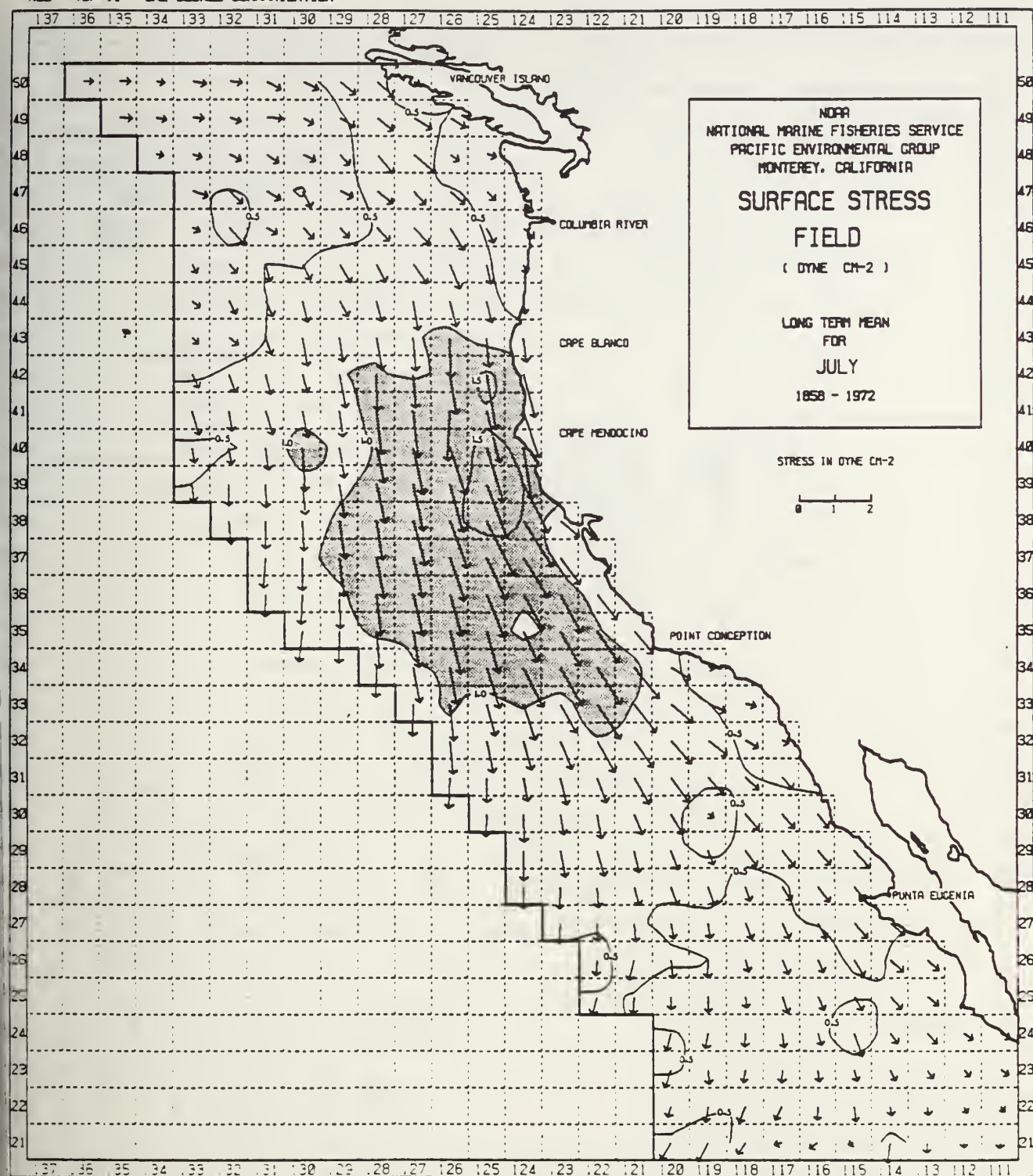


Figure 2.4) Climatological wind stress vectors for July  
(from Nelson, 1977).

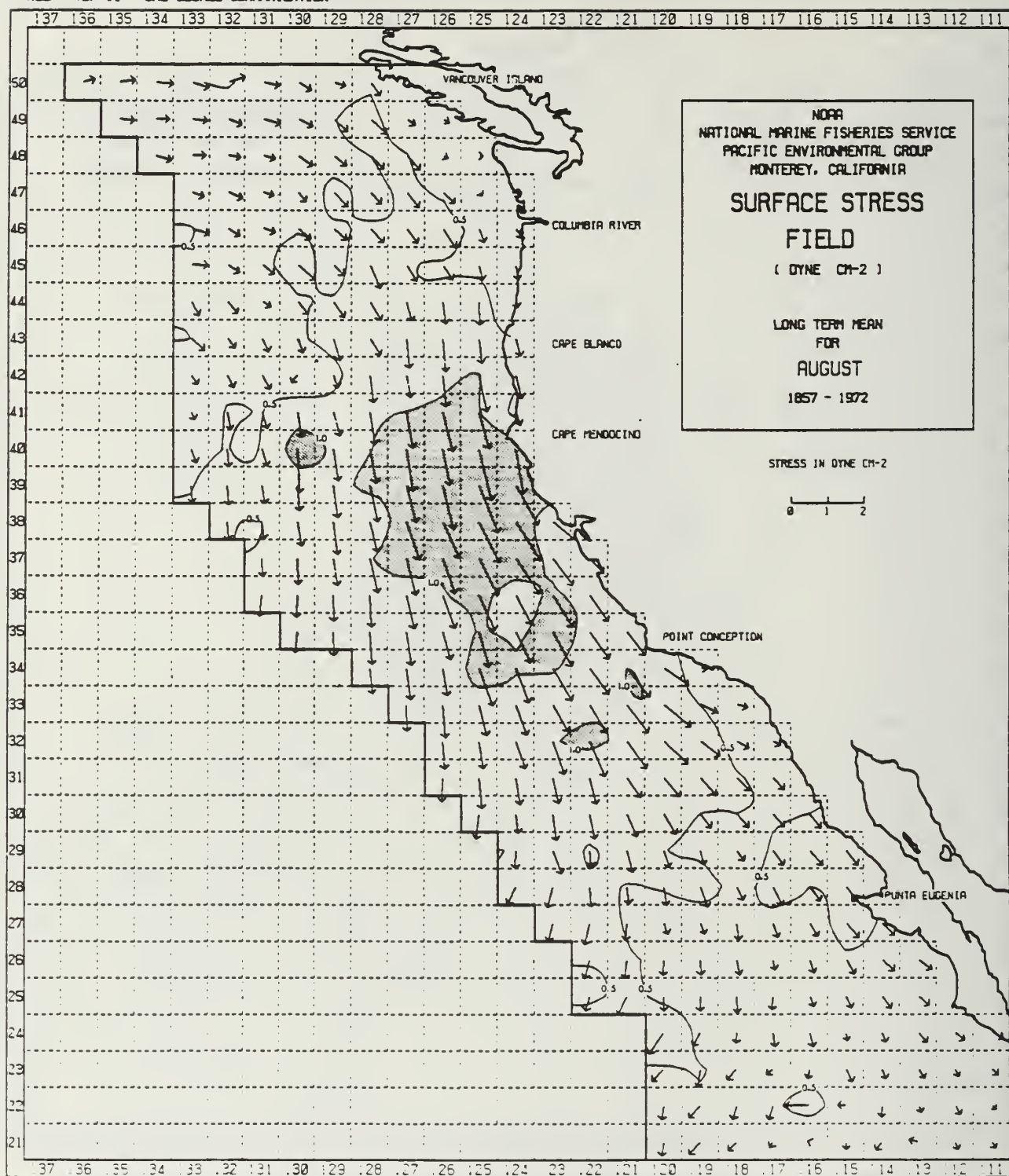


Figure 2.5) Climatological wind stress vectors for August  
(from Nelson, 1977)



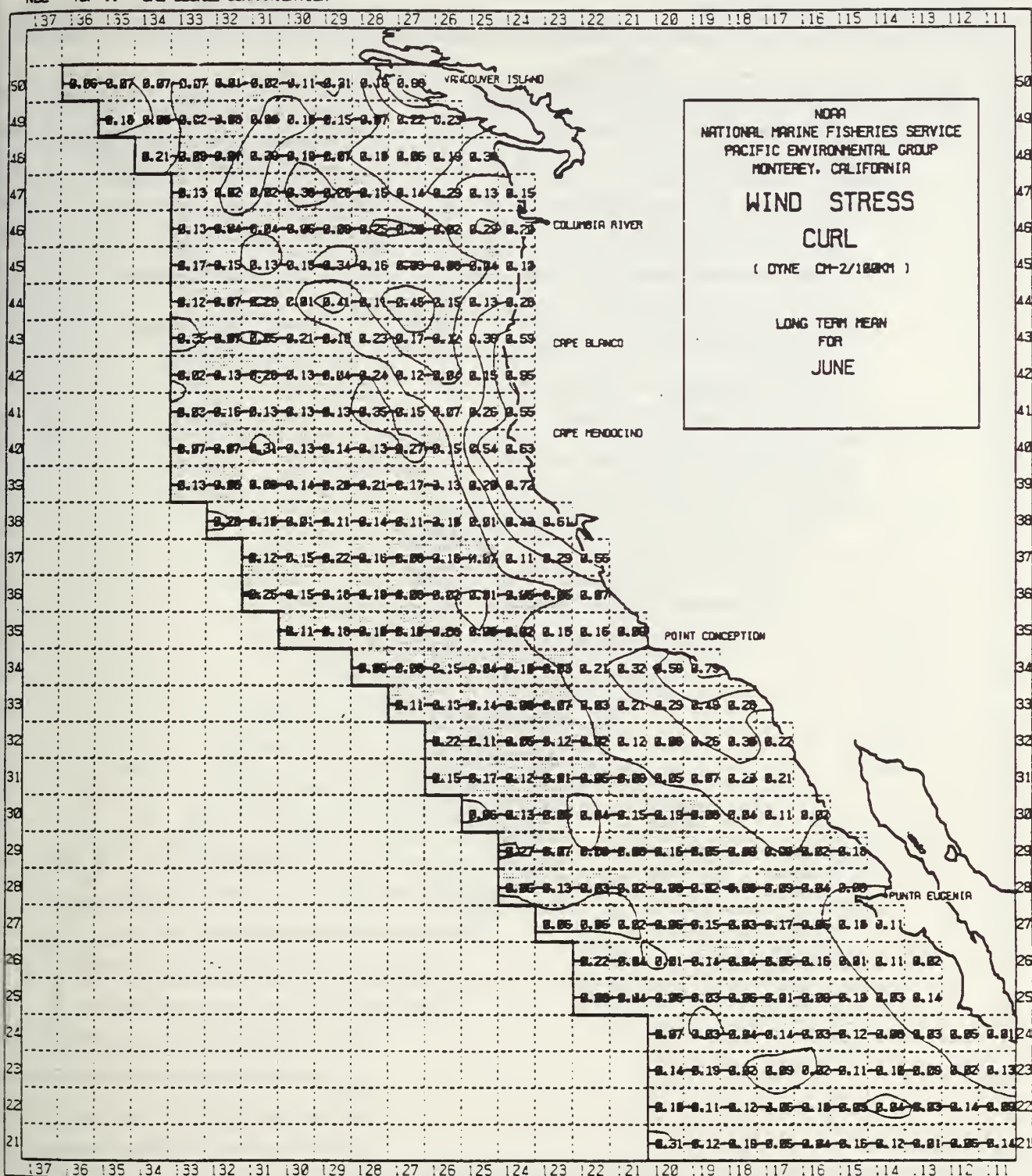


Figure 2.6) Climatological wind stress curl for June (from Nelson, 1977).

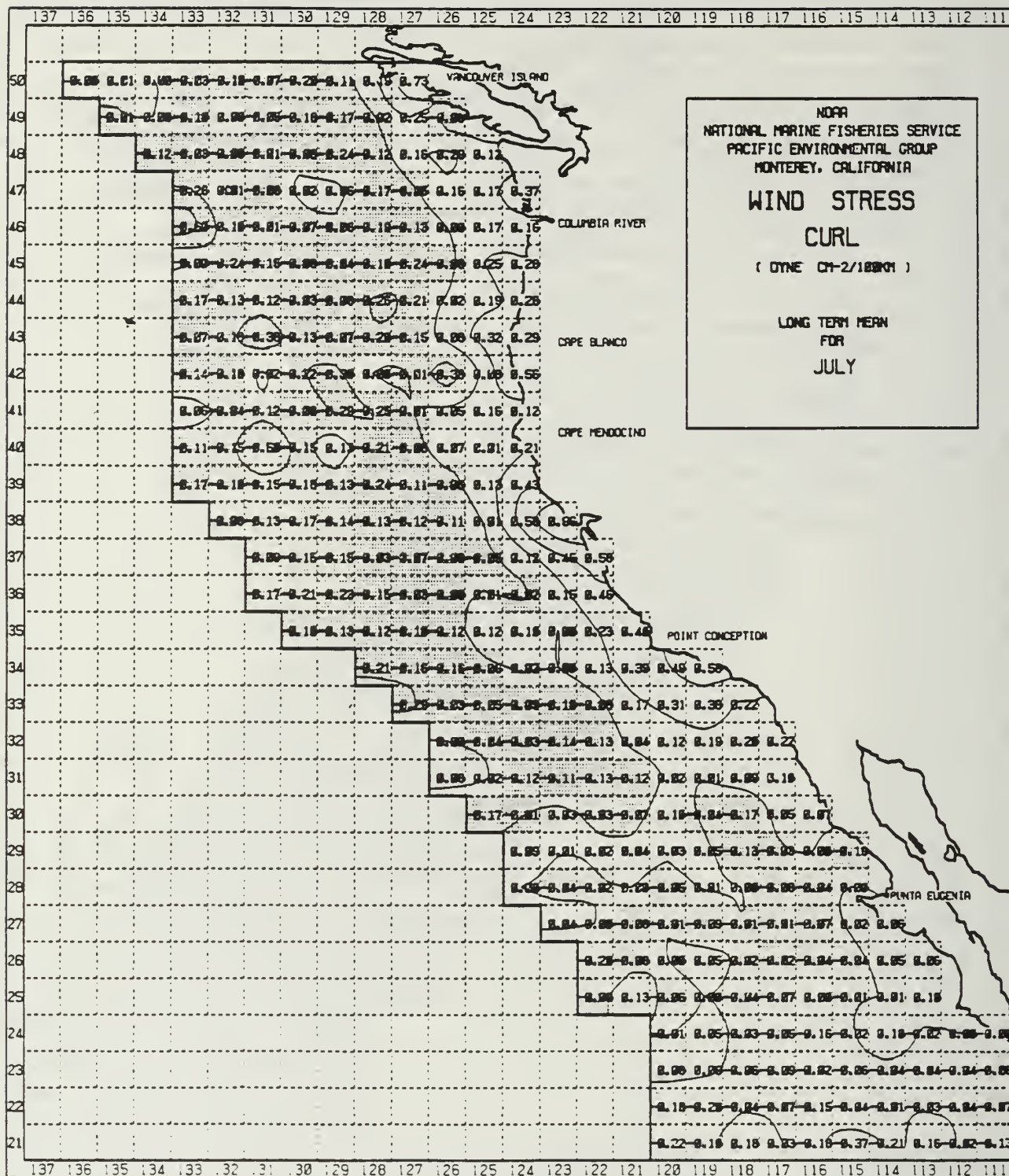


Figure 2.7) Climatological wind stress curl for July (from Nelson, 1977).



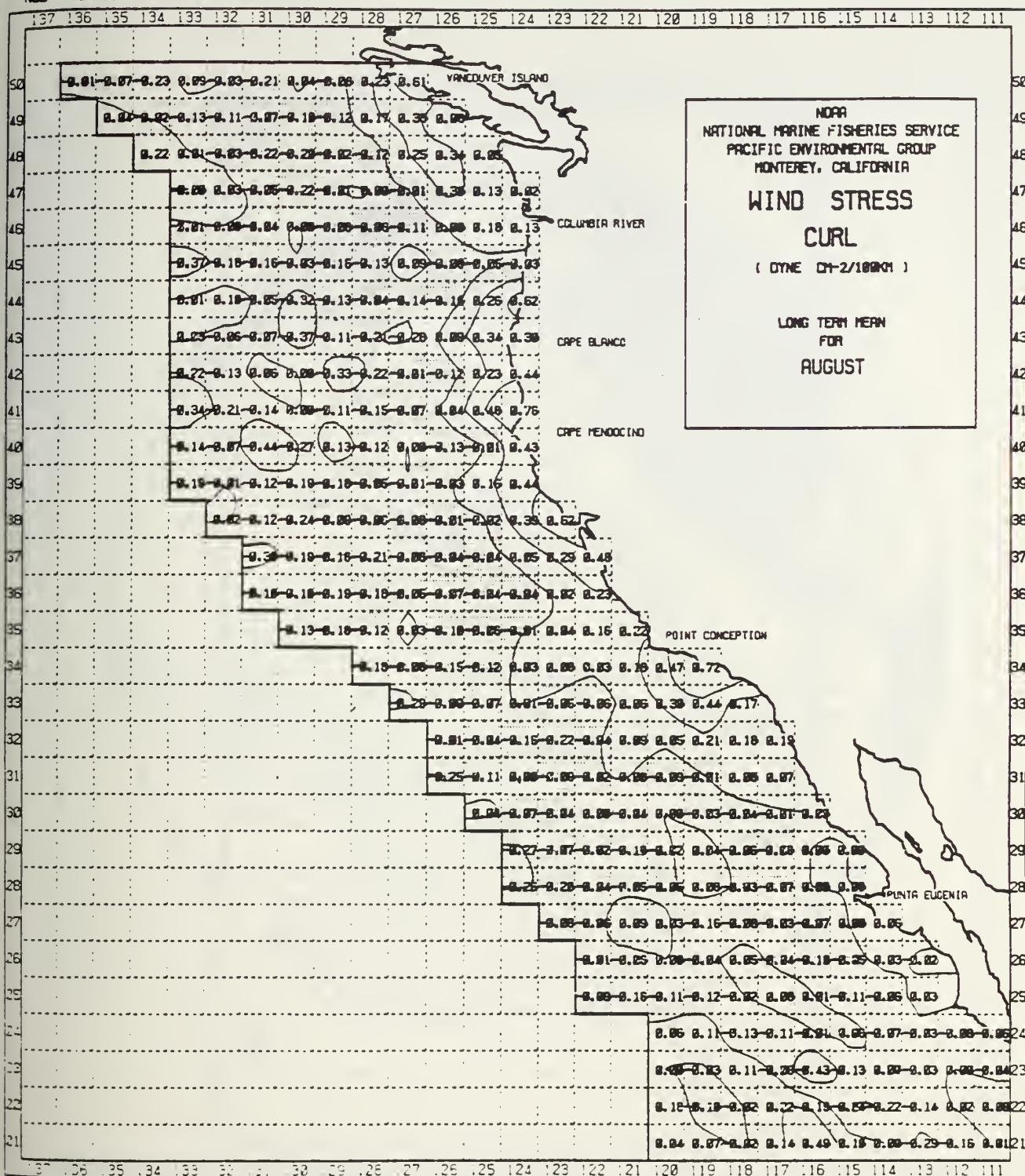


Figure 2.8) Climatological wind stress curl for August (from Nelson, 1977).

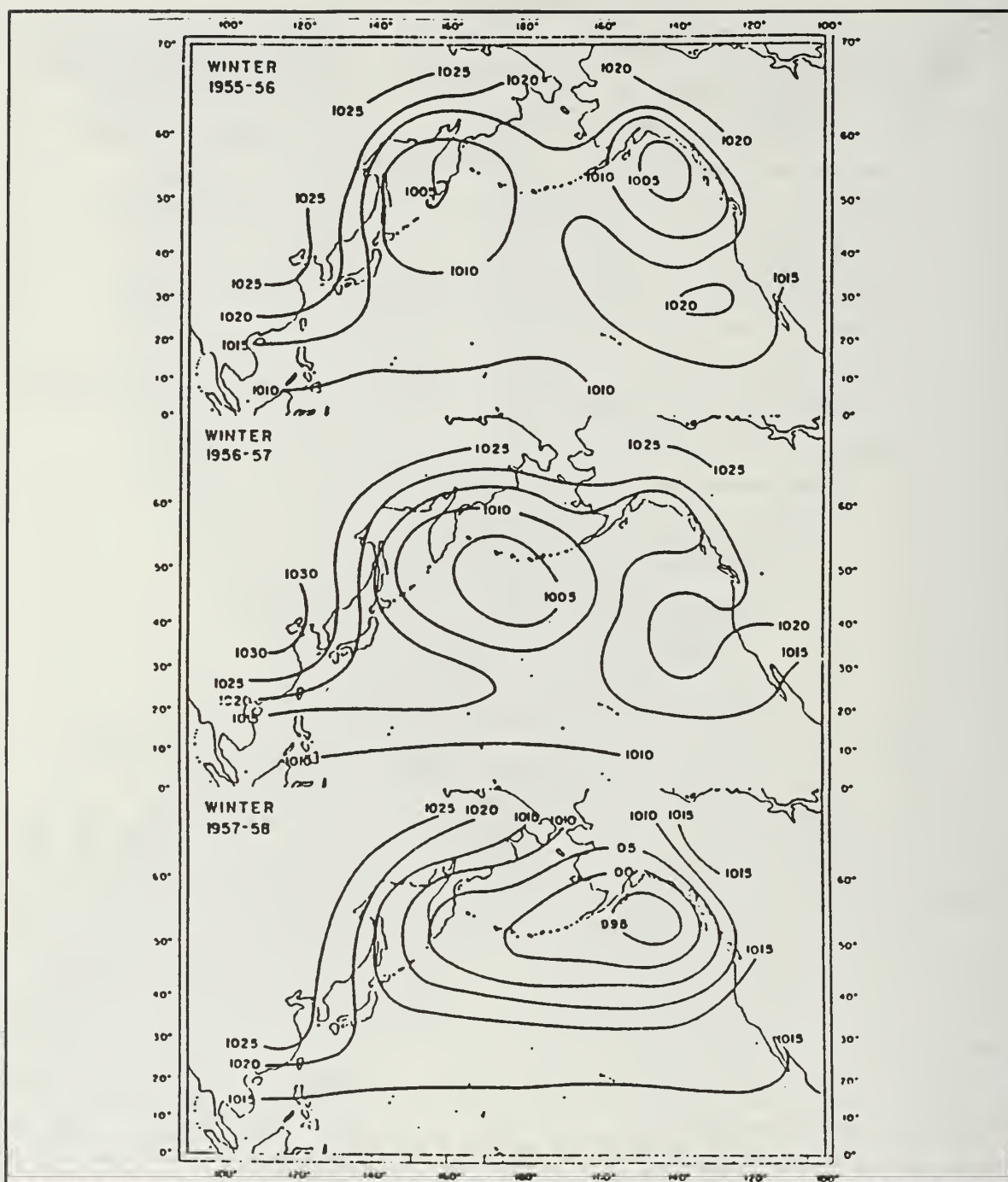


Figure 2.9: Average distribution of atmospheric pressure at sea level during the winter seasons, December to February inclusive, of 1955-56 and 1956-57, before the East Pacific equatorial warming, and 1957-58 at the peak of that warming (from Bjerknes, 1966).



Figure 2.10:— A schematic diagram of the Pacific North American (PNA) pattern of middle- and upper-tropospheric geopotential height anomalies during a Northern Hemisphere winter that coincides with El Niño conditions in the tropical Pacific (from Philander, 1990).



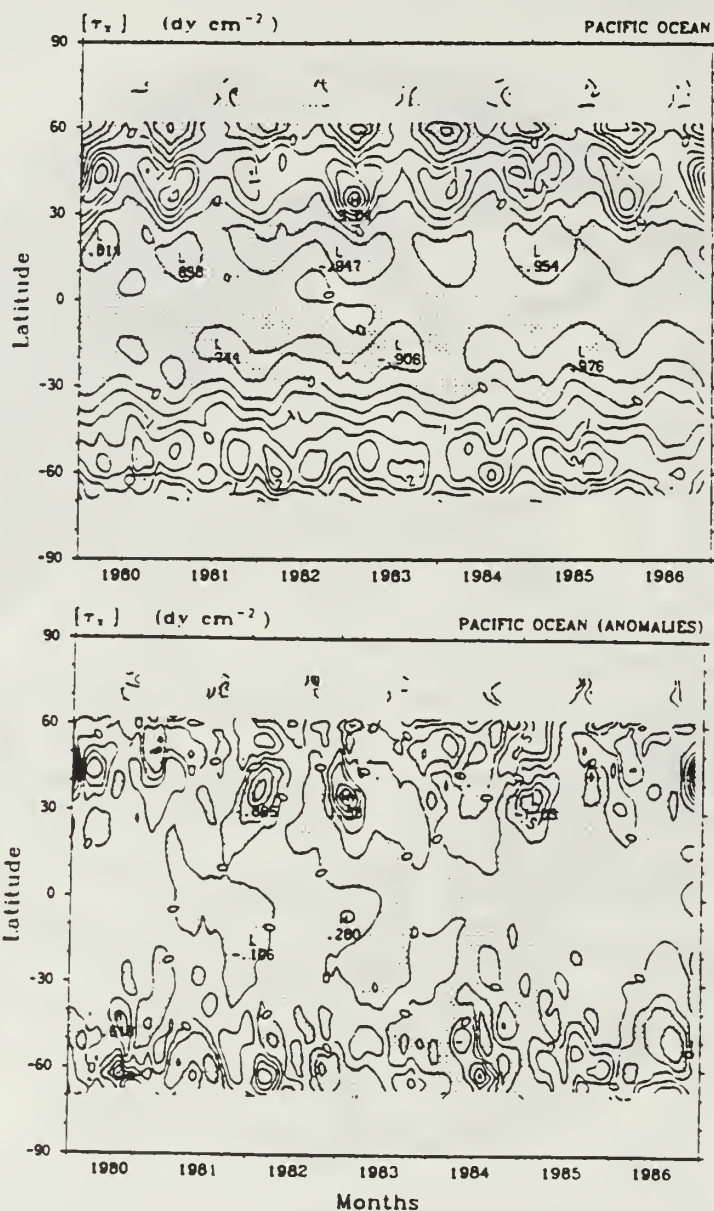


Figure 2.11: Latitude-time sections of the monthly mean wind stress from 1980 to 1986 eastward component zonally averaged for the Pacific Ocean: (a) total, contour  $0.5 \text{ dyn cm}^{-2}$ ; and (b) departures from the mean annual cycle, contour  $0.25 \text{ dyn cm}^{-2}$ . Negative values are stippled (from Trenberth et al. 1990).

### III. MODEL DESCRIPTION

The numerical model used in this research was developed by Haney (1974, 1985) for a closed basin, and later adapted by Batteen (1989) and Batteen *et al.* (1989) for application to limited area eastern boundary current regions with open borders on the northern, western and southern boundaries. The model has been thoroughly described in Batteen *et al.* (1989) and is summarized here.

#### A. MODEL EQUATIONS

To investigate the role of interannual variability in wind forcing on the generation of currents, eddies and filaments in the CCS, the wind stress fields, described below, were used to specify the wind forcing for a high-resolution, multi-level, primitive equation (PE) model of a baroclinic ocean on a  $\beta$ -plane. The model is based on the hydrostatic, Boussinesq, and rigid lid approximations. The governing equations may be written in the above framework as:

##### a. Momentum Equations:

$$\frac{du}{dt} = \frac{-1}{\rho_0} \frac{\partial p'}{\partial x} + f v - A_m \nabla^4 u + K_m \frac{\partial^2 u}{\partial z^2} + \delta_d(u) \quad (3.1)$$



$$\frac{dv}{dt} = \frac{-1}{\rho_0} \frac{\partial p'}{\partial y} - f u - A_m \nabla^4 v + K_m \frac{\partial^2 v}{\partial z^2} + \delta_d(v) \quad (3.2)$$

b. Continuity Equation:

$$w = - \int_{-H}^z \left( \frac{\partial u}{\partial x} + \frac{\partial v}{\partial y} \right) d\xi \quad (3.3)$$

c. Vertically Integrated Hydrostatic Equation:

$$p' = \int_z^0 \rho g d\xi - \frac{1}{H} \int_{-H}^0 \left[ \int_z^0 \rho g d\xi \right] dz \quad (3.4)$$

d. Equation of State:

$$\rho = \rho_0 (1 - \alpha (T - T_0)) \quad (3.5)$$

e. Thermodynamic Equation:

$$\frac{dT}{dt} = -A_H \nabla^4 T + K_H \frac{\partial^2 T}{\partial z^2} + Q_s + \delta_d(T) \quad (3.6)$$

In the equations,  $(x, y, z)$  is a right-handed coordinate system, with  $x$  positive toward shore,  $y$  alongshore, and  $z$  upward. The corresponding velocity components are  $(u, v, w)$ ,  $t$  is time,  $T$  is temperature,  $\rho$  is density, and  $p'$  is the departure from the vertically averaged pressure. The Coriolis parameter  $f$  is a linear function of latitude, so that  $f = f_0 + \beta y$ . This

approximation allows use of either the  $f$ -plane or the  $\beta$ -plane. In this study we used the  $\beta$ -plane approximation in order to allow the propagation of Rossby waves. In equations (3.3) and (3.4),  $\xi$  is a dummy variable of integration. Equation (3.5) is a linearized equation of state that assumes that density is a function of temperature only. This assumption has been shown to be consistent with the region being modeled (Lynn et al., 1982). Salinity is a good tracer for water masses in the CCS (Huyer and Kosro, 1987; Lynn and Simpson, 1987), but there are no major salinity sources or sinks in the region being modeled, and inclusion of salinity in the equation of state is not necessary for a zero-order description of the CCS. In (3.6),  $Q_s = \partial S / \rho_0 C \partial z$  is the heating due to solar radiation, where

$$S = S_0 (R e^{z/z_1} + (1-R) e^{z/z_2}) \quad (3.7)$$

$S_0$  is the downward flux of solar radiation at the surface,  $R = 0.62$  is the fraction of solar radiation absorbed in the upper few meters of the water column ( $z_1 = 1.5$  m), and  $(1 - R) = 0.38$  is the fraction that penetrates to deeper levels ( $z_2 = 20$  m) as given by Paulson and Simpson (1977). The  $\delta_d(u)$ ,  $\delta_d(v)$ , and  $\delta_d(T)$  terms represent the vertical turbulent mixing of momentum and heat by a dynamic adjustment mechanism. This adjustment is a generalization of the convective adjustment mechanism, and is based on the assumption of a critical

Richardson number. The dynamic adjustment mechanism serves to maintain dynamic stability in the water column (Adamec *et al.*, 1981).

The boundary conditions at the top ( $z=0$ ) of the model are:

$$K_m \frac{\partial u}{\partial z} = \frac{\tau^x}{\rho_0} \quad (3.8a)$$

$$K_m \frac{\partial v}{\partial z} = \frac{\tau^y}{\rho_0} \quad (3.8b)$$

$$K_H \frac{\partial T}{\partial z} = -Q_B \quad (3.8c)$$

$$w=0 \quad (3.8d)$$

and at the bottom ( $z = -H$ ) they are:

$$K_m \frac{\partial u}{\partial z} = C_D (u^2 + v^2)^{1/2} (u \cos \gamma - v \sin \gamma) \quad (3.9a)$$

$$K_m \frac{\partial v}{\partial z} = C_D (u^2 + v^2)^{1/2} (v \cos \gamma - u \sin \gamma) \quad (3.9b)$$

$$K_H \frac{\partial T}{\partial z} = 0 \quad (3.9c)$$

$$w=0 \quad (3.9d)$$

In (3.8a,b),  $\tau^x$  and  $\tau^y$  are the cross-shore and alongshore components of the surface wind stress. In (3.8c),  $Q_s$  is the net upward flux of longwave radiation, sensible and latent heat across the sea surface. The bottom stress in (3.9a,b) represents one of the simplest possible parameterizations of a bottom Ekman layer. The geostrophic inflow angle (Weatherly, 1972),  $\gamma$ , is  $10^\circ$ . Table 3.1 provides a list of other symbols used in the model equations, as well as values of constants used in this study.

## B. MODEL DOMAIN AND RESOLUTION

The domain of the model is a rectangular region extending from  $35^\circ\text{N}$  to  $47.5^\circ\text{N}$  and  $12^\circ$  in longitude from the west coast of the United States. The model extends from approximately Pt. Conception, California in the south to Cape Elizabeth, Washington in the north. The domain size is approximately 1024 km in the offshore direction and 1664 km alongshore. The horizontal resolution of the model is 8 km in the cross-shore direction and 13 km in the alongshore direction. This horizontal grid resolution should allow realistic spatial resolution of mesoscale features in the CCS, which have

typical wavelengths on the order of 100 km (Breaker and Mooers, 1986). In order to concentrate on the role of wind forcing only in the generation of eddies and jets, variations in the coastline and bottom topography are omitted from this version of the model.

### **C. FINITE DIFFERENCE SCHEME**

The numerical model used in this study is a staggered grid model, using the Arakawa and Lamb (1977) B-scheme, which has  $u$  and  $v$  defined at the center point of a grid box and  $T$ ,  $\rho$ ,  $w$ , and  $p$  at the corners. There are 10 layers in the vertical, separated by constant  $z$ -levels at 13, 46, 98, 182, 316, 529, 870, 1416, 2283 and 3656 m. This method of vertical spacing is designed to concentrate more layers in the upper, more dynamically active surface region above the main thermocline (Haney, 1974). Time stepping consists of a Matsuno (backward) time step followed by ten leapfrog time steps, with this pattern repeating throughout the model run.

### **D. HEAT AND MOMENTUM DIFFUSION**

Biharmonic lateral momentum and heat diffusion are used in the model in order to ensure that the friction acts on a scale smaller than the mesoscale features we are trying to observe (Holland, 1978; Holland and Batteen, 1986). Laplacian diffusion tends to suppress baroclinic instability processes at the mesoscale level and is not appropriate for a mesoscale eddy resolving model.



## E. SURFACE THERMAL FORCING

In order to isolate the effects of wind forcing on generating thermal variability in the CCS, the surface thermal forcing for this model is highly simplified. The solar radiation at the surface,  $S_0$ , is specified to be the summertime mean CCS value from Nelson and Husby (1983). The sum of the net longwave radiation, latent and sensible heat fluxes,  $Q_B$ , was computed during the model experiments from standard bulk formulas (Haney et al., 1978), using the read-in wind fields, summertime mean CCS values for cloud cover, relative humidity, air temperature, and model-predicted sea surface temperature (Haney et al., 1978). The initial sea surface temperature was chosen such that there would be no net heat flux across the sea surface at time  $t = 0$  (i.e.  $S_0 - Q_B = 0$ ). Therefore the only surface thermal forcing in the model is that which develops in  $Q_B$  as a result of wind-forced fluctuations in sea surface temperature. Further justification and a more detailed description of this formulation may be found in Batteen et al. (1989) and Haney (1985).

## F. HORIZONTAL BOUNDARY CONDITIONS

The eastern boundary of the model domain is closed, and is modeled as a straight, vertical wall. The kinematic boundary condition of no flow through the boundary is imposed on the cross-shore ( $u$ ) velocity component. Either free-slip or no-slip boundary conditions can be applied to the alongshore

(v) velocity component. In this study, a no-slip condition is invoked.

The northern, southern and western boundaries are open, and use a modified version of the radiation boundary conditions of Camerlengo and O'Brien (1980). Some spatial smoothing is also applied within 5 grid-points (~50 km) of the open boundaries.

In previous experiments with steady equatorward wind forcing applied to the northern and southern open boundaries, an alongshore current developed that was too strong, too deep and oriented equatorward at all depths (McCreary, 1981). In order to generate a realistic current system, the wind forcing was applied in a latitudinal band such that there was no wind stress near the northern and southern boundaries. This method allows poleward propagating Kelvin waves to be generated at the southern end of the wind forcing region, which produces an alongshore pressure gradient. This traps the equatorward jet at the coast and generates the poleward undercurrent (Batteen et al., 1989). The temporal and spatial variability in the "real" wind forcing, however, avoids this problem, with the result that we can apply wind forcing to all the boundaries for this study.

## G. INITIAL CONDITIONS

All of the experiments except the spun up runs were started from a state of rest. The initial mean stratification

used in all experiments is an exponential temperature profile with a vertical length scale of  $h = 450$  m. The exact form is:

$$T(z) = T_B + \Delta T e^{z/h} \quad (3.10)$$

The approximation assumes  $T_B = 2^\circ\text{C}$  to be the temperature at great depth, and  $\Delta T = 13^\circ\text{C}$  to be the increase in temperature between the bottom of the ocean and the surface. This temperature profile is the same profile used by Batteen (1989) and Batteen et al. (1989), and was derived by Blumberg and Mellor (1987) from available CCS observations of the long-term, mean climatological temperature stratification for the CCS region as a whole.

## H. WIND DATA DESCRIPTION

The model is forced with surface wind fields from the European Centre for Medium Range Weather Forecasts (ECMWF) surface wind analyses (Trenberth et al., 1989). Monthly mean stresses on a  $2.5^\circ \times 2.5^\circ$  grid based on twice-daily 1000 mb wind analyses were interpolated spatially to the  $8 \times 13$  km model resolution, and temporally to daily wind values. Winds from 1980-1983 were used, as well as a 120-month climatological average for the period 1980-1989. The 1980-1983 period was chosen due to the high degree of interannual variability in the winds that should be evident over the period before and during the 1982-83 El Niño event. The

climatological average wind fields were used as a baseline for comparing the individual runs, as well as to spin up the model for one year prior to the 1980-1983 continuous run.

Since the interpolated winds were created from monthly winds on a  $2.5^{\circ} \times 2.5^{\circ}$  grid, any possible manifestation of short-term or small-scale wind events is not resolved. Only seasonal or long-term, large-scale events such as wind field changes during an El Niño are preserved in the original ECMWF fields. It is anticipated that future experiments will be forced with winds that have higher spatial and temporal resolution, but these winds are certainly adequate for this process-oriented study.

## **I. EXPERIMENTAL DESIGN**

The first experiment is forced with the 120-month climatological wind fields. The subsequent four experiments are forced with the 1980-1983 winds. These five experiments are run for a period of 360 days each. Next a sixth and seventh experiment are each spun up for one year with the climatological wind fields and then forced with the 1980 and 1983 winds, respectively. Experiments one through five are started from rest in order to compare exactly when eddy formation is seen in each year. Experiments six and seven are intended to provide an idealized picture of what the interannual wind fields will do to the existing eddy fields left from the prior year.



## I. ENERGY ANALYSIS TECHNIQUES

The energy analysis technique used by Batteen *et al.* (1992) is used to analyze the generation of eddies, jets and filaments in the CCS. The following is a summary of their description of that technique.

The energy calculations are presented using the Semtner and Mintz (1977) notation:

$\overline{(\ )}$	<i>time average</i>
$(\ )'$	<i>time deviation</i>
$(\ )^{\sim}$	<i>horizontal space average</i>
$(\ )^*$	<i>horizontal space deviation</i>

The kinetic energy (K) is calculated by:

$$K = \frac{u^2 + v^2}{2} \quad (3.11)$$

After reaching a quasi-steady state in which the total kinetic energy is nearly constant, the time mean and time eddy kinetic energy are calculated by:

$$\overline{K} = \frac{\overline{u^2} + \overline{v^2}}{2} \quad (3.12)$$

$$K' = \frac{\overline{u'^2} + \overline{v'^2}}{2} \quad (3.13)$$

Available potential energy (P) is calculated by:

$$P = \alpha g \left[ \frac{1}{2} (T^*)^2 \left( \frac{\partial \tilde{T}}{\partial z} \right)^{-1} \right] \quad (3.14)$$

which determines when a quasi-steady state is reached and statistics can be collected. The temporal mean and eddy available potential energy are then calculated by:

$$\bar{P} = \alpha g \left[ \frac{1}{2} (\overline{T^*})^2 \left( \frac{\partial \bar{T}}{\partial z} \right)^{-1} \right] \quad (3.15)$$

$$P' = \alpha g \left[ \frac{1}{2} \overline{(T'^*)^2} \left( \frac{\partial \bar{T}}{\partial z} \right)^{-1} \right] \quad (3.16)$$

The transfers between the energy types are defined, after Semtner and Mintz (1977), by:

$$\{\bar{K} \rightarrow \bar{P}\} = -\alpha g [\overline{T w}] \quad (3.17)$$

$$\{P' \rightarrow K'\} = \alpha g [\overline{T' w'}] \quad (3.18)$$

$$\{\bar{K} \rightarrow K'\} = \bar{\mathbf{v}} (\nabla \cdot \overline{\mathbf{v}' \mathbf{v}'} + \frac{\partial}{\partial z} \overline{w' \mathbf{v}'}) \quad (3.19)$$

$$\{\bar{P} \rightarrow P'\} = \alpha g [\bar{T}^* \nabla \cdot \overline{\mathbf{v}' T'^*} \left( \frac{\partial \bar{T}}{\partial z} \right)^{-1}] \quad (3.20)$$

The model output consists of velocity components and temperature at specified intervals at each gridpoint. Neither the vertical velocity nor advection terms calculated by the model are stored. As the calculation of the energy transfers requires both vertical velocity and numerous advection terms, these are recalculated in the same manner as during a model run, but using the stored values of  $u$ ,  $v$ , and  $T$  as the input data. These recalculated energy transfers are consistent with the initial calculations of vertical velocity and advection terms obtained during the model run.

Semtner and Mintz (1977) applied their energy transfer analysis to currents which had become unstable, generated eddies and then reached a quasi-steady state. In this study, the quasi-steady energy state prior to and during eddy formation is examined, and the energy transfer analysis is used to argue for the instability mechanism (baroclinic vs. barotropic) which leads to eddy generation.

Table 3.1 VALUES OF CONSTANTS USED IN THE MODEL

C	$0.958 \text{ cal gm}^{-1}(\text{°K})^{-1}$	specific heat of sea water
$C_D$	$1.225 \times 10^{-3}$	bottom drag coefficient
$f_0$	$278.2\text{°K}$	constant reference temperature
$\rho_a$	$1.23 \times 10^{-3} \text{ gm cm}^{-3}$	density of air
$\rho_0$	$1.0276 \text{ gm cm}^{-3}$	density of sea water at $T_0$
$\alpha$	$2.01 \times 10^{-4} (\text{°K})^{-1}$	thermal expansion coefficient
D	10	number of levels in vertical
$\Delta x$	$8.0 \times 10^5 \text{ cm}$	cross-shore grid spacing
$\Delta y$	$13.0 \times 10^5 \text{ cm}$	alongshore grid spacing
D	$4.5 \times 10^5 \text{ cm}$	total ocean depth
$\Delta t$	800 s	time step
$f_0$	$0.93 \times 10^{-4} \text{ s}^{-1}$	mean coriolis parameter
g	$980 \text{ cm s}^{-2}$	acceleration of gravity
$A_M$	$2 \times 10^{17} \text{ cm}^4 \text{ s}^{-1}$	biharmonic momentum diffusion coefficient
$A_H$	$2 \times 10^{17} \text{ cm}^4 \text{ s}^{-1}$	biharmonic heat diffusion coefficient
$K_M$	$0.5 \text{ cm}^2 \text{ s}^{-1}$	vertical eddy viscosity
$K_H$	$0.5 \text{ cm}^2 \text{ s}^{-1}$	vertical eddy conductivity



#### IV. EXPERIMENT RESULTS

Experiments 1 through 5 study the effects of forcing a model domain that is initially at rest with climatological average and annual (1980-1983) wind fields. Experiments 6 and 7 use the 1980 and 1983 wind fields, respectively, to force a model domain that has been spun up for a period of one year with the climatological average wind fields. (Note that all figures of horizontal surface fields are shown five gridpoints (52 km) from the northern and southern model boundaries, in order to stay away from smoothed regions. This means that the figures display the interior of the model region, from approximately  $35.5^{\circ}$  to  $47^{\circ}\text{N}$ .)

##### A. RESULTS OF EXPERIMENTS STARTED FROM REST

###### 1. Experiment 1

In Experiment 1 the model was forced with the climatological average (1980-1989) wind fields. The wind forcing at the beginning of the year has a poleward component north of approximately  $40^{\circ}\text{N}$  and an equatorward component south of  $40^{\circ}\text{N}$  (Fig. 4.1a). The wind shifts as the North Pacific High moves onshore (Fig. 4.1b), and has an equatorward component throughout the model domain by day 180 (Fig. 4.1c). The winds intensify until day 255 (Fig. 4.1d), then start to weaken as

the North Pacific High moves southwest, and are divergent at 40°N again by day 300 (Figs. 4.1e).

An equatorward coastal jet forms in the southern portion of the model domain by day 60 (Fig. 4.2a). Evidence of upwelling is also seen in the colder surface temperature field near the coast (Fig. 4.2b). Eddies begin to form in the southern part of the model domain by day 120, as seen in the zonal velocity field (Fig. 4.3). (Since the velocity field at this point in the model year is primarily meridional, perturbations in the zonal velocity field are easily discernible.) Evidence of eddy formation in the surface temperature field is not seen until day 144 (Fig. 4.4), when meanders of the isotherms in the southern region of the domain are evident. A cross-section of meridional velocity at 43°N in the area of eddy formation at day 120 (Fig. 4.5) shows a surface equatorward jet with a maximum speed of approximately 35 cm s<sup>-1</sup> overlying a weaker poleward undercurrent centered at around 200 m depth.

Eddies form in the southern region of the model domain first. Although the  $\beta$ -plane effect would encourage eddy formation in the north, the longer duration and greater strength of the equatorward wind forcing in the south results in eddy generation in the southern portion of the domain. The eddies continue to form and the growth region moves to the north, until the entire eastern boundary region of the model domain contains mature eddies by day 285 (Figs. 4.6a,b,c).

Both baroclinic and barotropic instabilities play a role in eddy formation at day 120, with energy very nearly equally partitioned between the two (Figs. 4.7a,b). Baroclinic instability comes from the vertical shear in the mean flow, while barotropic instability comes from the horizontal shear. An inspection of the cross-section of meridional velocity at  $43^{\circ}\text{N}$  at day 120 (Fig. 4.5) shows that there is, indeed, both vertical and horizontal shear evident in the eddy formation region.

When the winds are at their weakest strength at day 345 (not shown), the horizontal shear in the mature eddy field is much stronger than the vertical shear. A comparison of baroclinic (not shown) and barotropic instability (Fig. 4.8) shows that barotropic instability is dominant over the entire model domain. This indicates that the mature eddy field contains mostly horizontal shear. A cross-section of meridional velocity in the northern part of the model domain at  $46.5^{\circ}\text{N}$  shows that the poleward undercurrent has moved to the surface and forced the equatorward jet offshore (Fig. 4.9). By comparing the surface zonal velocity at day 345 (Fig. 4.10) with the barotropic instability (Fig. 4.8), we see that the regions of strongest barotropic instability are associated with the southeastern edges of the eddies near the coast, and with the edge of the equatorward jet.

## **2. Experiments 2, 3, and 4**

The results for the experiments forced by the 1980, 1981 and 1982 winds were quite similar to those for the climatological average wind fields summarized above. Pertinent figures from these experiments are included as an Appendix.

## **3. Experiment 5**

The 1983 winds were dramatically different from the climatological average and 1980-1982 winds, especially during the first three months of the year. At the start of the year the winds contained a strong poleward component throughout the entire model domain (Fig. 4.11a). The strong poleward component in the northern part of the domain was seen until day 90 (Fig. 4.11b). The winds then shifted rapidly, developing an equatorward component throughout the model domain by day 105 (not shown). After day 120 (Figs. 4.11c,d,e,f), the 1983 winds were quite similar to the climatological average and previous years.

The intense poleward winds in the beginning of the year generated a poleward coastal jet by day 15 in the northern region of the model domain (not shown). The jet continued to intensify, and eddies began to form in the northern region by day 66, as shown by perturbations in the zonal velocity (Fig. 4.12a). In this case, meanders in temperature (Fig. 4.12b), velocity (4.12c) and dynamic height (Fig. 4.12d) showed up at the same time as the perturbations



of zonal velocity, indicating that the eddy formation is a more intense process than that seen in Experiments 1-4.

Both barotropic and baroclinic instabilities play a part in eddy formation (Figs. 4.13a,b), but the area of eddy formation has moved to the northern region of the model domain. In this area the  $\beta$ -plane effect will encourage eddy formation, and the amount of energy being converted (up to  $90 \text{ ergs cm}^3 \text{ s}^{-1}$ ) is much higher than that (up to  $7.6 \text{ ergs cm}^3 \text{ s}^{-1}$ ) in Experiment 1 (Figs. 4.7a,b). A cross-section of meridional velocity at  $46.5^\circ\text{N}$  at day 66 (Fig. 4.14) shows a relatively strong (approximately  $15 \text{ cm s}^{-1}$ ) poleward jet overlying a weak equatorward undercurrent, exactly the opposite of the flow seen in 1980-1982 (e.g., compare Fig. 4.14 with Fig. 4.5).

After the winds shift and become largely equatorward throughout the model domain, eddies develop in the south as in the earlier experiments. The zonal velocity field (Fig. 4.15a) at day 159 shows large (up to  $150 \text{ km}$  in diameter) eddies in the northern region and smaller eddies forming in the central and southern regions. Note that the large eddies in the northern region show up in the dynamic height field as positive anomalies (Fig. 4.15b). These eddies are associated with the poleward winds and onshore transport, have warm cores (not shown), and are anticyclonic. (In contrast, the eddies formed by equatorward winds were cyclonic, with cold cores, and show up as negative dynamic height anomalies.) A cross-section of meridional velocity at approximately  $41^\circ\text{N}$  at day

159 shows the more common mean state of the CCS, with an equatorward jet overlying a poleward undercurrent (Fig. 4.16). As in previous years, both baroclinic and barotropic instabilities (Figs. 4.17a,b) play a role in the eddy formation near the coast, as expected with the now prevalent equatorward winds. A comparison of Figures 4.17a,b with Experiment 1 (Fig. 4.7a,b), however, shows that the rate of energy conversion is much higher in 1983 than in the climatological average.

## **B. RESULTS OF EXPERIMENTS SPUN UP FROM CLIMATOLOGICAL WINDS**

### **1. Experiment 6**

Experiment 6 was forced with the 1980 winds, using the temperature and velocity fields at day 360 in Experiment 1 (climatological average wind forcing) as initial fields. Since the run starts with an existing eddy field, it is expected that wind forcing effects will be noticed earlier in the year. In the 1980 experiment started from rest, eddy formation started on day 90 (Appendix 1, Figs. A.1-A.5), whereas in this experiment new eddies began to form by day 60 (Fig. 4.18). (Note: Since this run started at day 360, the Figures are labeled with the model day plus 360, i.e., model day 60 is day 420 on the Figures.) Again, initial eddy formation was pinpointed by looking for perturbations in the zonal velocity field, which first occurred in the northern portion of the model domain (Fig. 4.18).

Eddy production is still due to both baroclinic and barotropic transfer processes (Figs. 4.19a,b), but in this case it is mostly baroclinic shear (4.19a) at day 60 (day 420). The baroclinic shear is dominant in this case because the winds are poleward in the northern region of the model domain, while the surface current is still equatorward, causing a strong vertical shear between the poleward wind and the equatorward surface current. The location for the eddy formation is also modified. In the run from rest, eddies initially form at the coast, while in this run they form not only at the coast but also along the equatorward jet, as seen by comparing the baroclinic instability (Fig. 4.19a) and the surface velocity field (Fig. 4.20). The eddies that form along the equatorward jet are examples of frontal instability processes. A cross-section of meridional velocity at  $46.5^{\circ}\text{N}$  at day 60 (day 420) again shows an equatorward jet overlying a poleward undercurrent (Fig. 4.21), but the equatorward jet has moved offshore and the poleward undercurrent has extended up to the surface, establishing a poleward surface current.

The most dramatic difference between the experiments started from rest (i.e., Experiments 1-5) and those that are spun up from the climatological winds is that the latter show evidence of filament formation during the upwelling season. This is clearly seen in the surface temperature field (Fig. 4.22a). By day 150 (day 510) there are three filaments in various stages of formation, with the largest extending to

over 300 km offshore. Surface velocities in the filaments are greater than  $50 \text{ cm s}^{-1}$  (Fig. 4.22b). The filaments are approximately 60 km across and have spread out into a hammerhead at the limit of their offshore extent, quite similar to the filaments seen in observations (e.g., Fig. 2.1). Another major difference between the experiments started from rest and those that were spun up from the climatological winds is the evidence of frontal instabilities along the coastal jet (seen in the northern portion of Fig. 4.19a).

## 2. Experiment 7

This experiment was forced with the 1983 winds, again using model fields spun up for a period of 360 days with the climatological average winds as initial conditions. The results were quite similar to those for Experiment 6. However, a cross-section of meridional velocity at  $45^\circ\text{N}$  at day 66 (day 426) (Fig. 4.23) does show that the surface poleward current is much stronger and extends farther offshore than in 1980 (Fig. 4.21). As in Experiment 6, there is evidence of both baroclinic (Fig. 4.24a) and barotropic (Fig. 4.24b) instability processes. Again, comparing the regions of baroclinic instability (Fig. 4.24a) to the surface velocity field (Fig. 4.25) shows that eddies are forming not only at the coast, but also along the equatorward jet.

Since the abnormally strong poleward winds during the first 90 days of the year had to work against the existing equatorward surface current, the effects were not as dramatic



as the differences seen between the 1980 and 1983 runs initialized from rest (i.e., Experiments 2 and 5). However, there were some notable differences between Experiments 6 and 7. A comparison of surface temperature for the two runs at day 150 (day 510) shows that the 1983 run (Fig. 4.26a) is approximately  $2^{\circ}$  warmer than the 1980 run (Fig. 4.22a). In addition, the filaments formed in 1983 extend only about 200 km offshore at this point in the year, as opposed to over 300 km for 1980. Note that the locations for filament formation in Figs. 4.22a and 4.26a are nearly the same, indicating that there is some geographical preference in locations for eddy and filament formation during the upwelling season, even without including a coastline or bottom topography in the model. A comparison of surface velocity fields at day 150 (day 510) in the two experiments indicates that the magnitudes for the current system as a whole are weaker and/or less developed in 1983 (Fig. 4.26b) than in 1980 (Fig. 4.22b).

### **C. COMPARISON OF RESULTS WITH OBSERVATIONS OF THE CCS**

Since this study isolates the effects of wind forcing only on the CCS, quantitative comparisons of model results with observations are not feasible. Particularly during the early part of the year, the experiments that start from rest cannot be compared with the CCS because the CCS is not at rest on January 1 each year. However, after the experiments are

allowed to spin up for a period of time, the model results may be qualitatively compared with observations.

Table 5.1 (based on Batteen et al., 1989) shows model results alongside some results of observations of the CCS. Experiment 5 (1983) is dramatically different from Experiments 1 through 4 (Climatological average and 1980-1982), but Experiments 6 (1980 spun up) and 7 (1983 spun up) are more similar to each other. As expected, the experiments that were started from a spun up state (Experiments 6 and 7) agree better with the observations than do any of the experiments (1 through 5) that were started from rest. Also, no evidence of filaments was seen in the experiments started from rest, but they were found in both of the spun up experiments.

Table 5.2 shows qualitative results from both of the El Niño year experiments (5 and 7) alongside some observations of the 1982-1983 CCS El Niño characteristics. Note that since the model does not include any kind of remote forcing or any salinity forcing term, the oceanic teleconnection will not be expressed in the model results. Even without the remote forcing, however, there is good qualitative agreement with observations from the 1982-1983 Californian El Niño. Warmer sea surface temperatures and evidence of onshore advection are noted, especially during the first 90 days of the year (days 360-450). Also, the entire current system is weaker than in the other model years, and poleward surface flow is enhanced. This is strong evidence that anomalous atmospheric forcing plays a major role in the generation of a CCS El Niño event.

Table 4.1 INSTANTANEOUS COMPARISON OF EXPERIMENTS (EXP.) WITH OBSERVATIONS (OBS) OF THE CCS.

	Obs. (References)	Exp. 1-4	Exp. 5	Exp. 6	Exp. 7
A. Maximum coastal jet velocity ( $\text{cm s}^{-1}$ )	30-100 (1,2,3,4)	80	80	100	100
B. Offshore location of coastal jet (km)	25-35 (2,3)	30-60	30-60	30-60	30-60
C. Offshore extent of coastal jet (km)	>40 (1,2,3)	80-100	80-100	80-100	80-100
D. Depth of inshore coastal jet (m)	90-150 (2,3)	175	175	175	175
E. Maximum undercurrent velocity ( $\text{cm s}^{-1}$ )	5-15 (2,3)	8	5	10	10
F. Offshore location of undercurrent axis (km)	10-40 (2,3)	20-30	15-25	20-30	15-25
G. Maximum width of undercurrent (km)	10-20 (2,3)	40	40	40	40
H. Depth of undercurrent axis (m)	200-300 (2)	200	200	200	200
I. Maximum zonal eddy diameter (km)	10->100 (2,5,6,7)	200	200	220	220
J. Maximum zonal eddy velocity ( $\text{cm s}^{-1}$ )	50-100 (1,2,3,4,6,7)	60-90	75	100	85

## References:

- (1) Kosro and Huyer (1986)
- (2) Huyer and Kosro (1987)
- (3) Kosro (1987)
- (4) Davis (1985)
- (5) Mooers and Robinson (1984)
- (6) Brink and Cowles (1991)
- (7) Brink et al. (1991)

TABLE 4.2 COMPARISON OF OBSERVED (OBS) AND MODEL EXPERIMENT (EXP)  
QUALITATIVE CCS FEATURES SEEN DURING EL NIÑO YEARS

El Niño Obs. compared to CCS Mean State	Exp. 5	Exp. 7
A. Warmer sea surface temperature (1,2,3)	Simulated	Simulated
B. Weaker overall current system (2)	Simulated	Simulated
C. Enhanced poleward flow (2,3)	Simulated	Simulated
D. Enhanced onshore advection (1,2,3)	Simulated	Simulated
E. Max equatorward surface current farther offshore (2)	Not Simulated	Simulated

References: (1) Mooers and Robinson (1984)  
(2) Simpson (1983)  
(3) Simpson (1984)



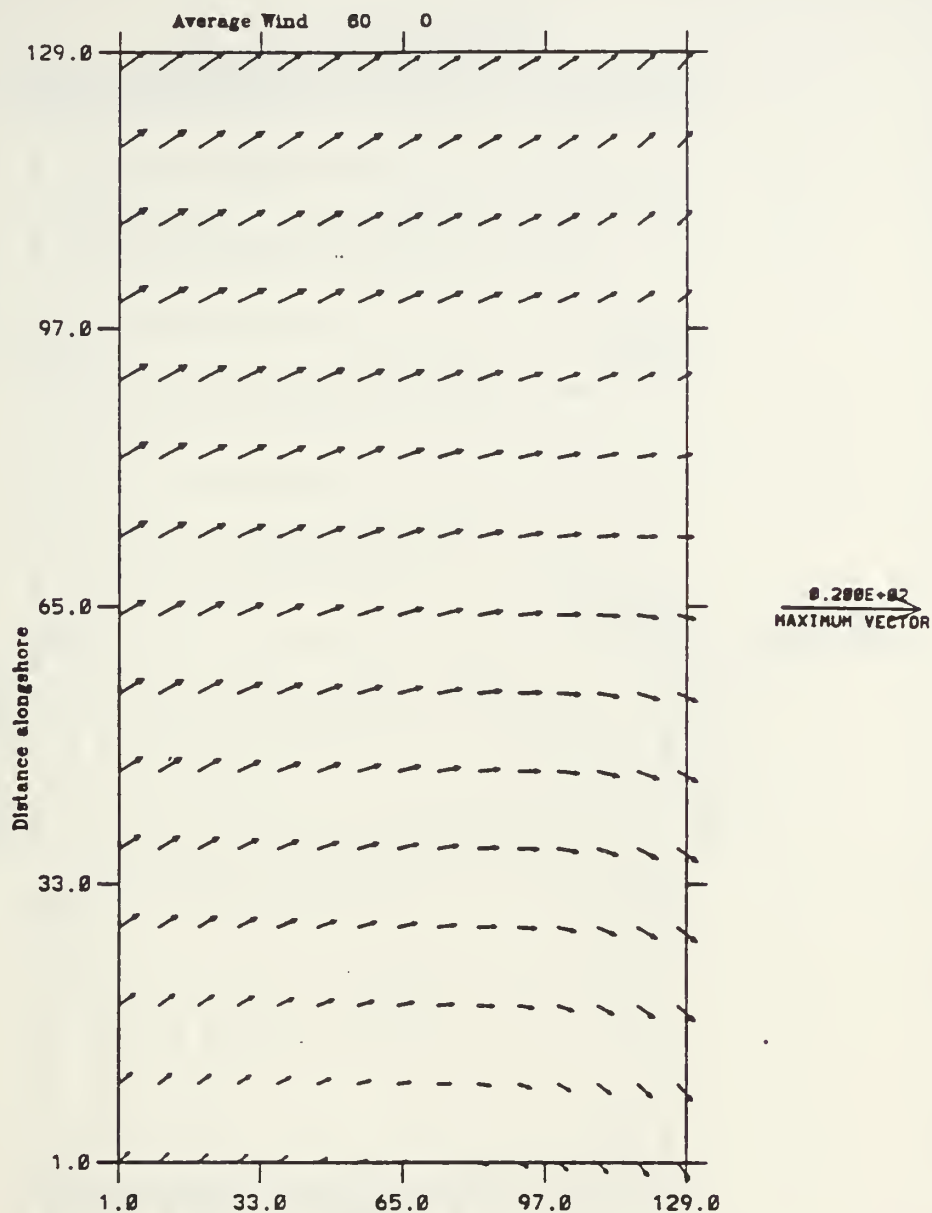


Figure 4.1a) Experiment 1: Climatological average wind forcing in  $\text{m s}^{-1}$  at day 60.  $\Delta x = 8 \text{ km}$ ,  $\Delta y = 13 \text{ km}$ . Wind values for every ninth gridpoint are plotted.

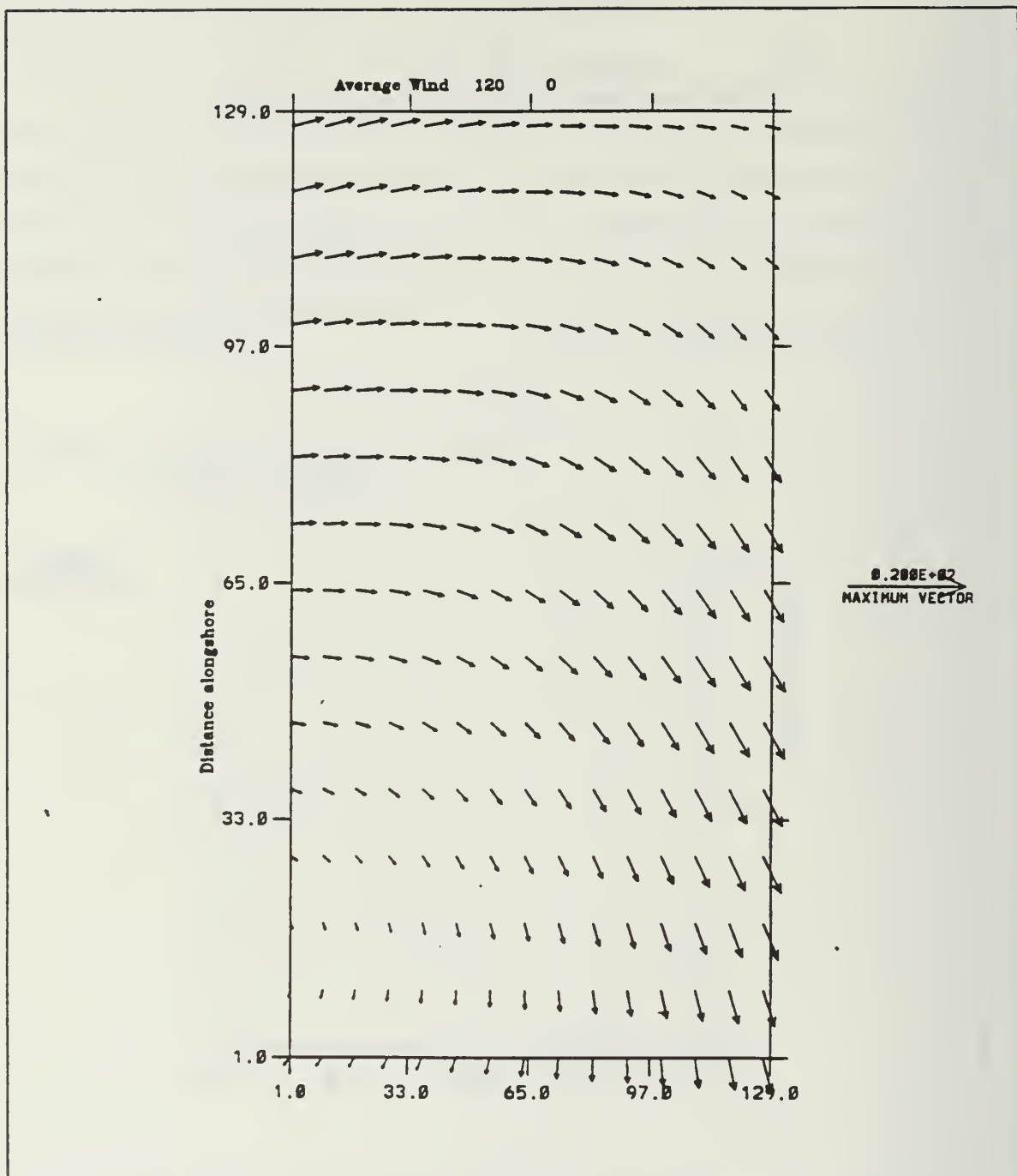


Figure 4.1b) Experiment 1: Climatological average wind forcing in  $\text{m s}^{-1}$  at day 120. As in Fig. 4.1a.

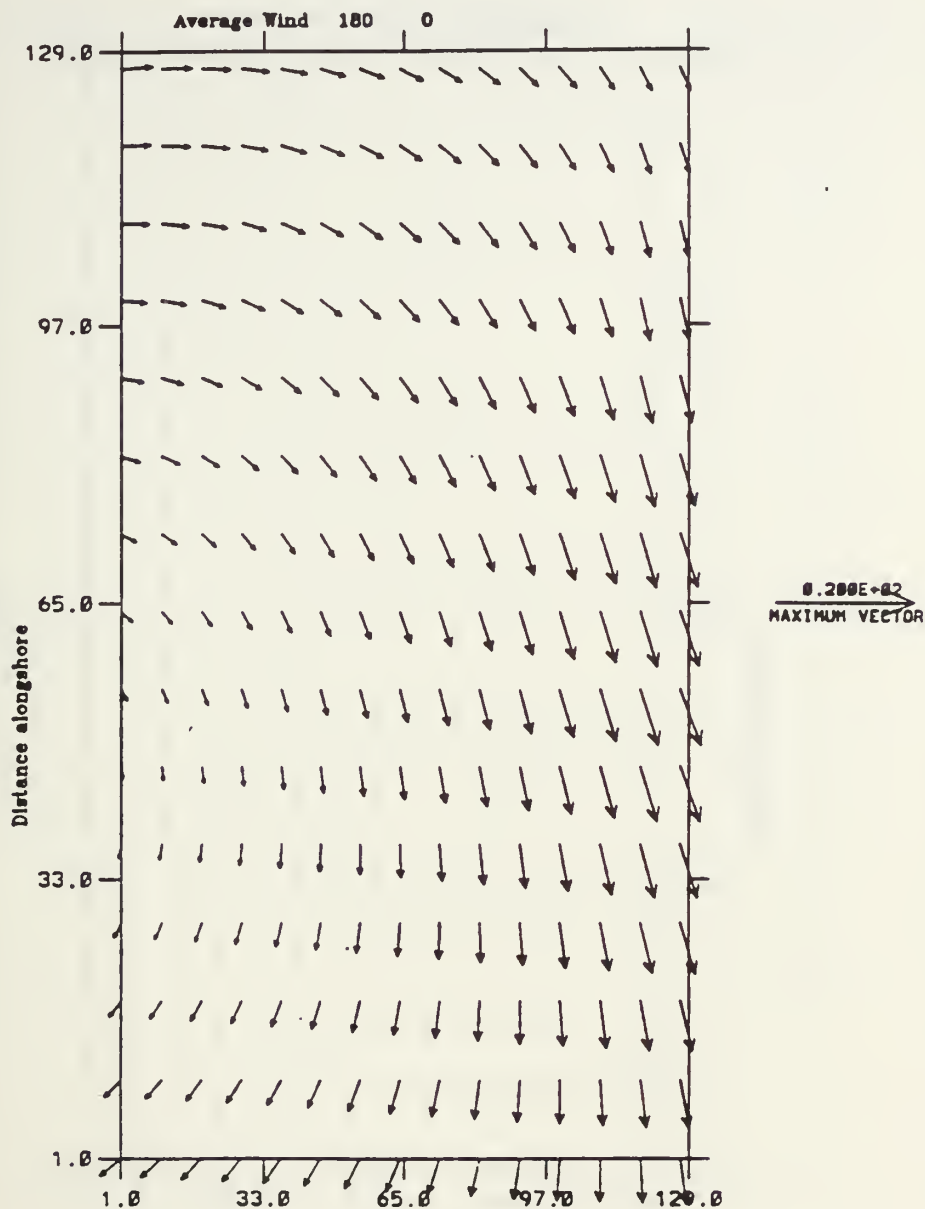


Figure 4.1c) Experiment 1: Climatological average wind forcing in  $\text{m s}^{-1}$  at day 180. As in Fig. 4.1a.

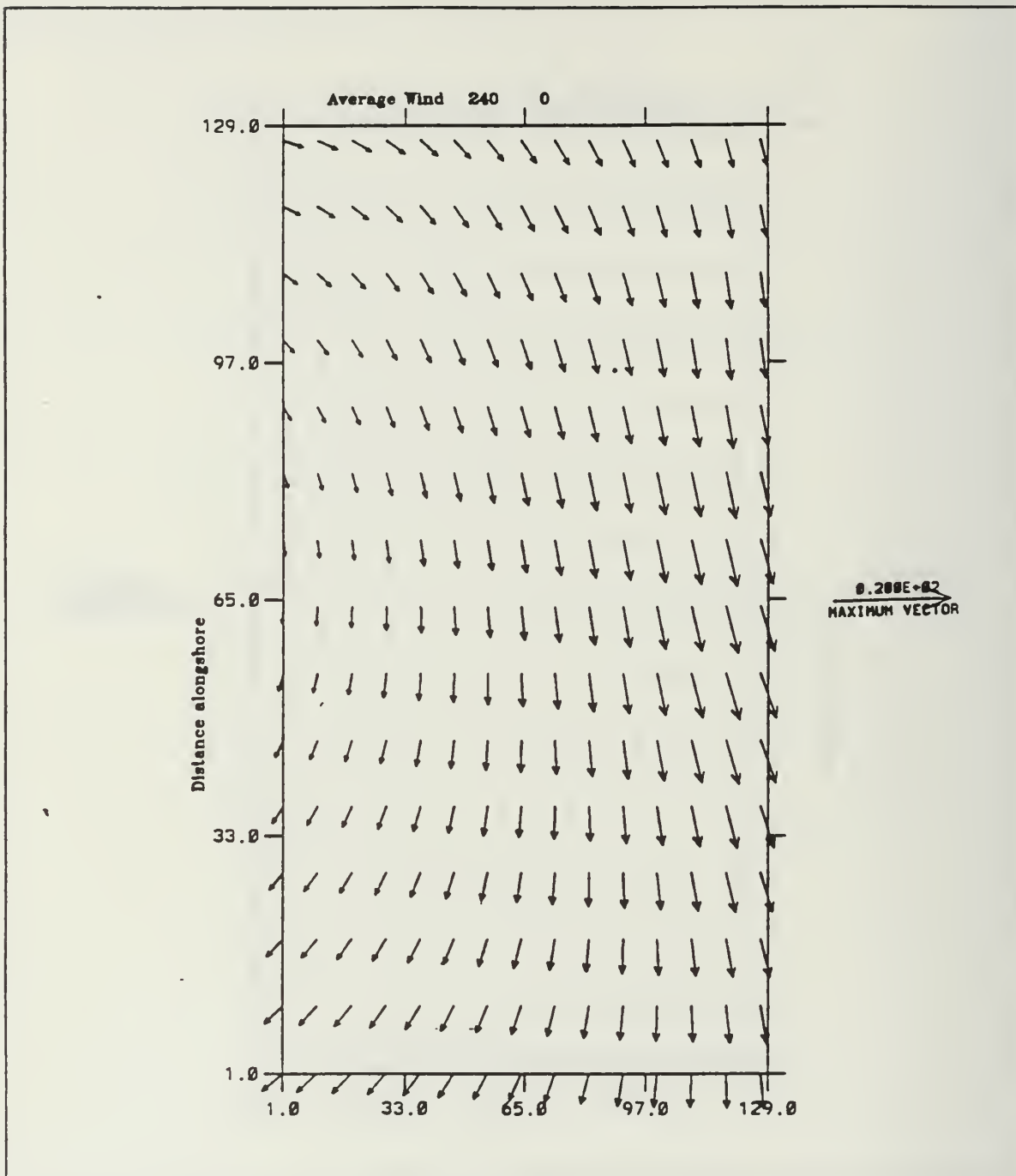


Figure 4.1d) Experiment 1: Climatological average wind forcing in  $\text{m s}^{-1}$  at day 240. As in Fig. 4.1a.



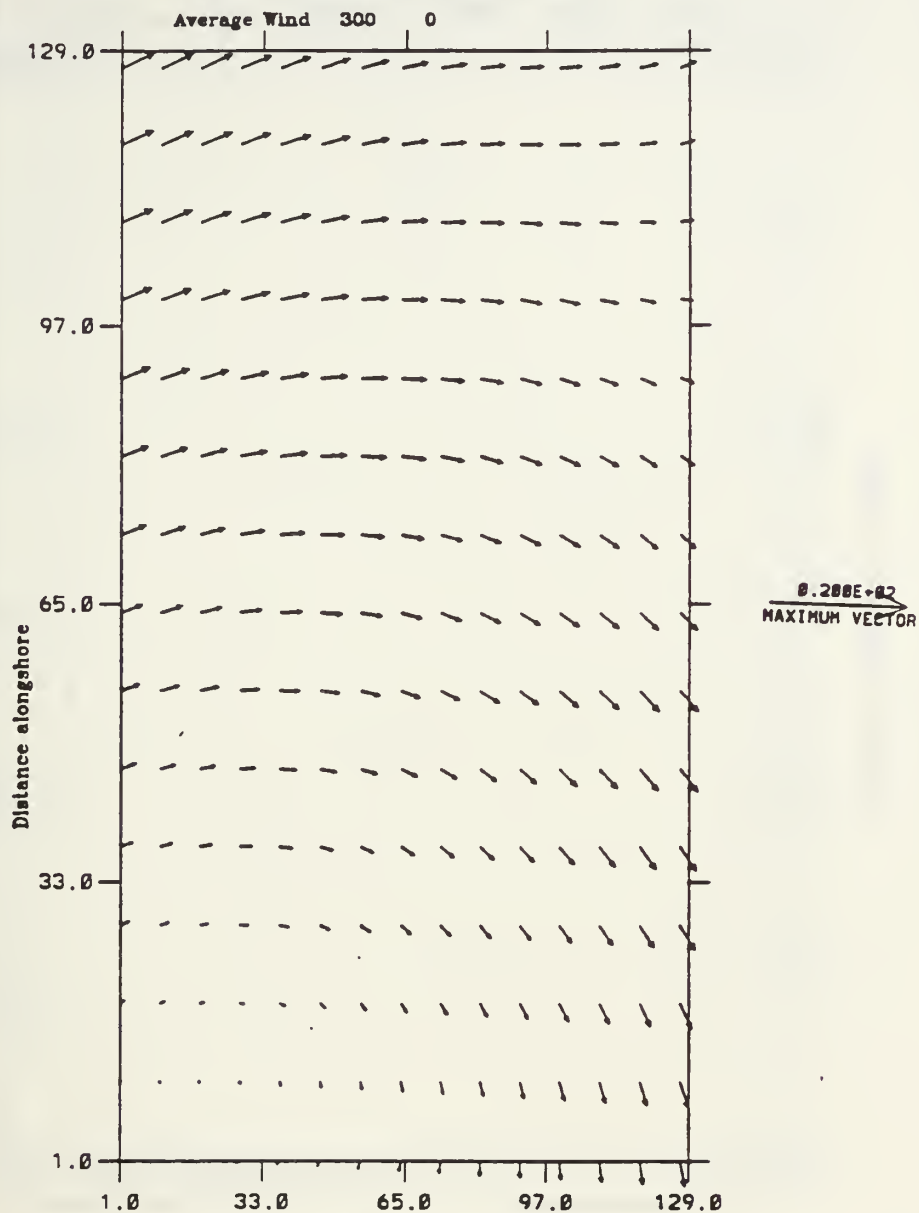


Figure 4.1e) Experiment 1: Climatological average wind forcing in  $\text{m s}^{-1}$  at day 300. As in Fig. 4.1a.

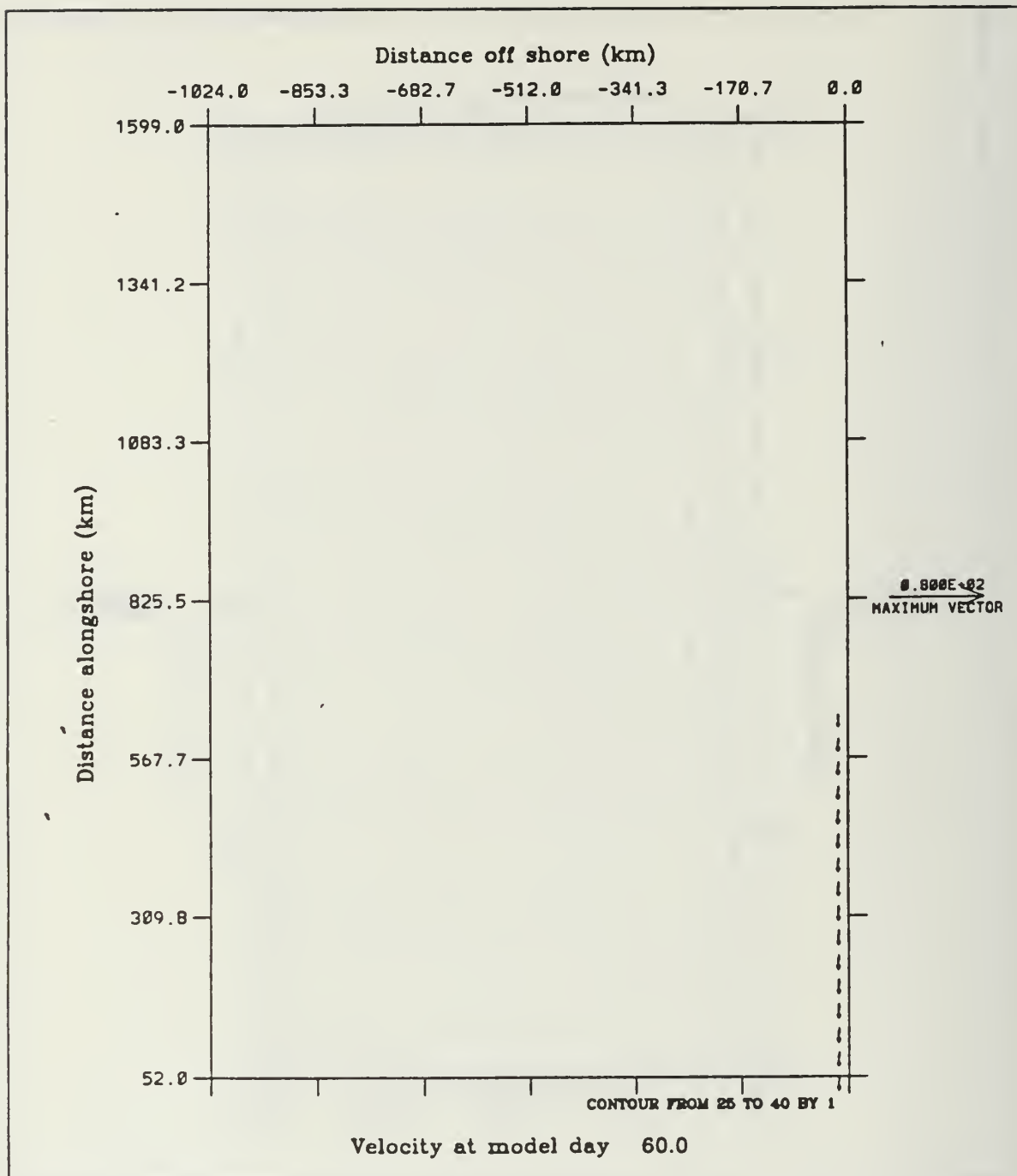


Figure 4.2a) Experiment 1: Surface velocity in  $\text{cm s}^{-1}$  at day 60. Values for every third gridpoint are plotted. Minimum vector plotted is  $25 \text{ cm s}^{-1}$ .

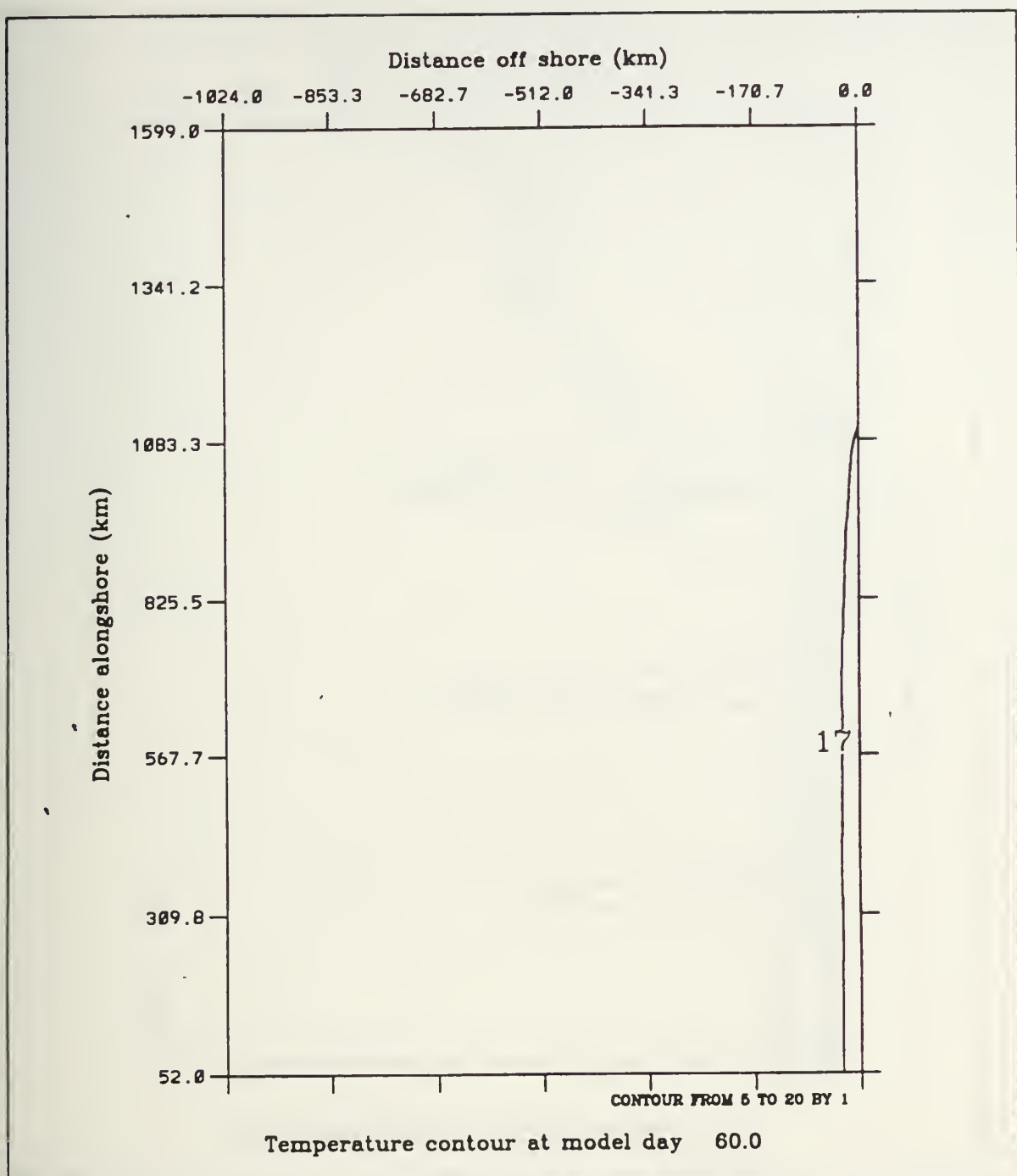


Figure 4.2b) Experiment 1: Surface temperature contours at day 60. The contour interval is 1°C. The temperature decreases toward the coast.

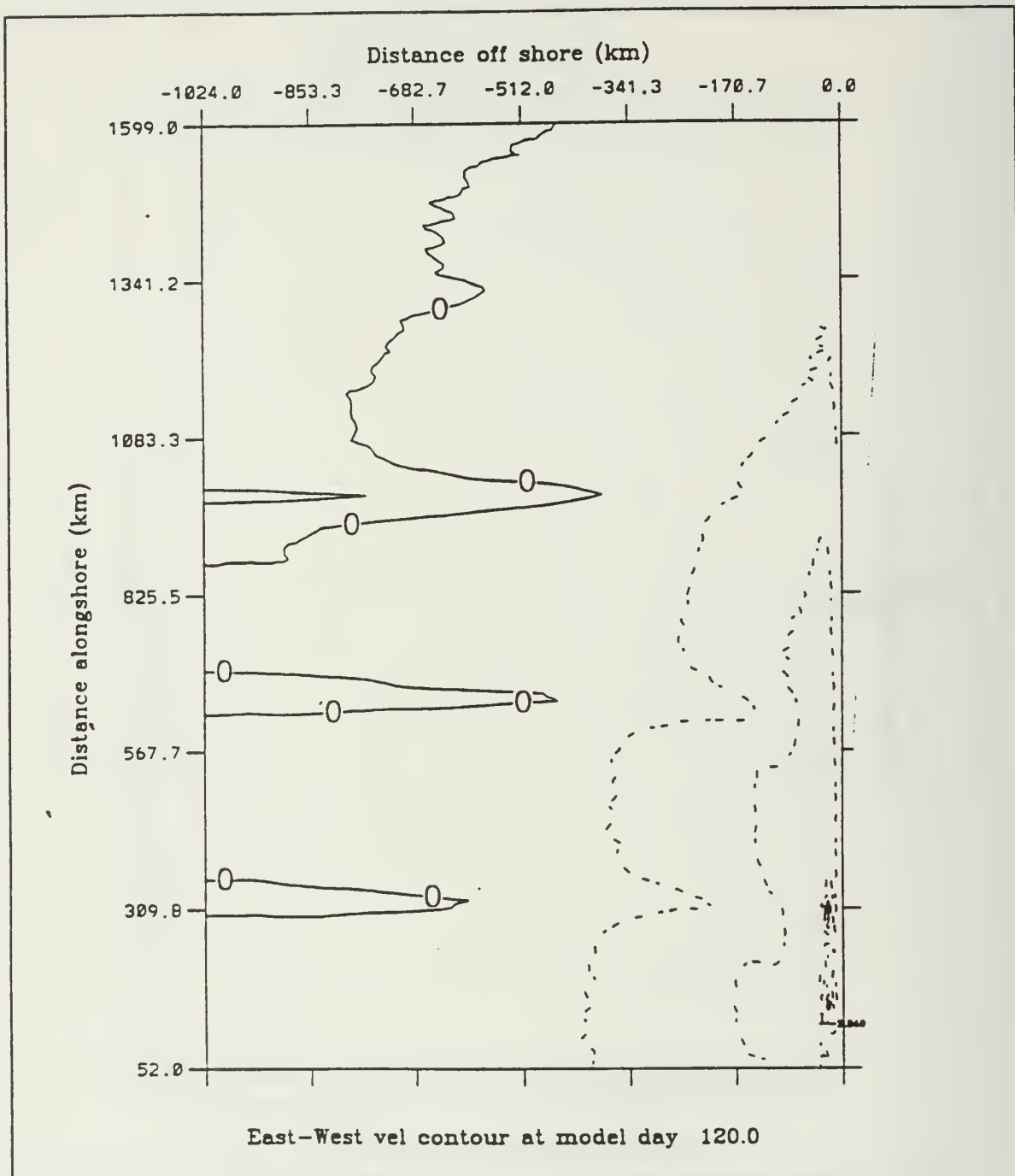


Figure 4.3 Experiment 1: Surface zonal velocity contours at day 120. The contour interval is  $2 \text{ cm s}^{-1}$ . Dashed lines indicate offshore velocities.



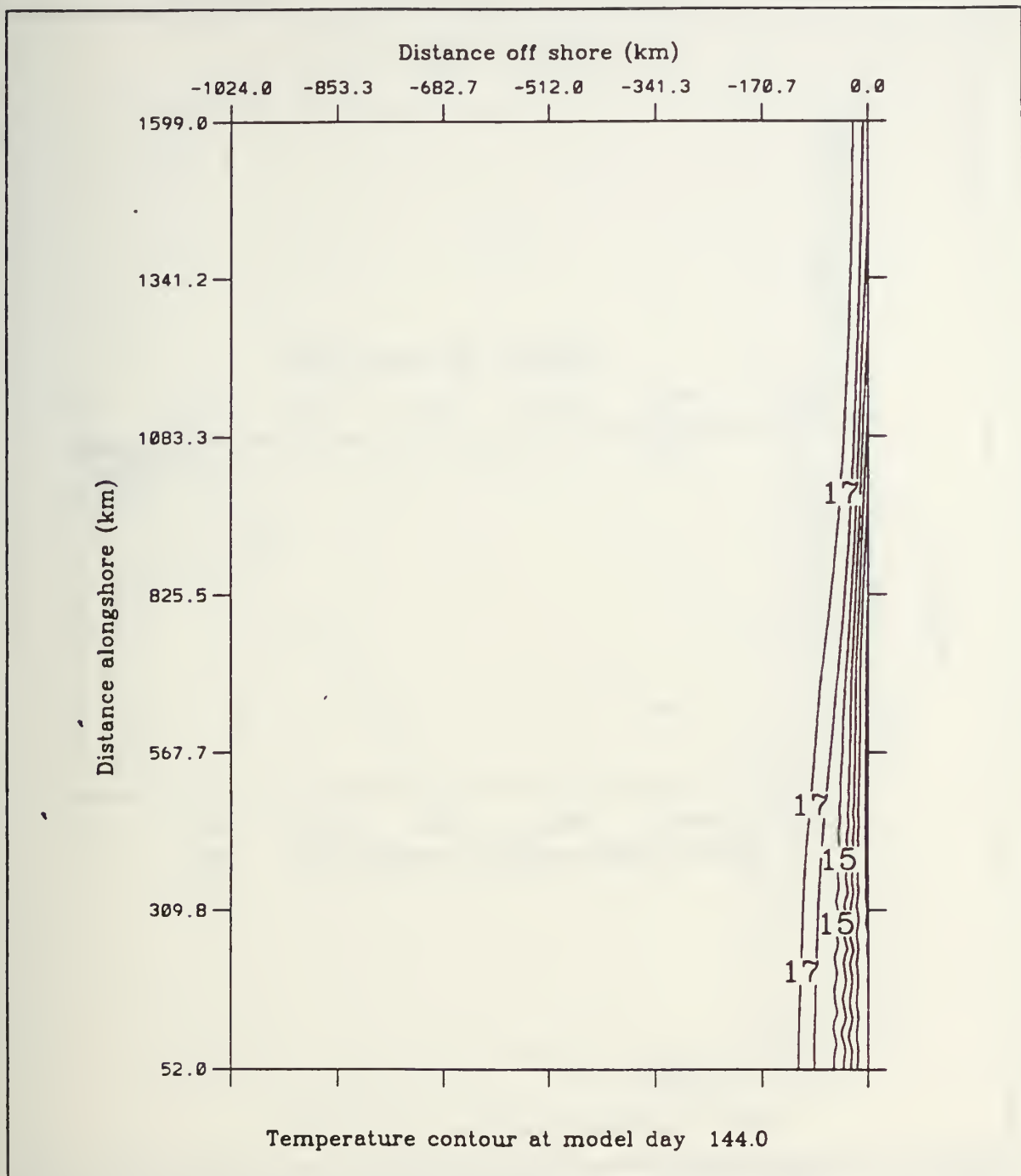


Figure 4.4) Experiment 1: Surface temperature contours at day 144. The contour interval is 1°C.

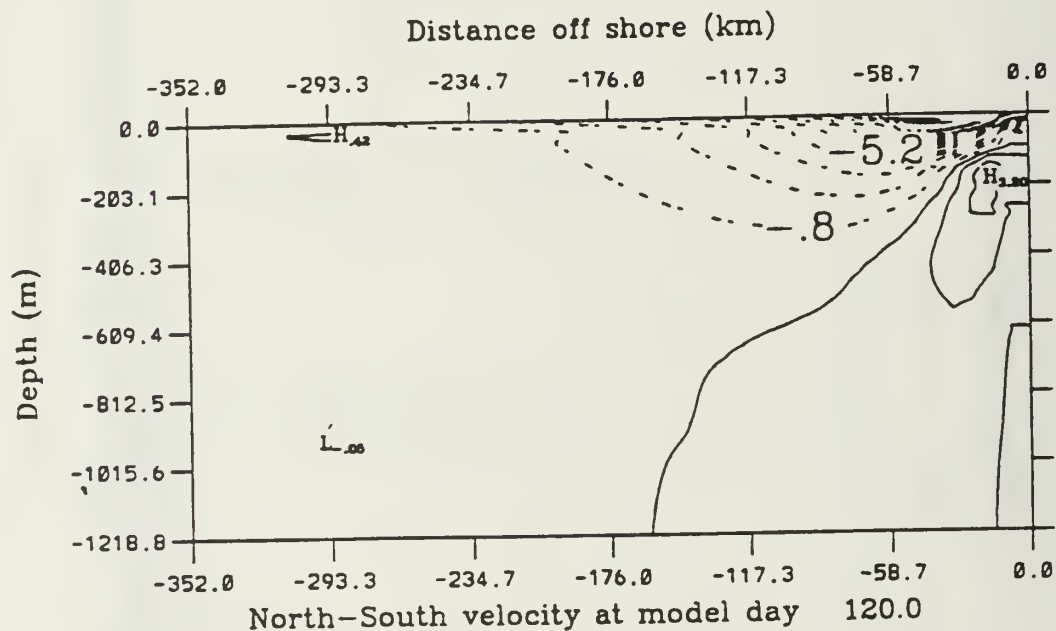


Figure 4.5 Experiment 1: Cross-section of meridional velocity contours at approximately 43°N at day 120. The contour interval is 1.1 cm s<sup>-1</sup>. Maximum values contoured are +/- 25 cm s<sup>-1</sup>. Dashed lines indicate southward flow and show the equatorward surface current. Solid lines indicate northward flow and show the poleward undercurrent.

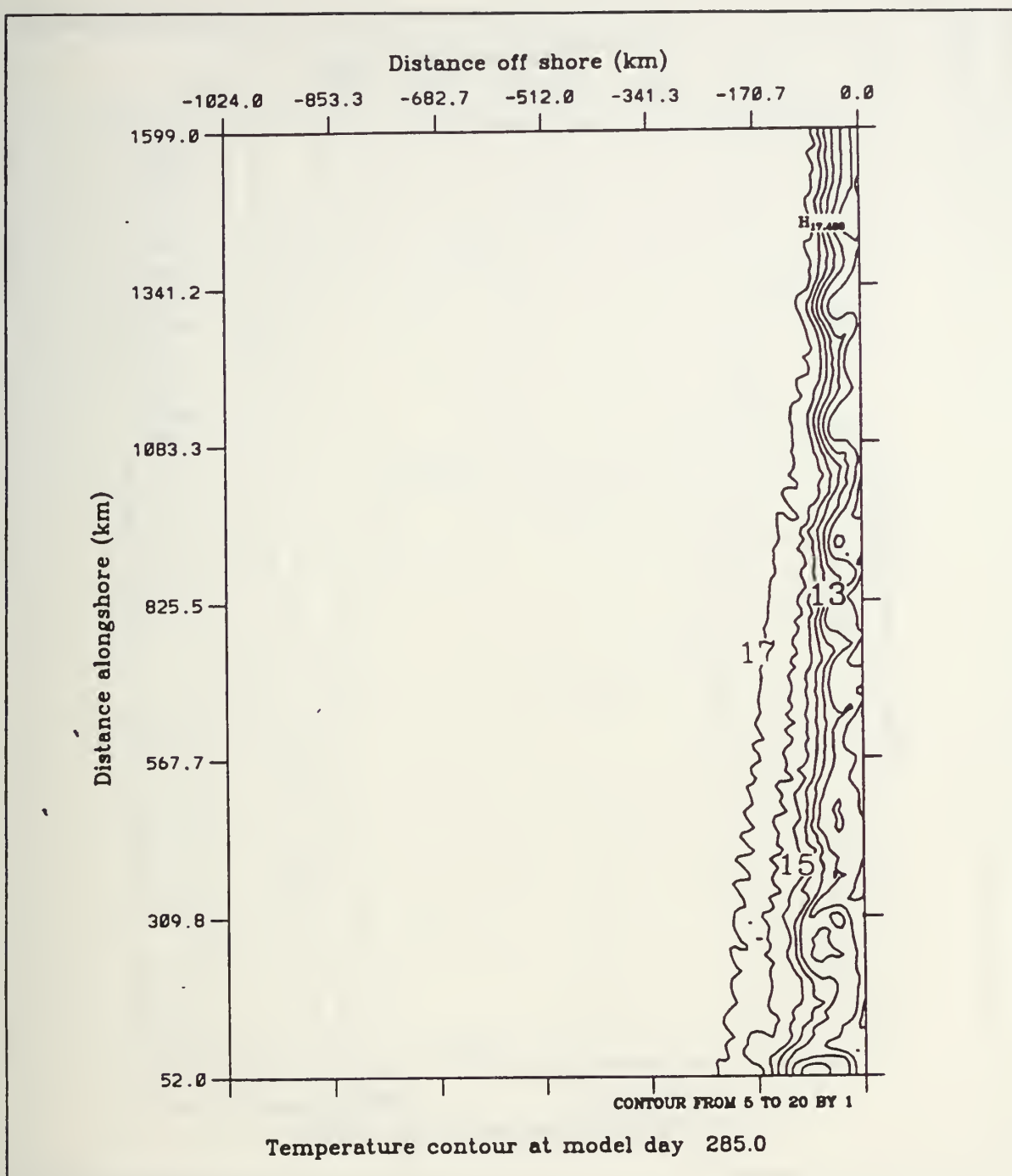


Figure 4.6a) Experiment 1: Surface temperature contours at day 285. The contour interval is 1°C. Temperature decreases toward the coast.

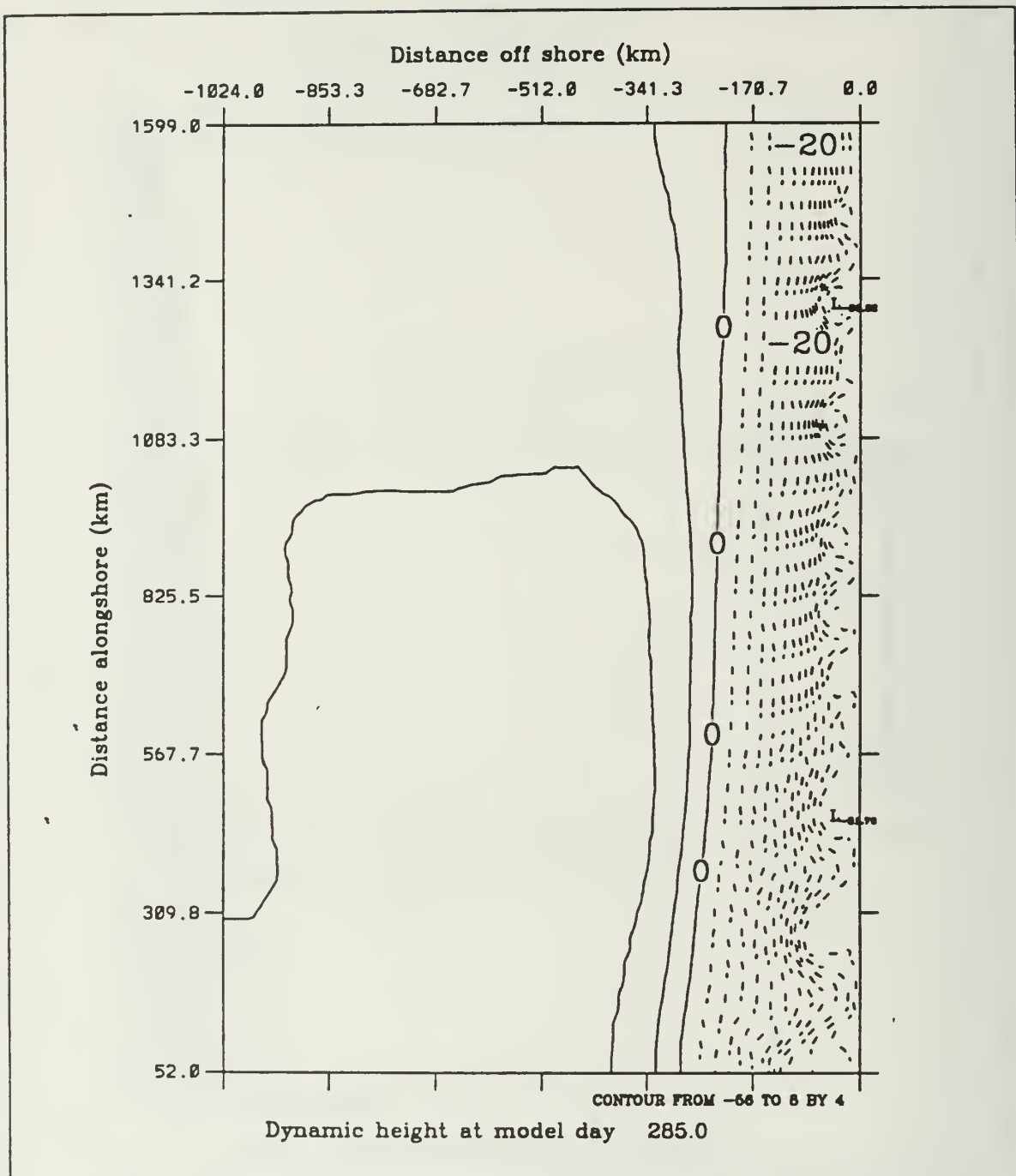


Figure 4.6b) Experiment 1: Surface dynamic height (relative to 2500 m) at day 285. The contour interval is 1 cm. Dashed lines indicate negative dynamic height.



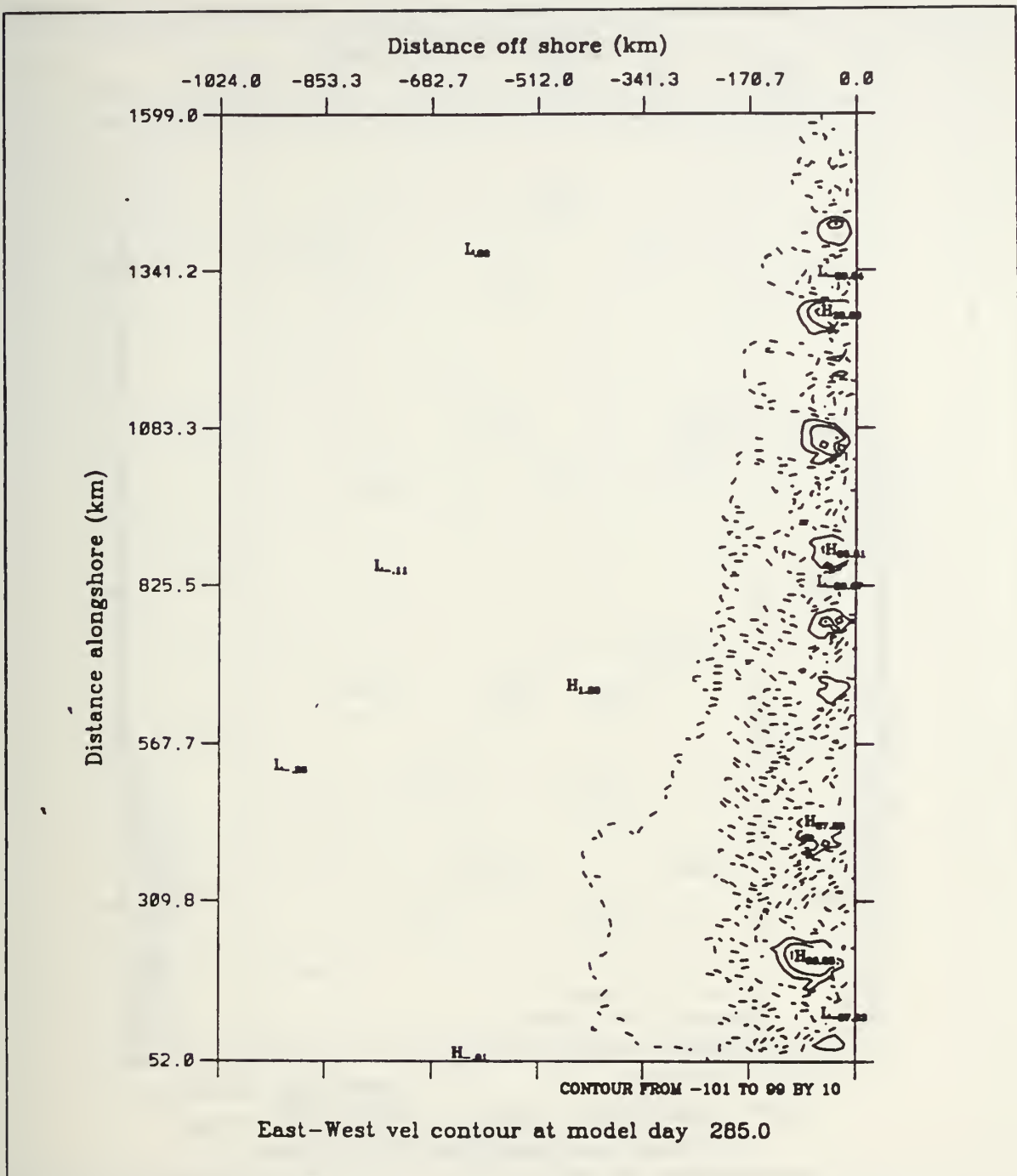


Figure 4.6c) Experiment 1: Surface zonal velocity contours at day 285. Contour interval is 10 cm s<sup>-1</sup>. Dashed lines indicate offshore flow.



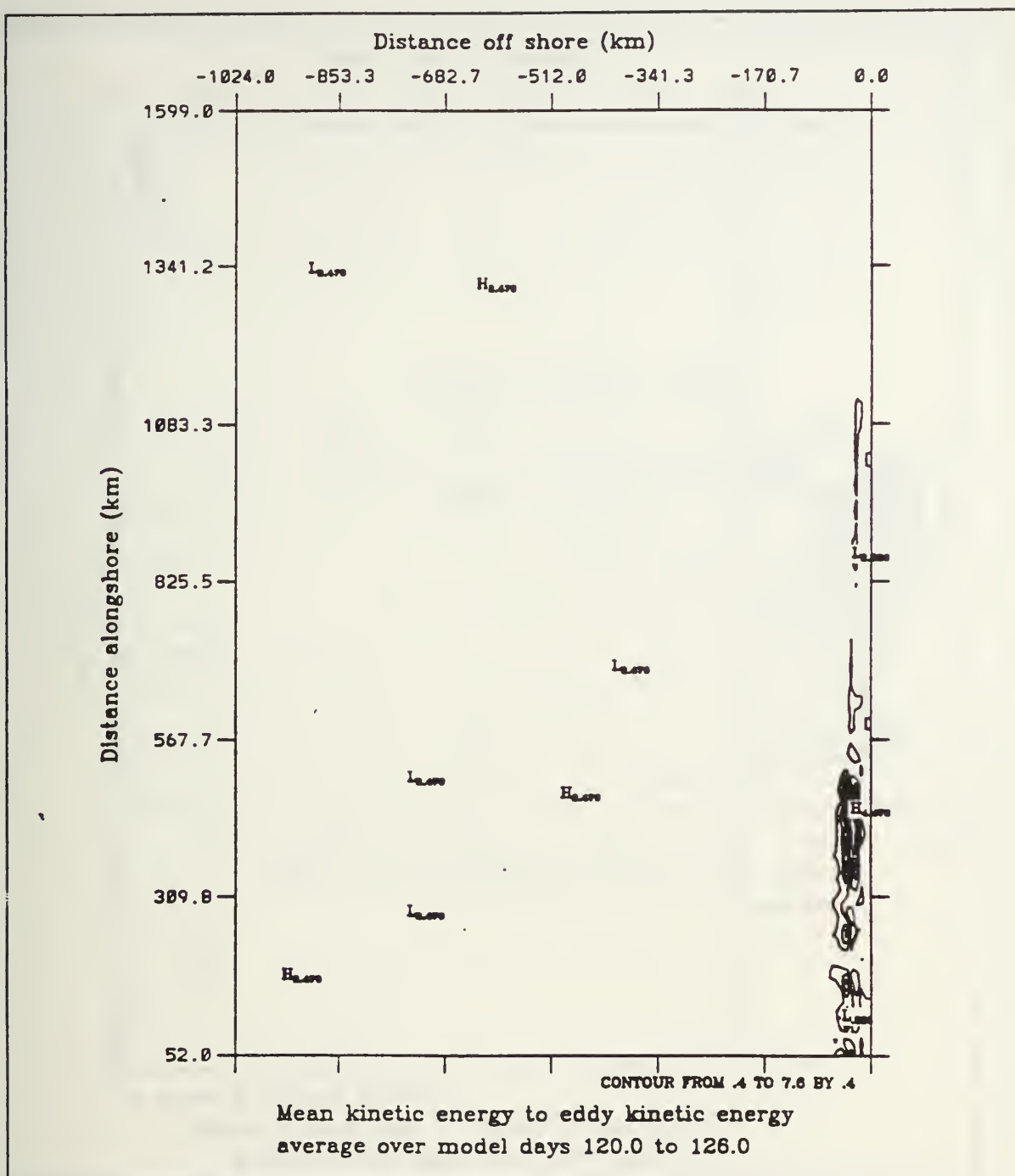


Figure 4.7b) Experiment 1: Barotropic transfer of energy (as defined in equation 3.19) from K to K' (mean to eddy kinetic energy). Transfer of energy is averaged over the days 120 to 126 and summed over the upper five layers. The contour interval is  $0.4 \text{ ergs cm}^{-3} \text{ s}^{-1}$ .

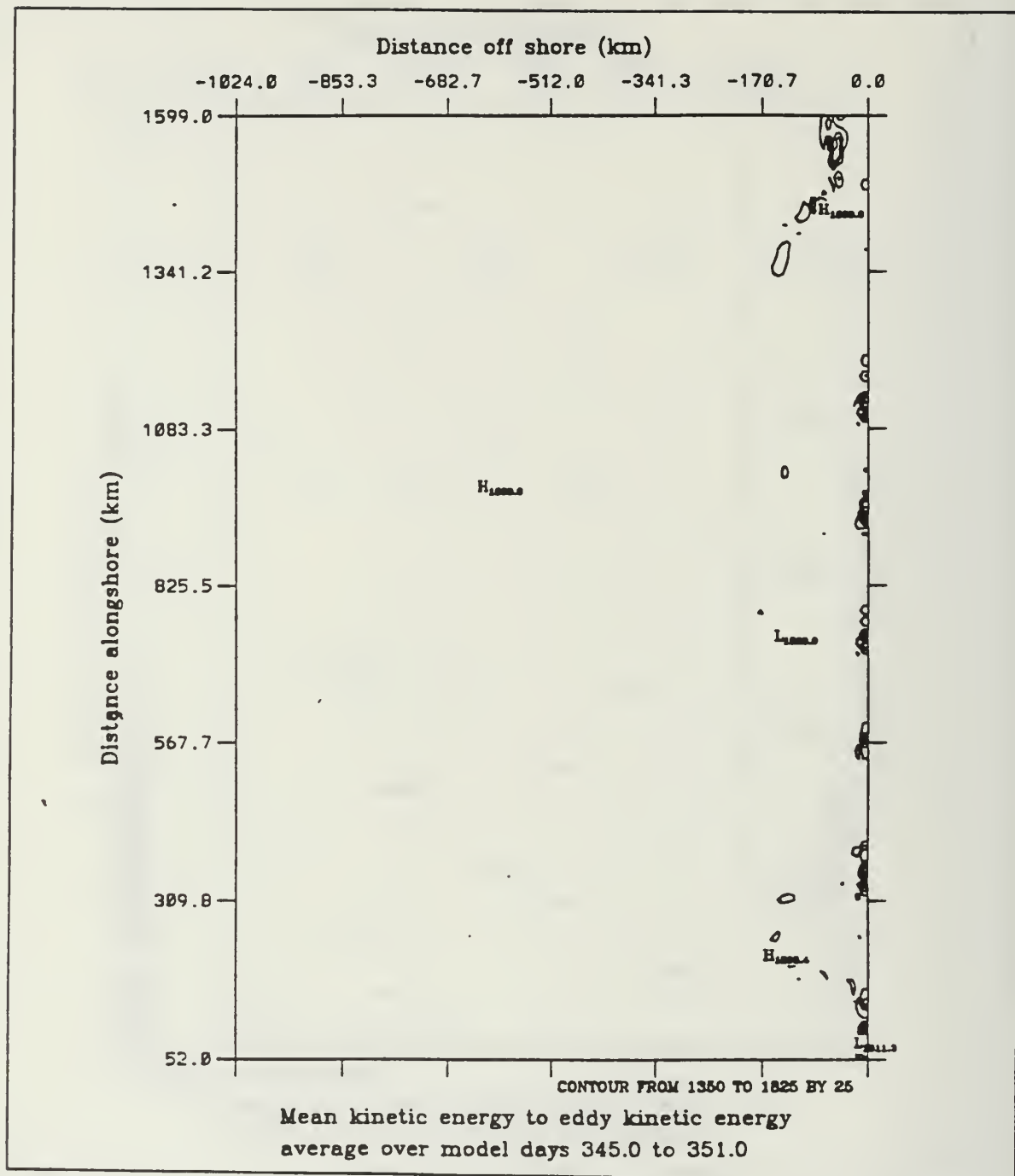


Figure 4.8 Experiment 1: Barotropic transfer of energy (as defined in equation 3.19) from K to K' (mean to eddy kinetic energy). Transfer of energy is averaged over the days 345 to 351 and summed over the upper five layers. The contour interval is 25 ergs  $\text{cm}^{-3} \text{s}^{-1}$ .



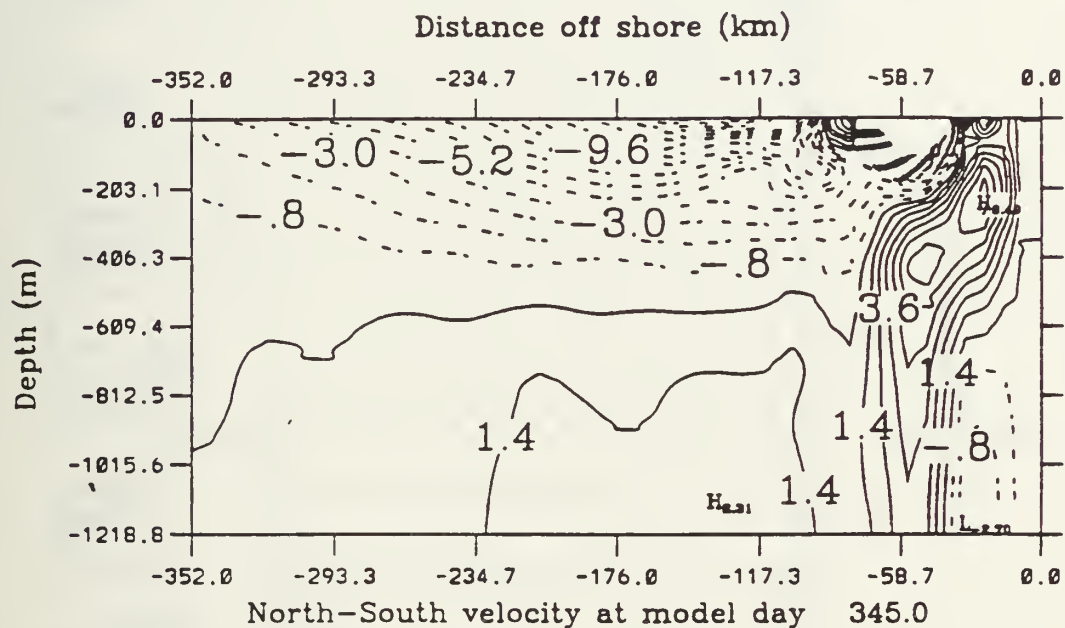


Figure 4.9 Experiment 1: Cross-section of meridional velocity contours at approximately  $46.5^{\circ}\text{N}$  at day 345. Contour interval is  $1.1 \text{ cm s}^{-1}$ . Maximum values contoured are  $\pm 25 \text{ cm s}^{-1}$ . The dashed lines indicate southward flow and show the equatorward surface current. The solid lines indicate northward flow and show the poleward current.

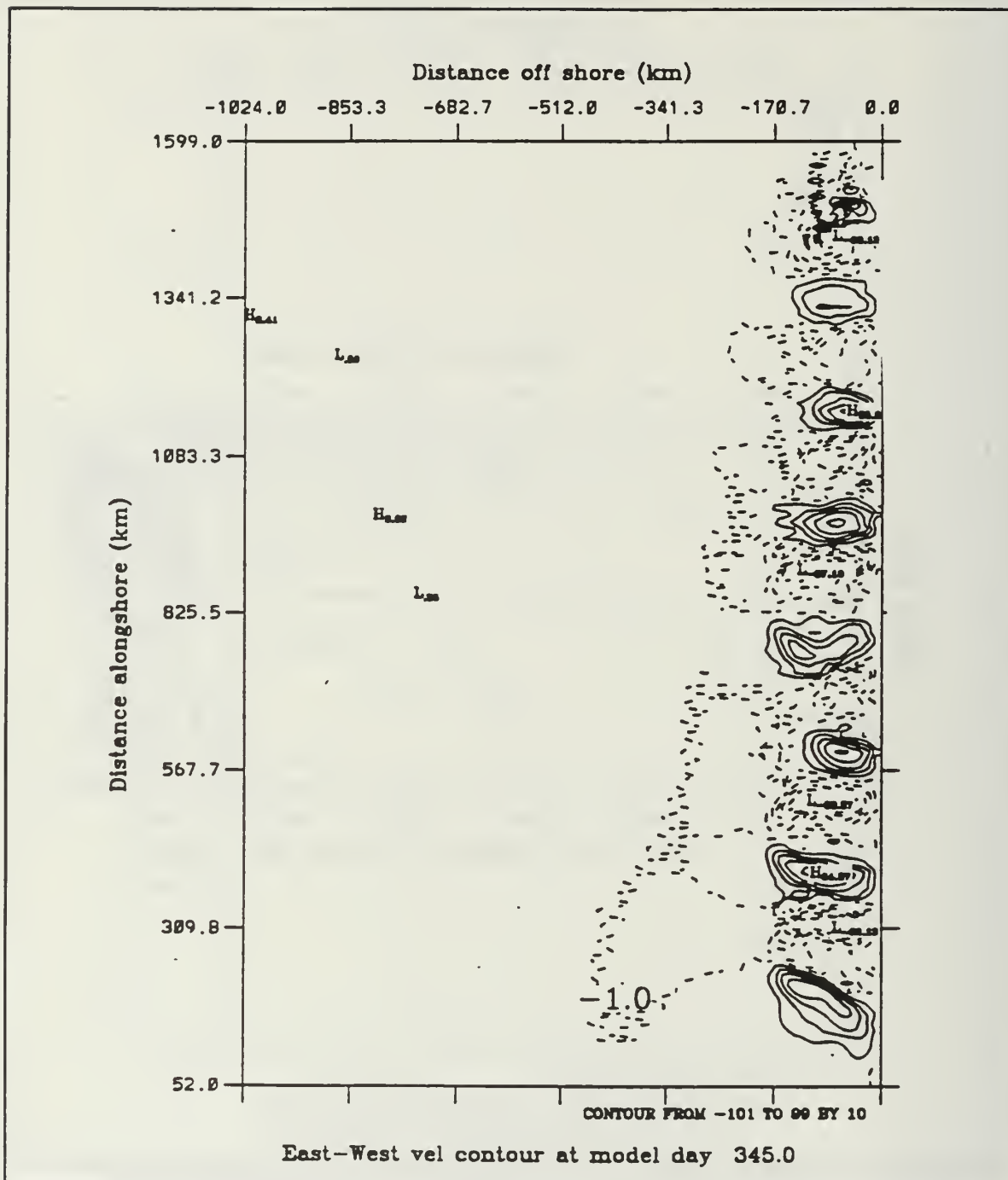


Figure 4.10 Experiment 1: Surface zonal velocity contours at day 345. Contour interval is 10 cm s<sup>-1</sup>. Dashed lines indicate offshore velocity.

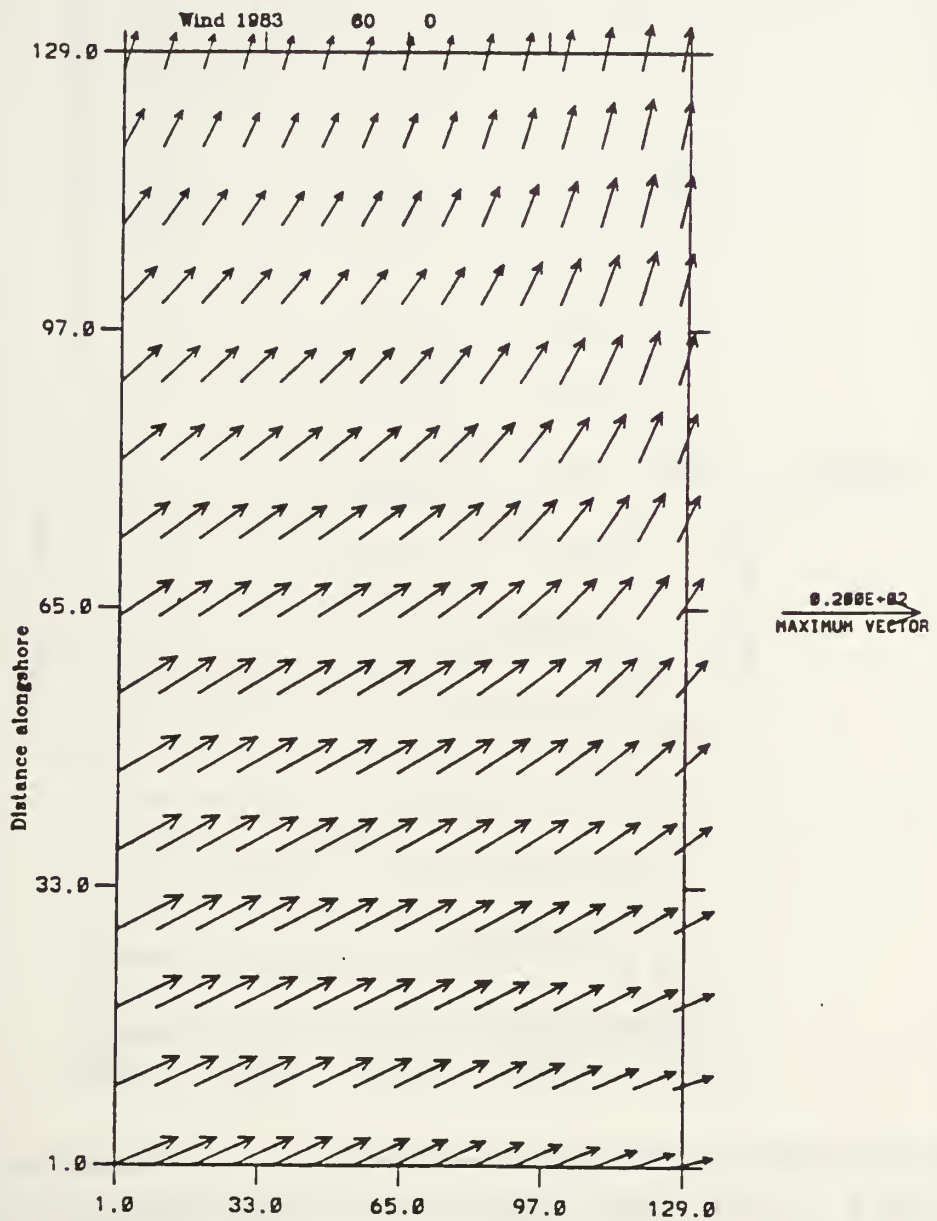


Figure 4.11a) Experiment 5: 1983 Wind forcing in  $\text{m s}^{-1}$  at day 60. As in Fig. 4.1a.

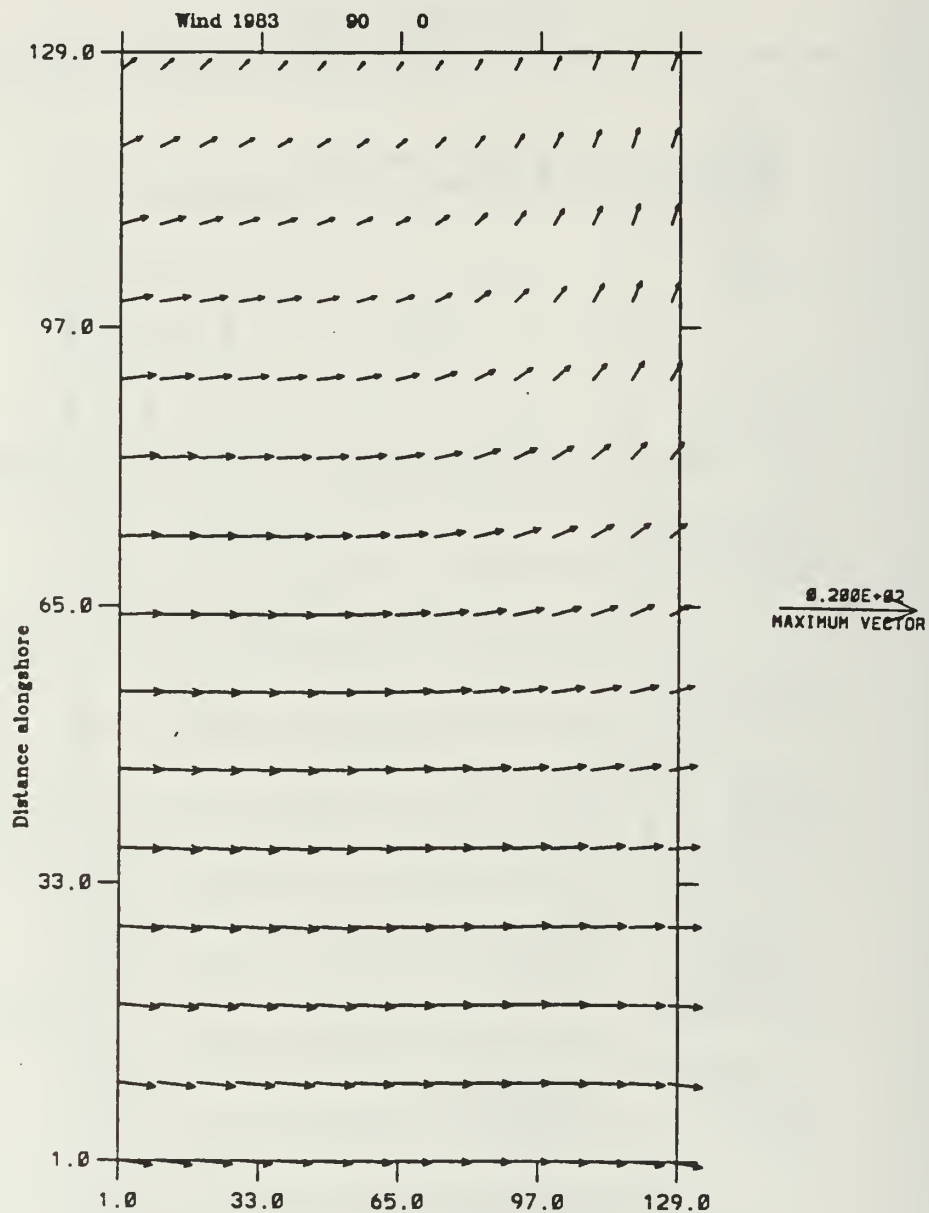


Figure 4.11b) Experiment 5: 1983 Wind forcing in  $\text{m s}^{-1}$  at day 90. As in Fig. 4.1a.

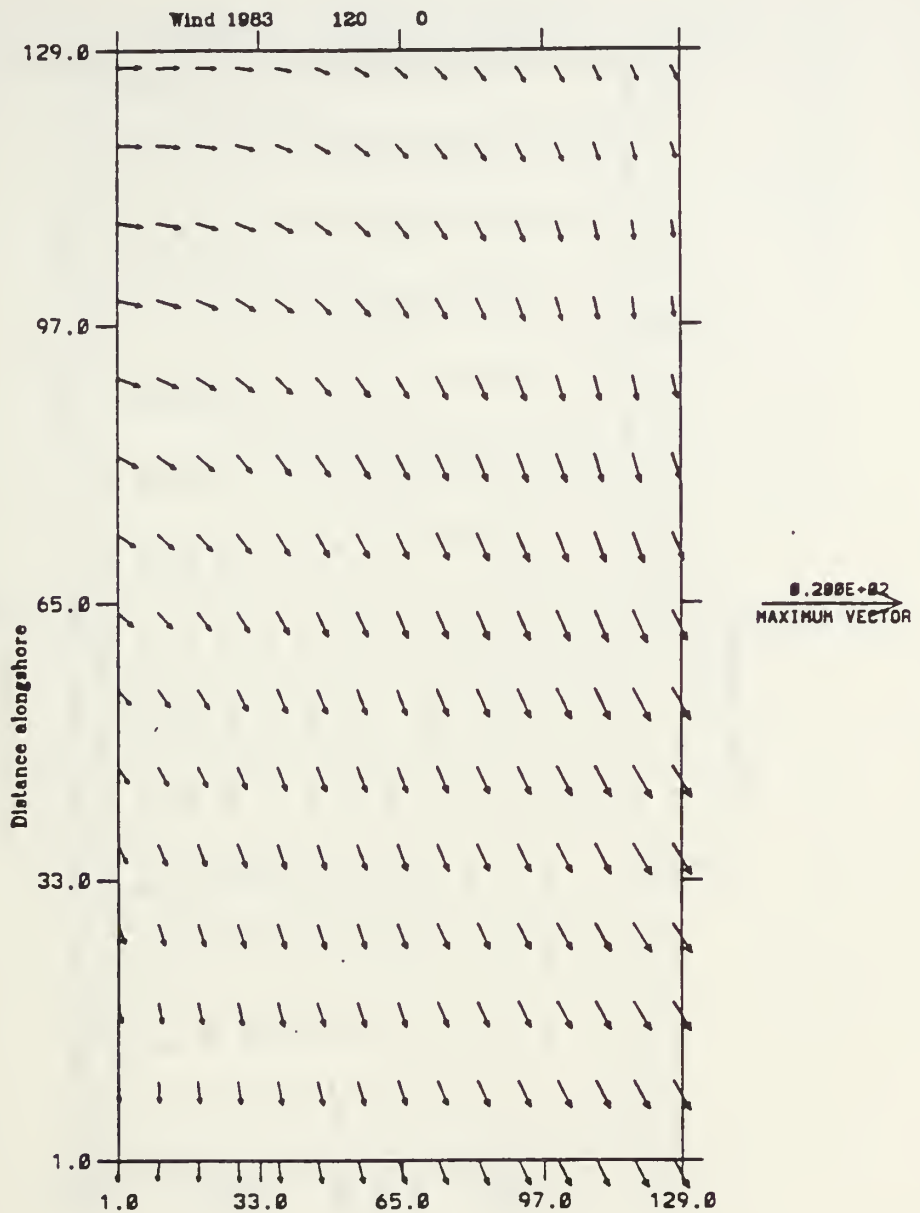


Figure 4.11c) Experiment 5: 1983 Wind forcing in  $\text{m s}^{-1}$  at day 120. As in Fig. 4.1a.



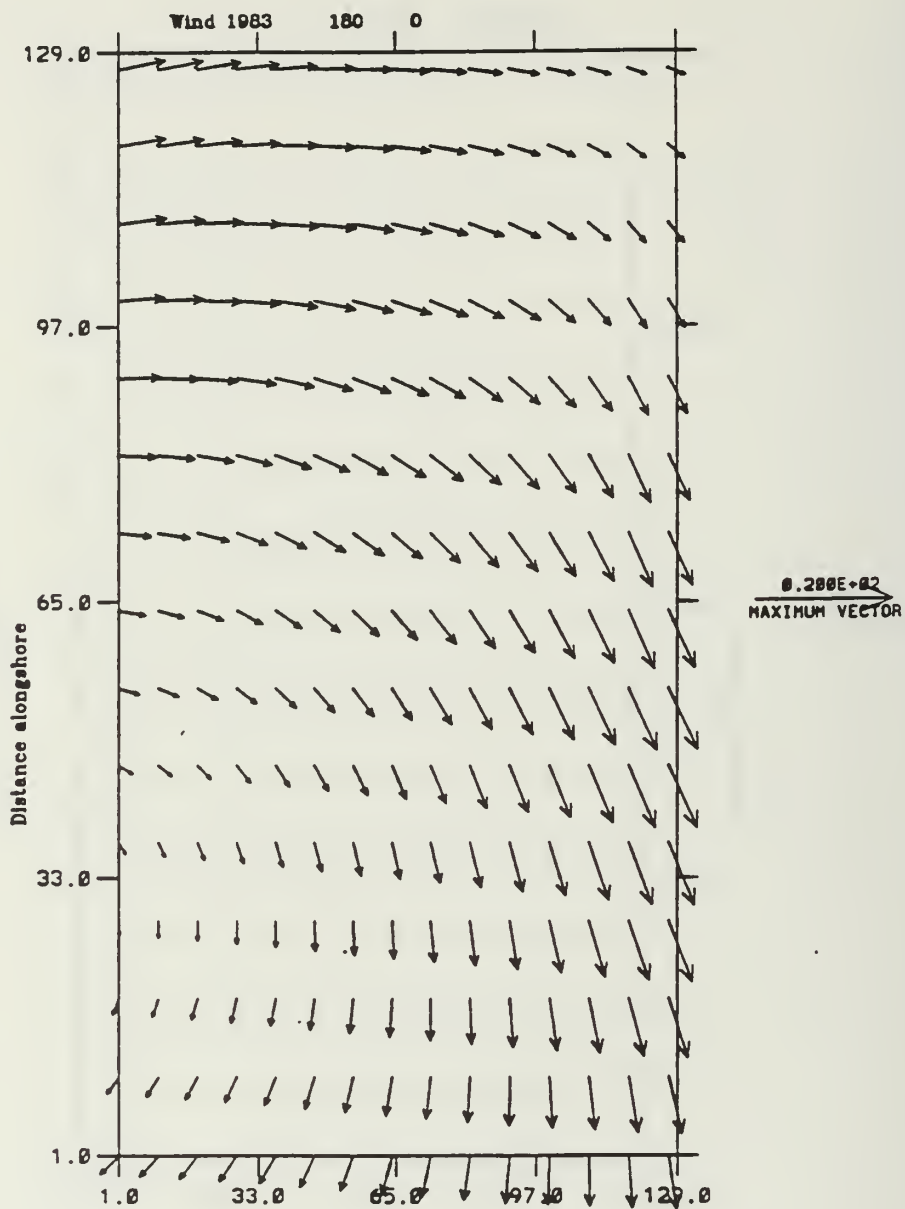


Figure 4.11d) Experiment 5: 1983 Wind forcing in  $\text{m s}^{-1}$  at day 180. As in Fig. 4.1a.

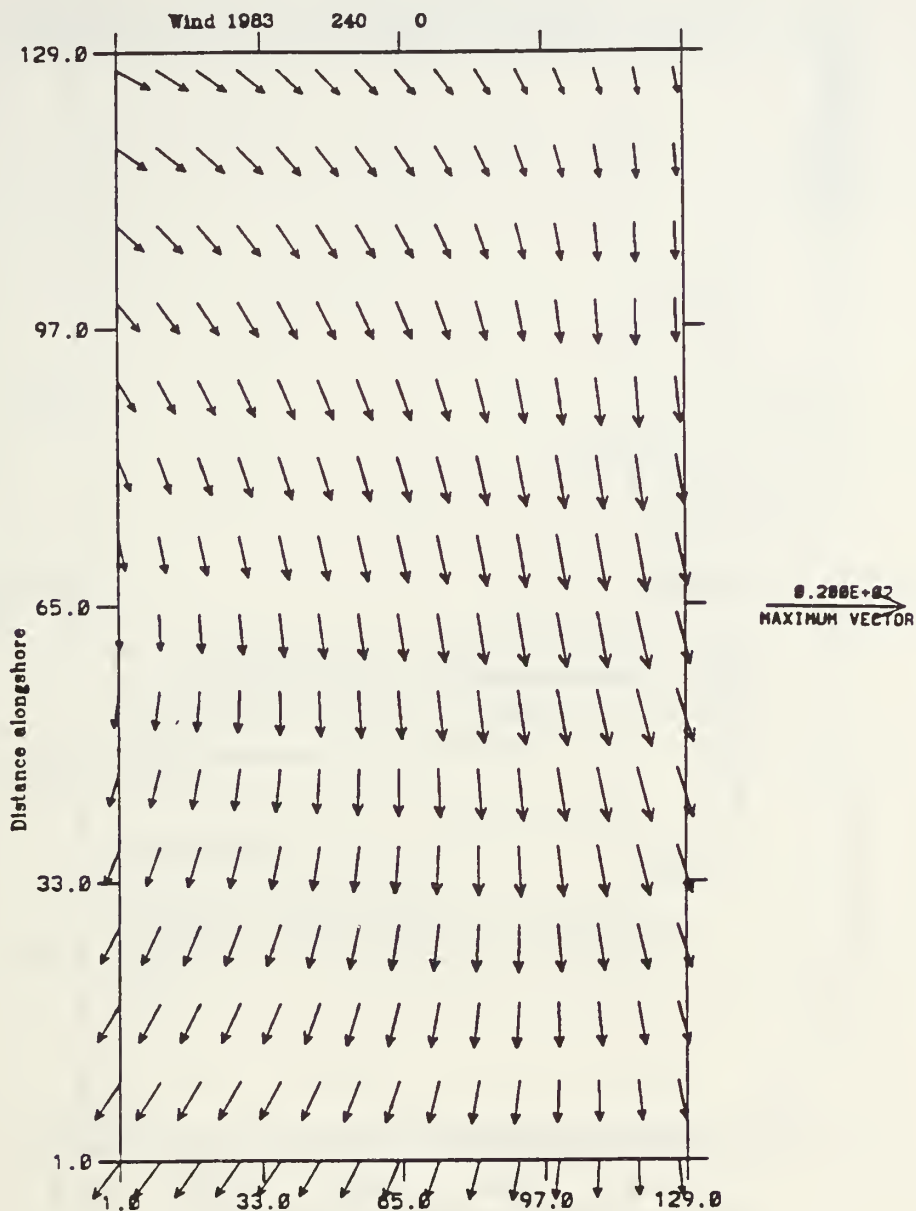


Figure 4.11e) Experiment 5: 1983 Wind forcing in  $\text{m s}^{-1}$  at day 240. As in Fig. 4.1a.

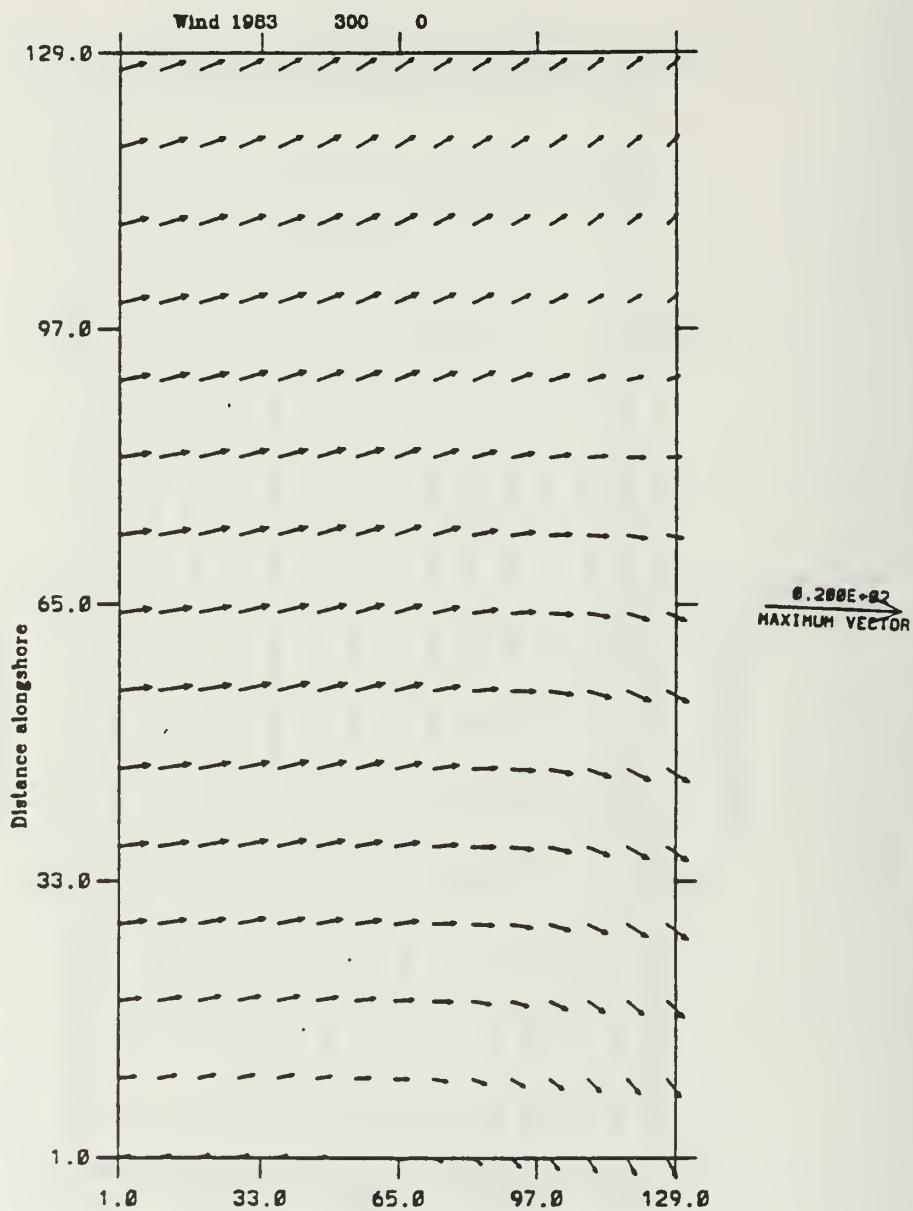


Figure 4.11f) Experiment 5: 1983 Wind forcing in  $\text{m s}^{-1}$  at day 300. As in Fig. 4.1a.

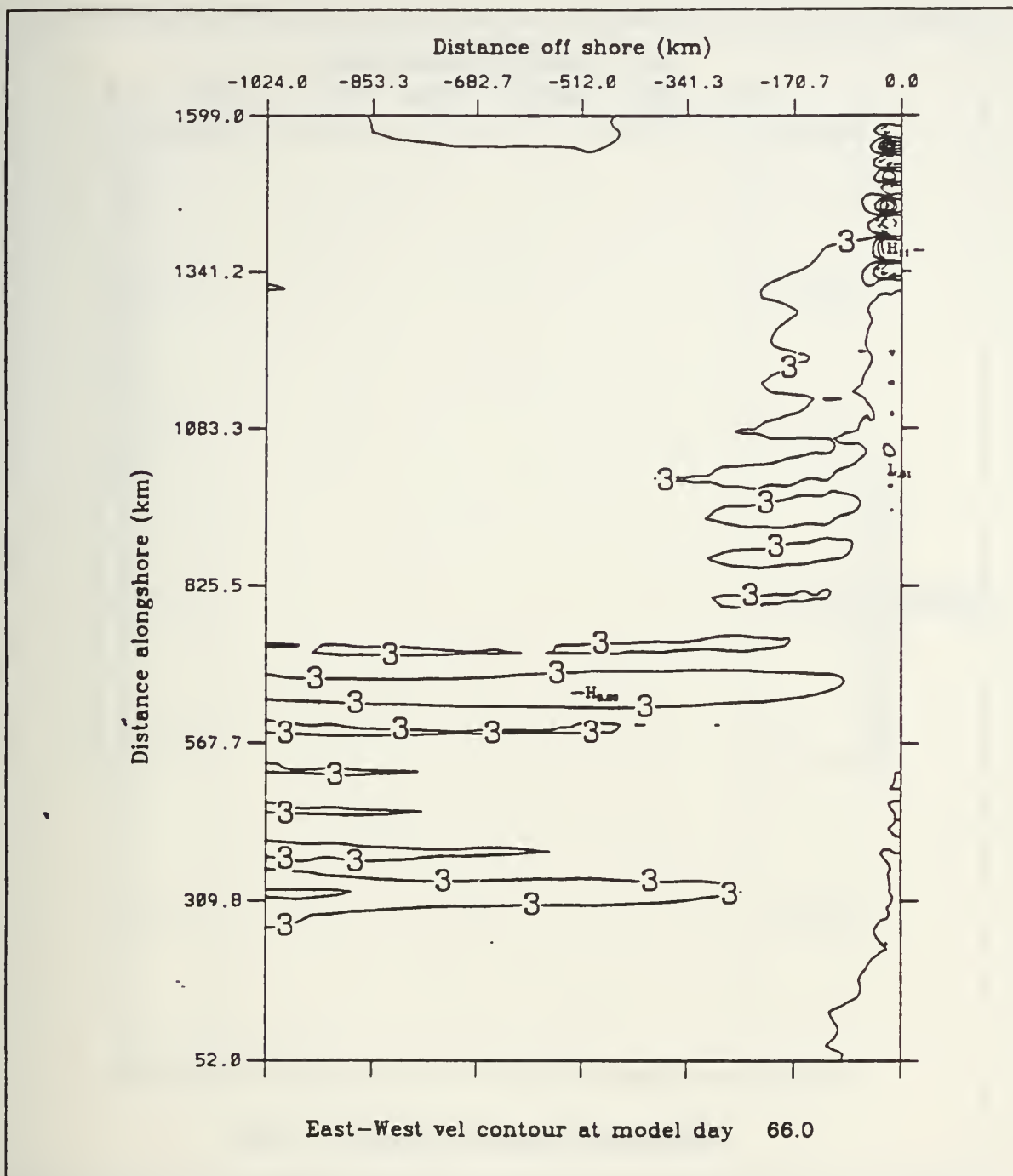


Figure 4.12a) Experiment 5: Surface zonal velocity contours at day 66. Contour interval is  $2 \text{ cm s}^{-1}$ . Dashed lines indicate offshore velocity.

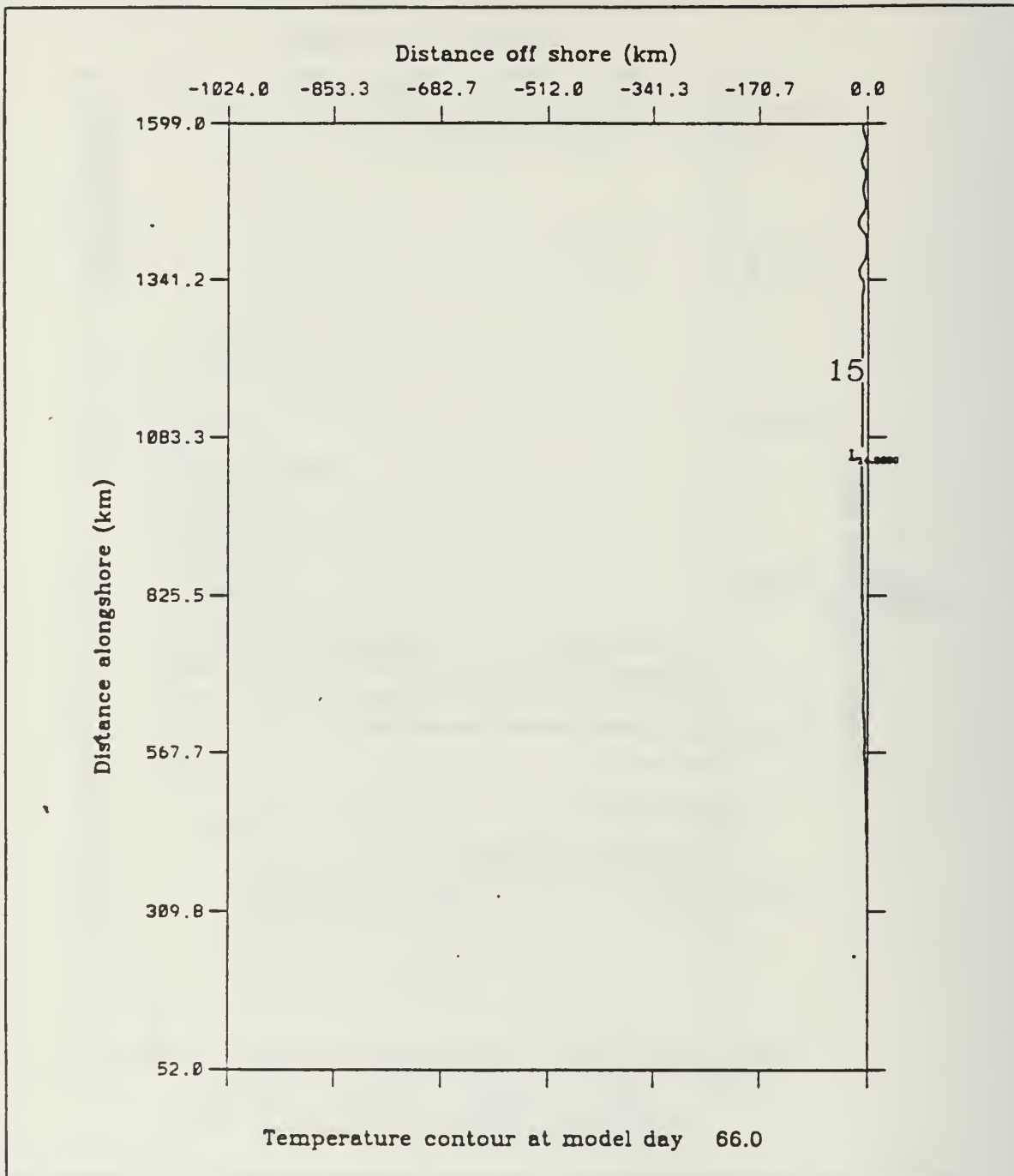


Figure 4.12b) Experiment 5: Surface temperature contours at day 66. Contour interval is 1°C. Temperature decreases toward the coast.



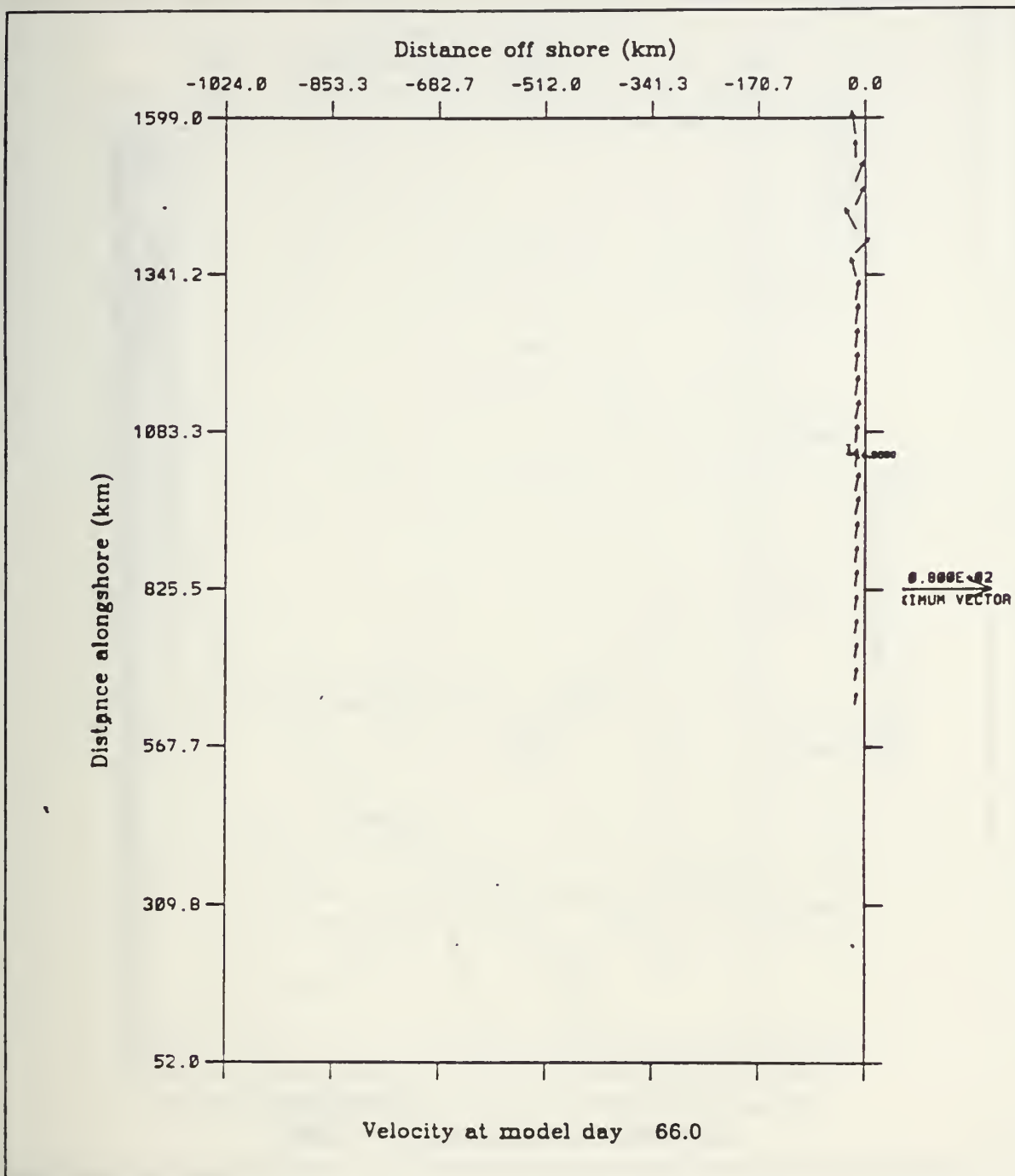


Figure 4.12c) Experiment 5: Surface velocity in  $\text{cm s}^{-1}$  at day 66. As in Fig. 4.2a.

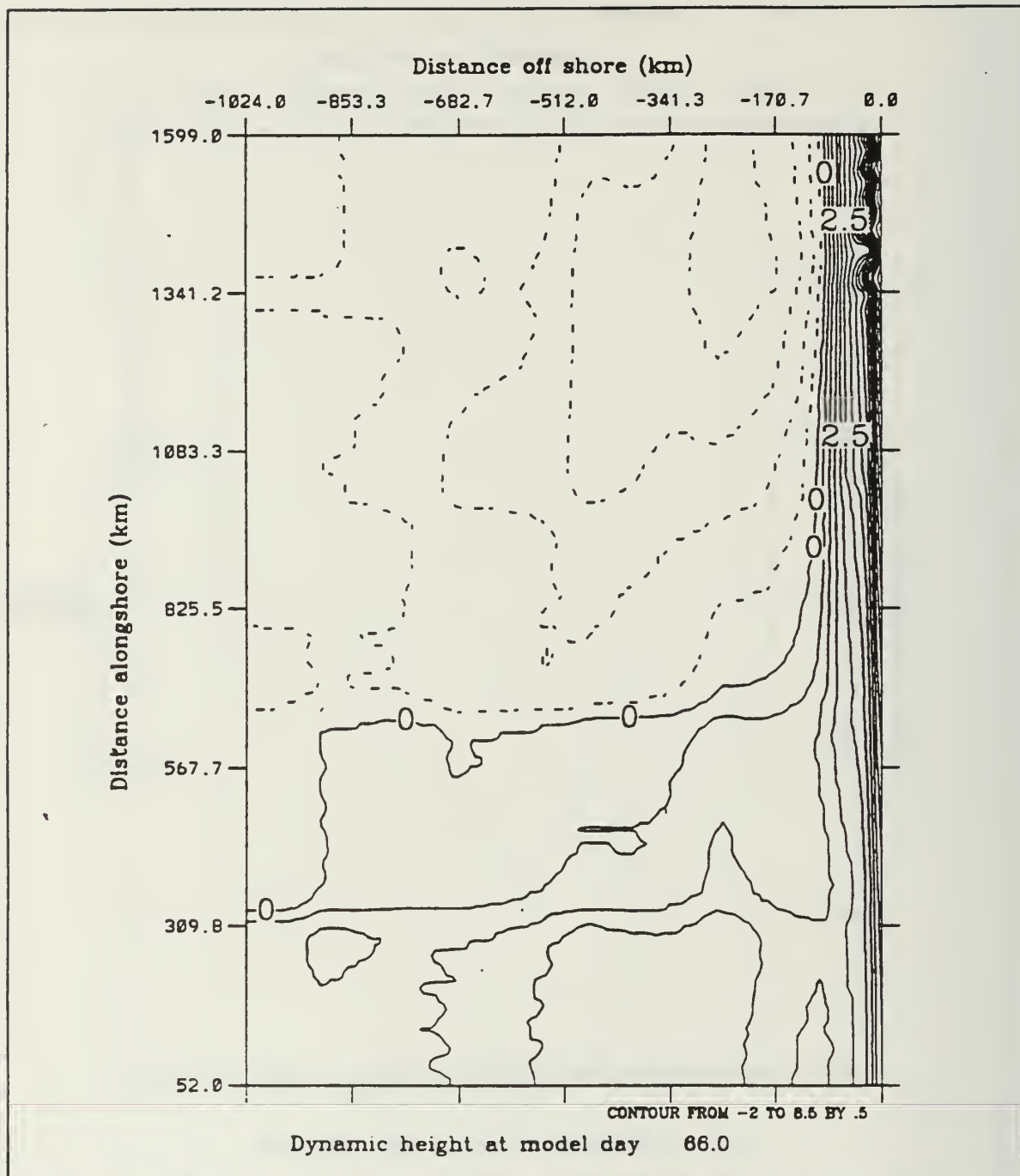
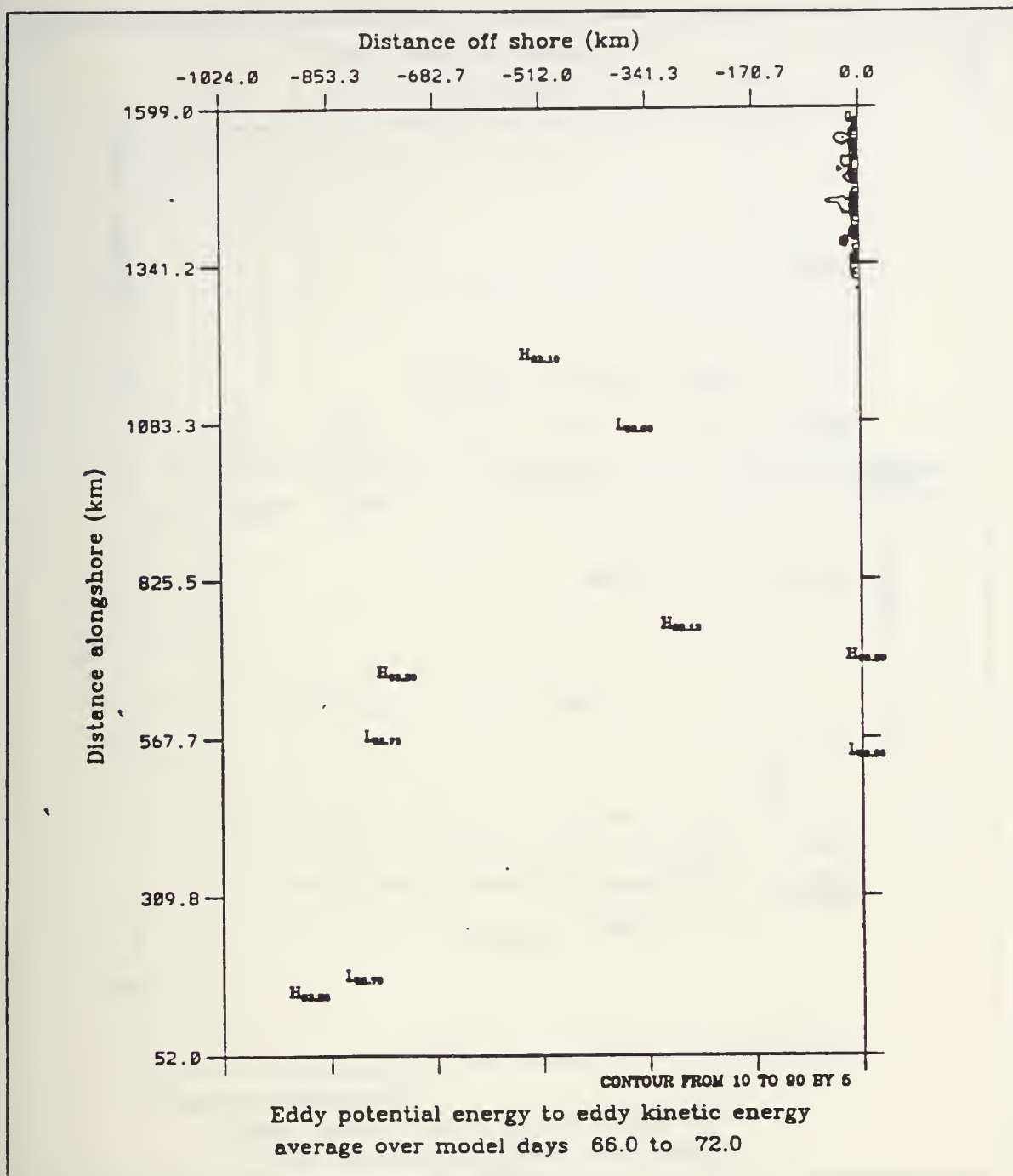


Figure 4.12d) Experiment 5: Surface dynamic height (relative to 2500 m) contours at day 66. Contour interval is 0.5 cm. Dashed lines indicate negative dynamic height.



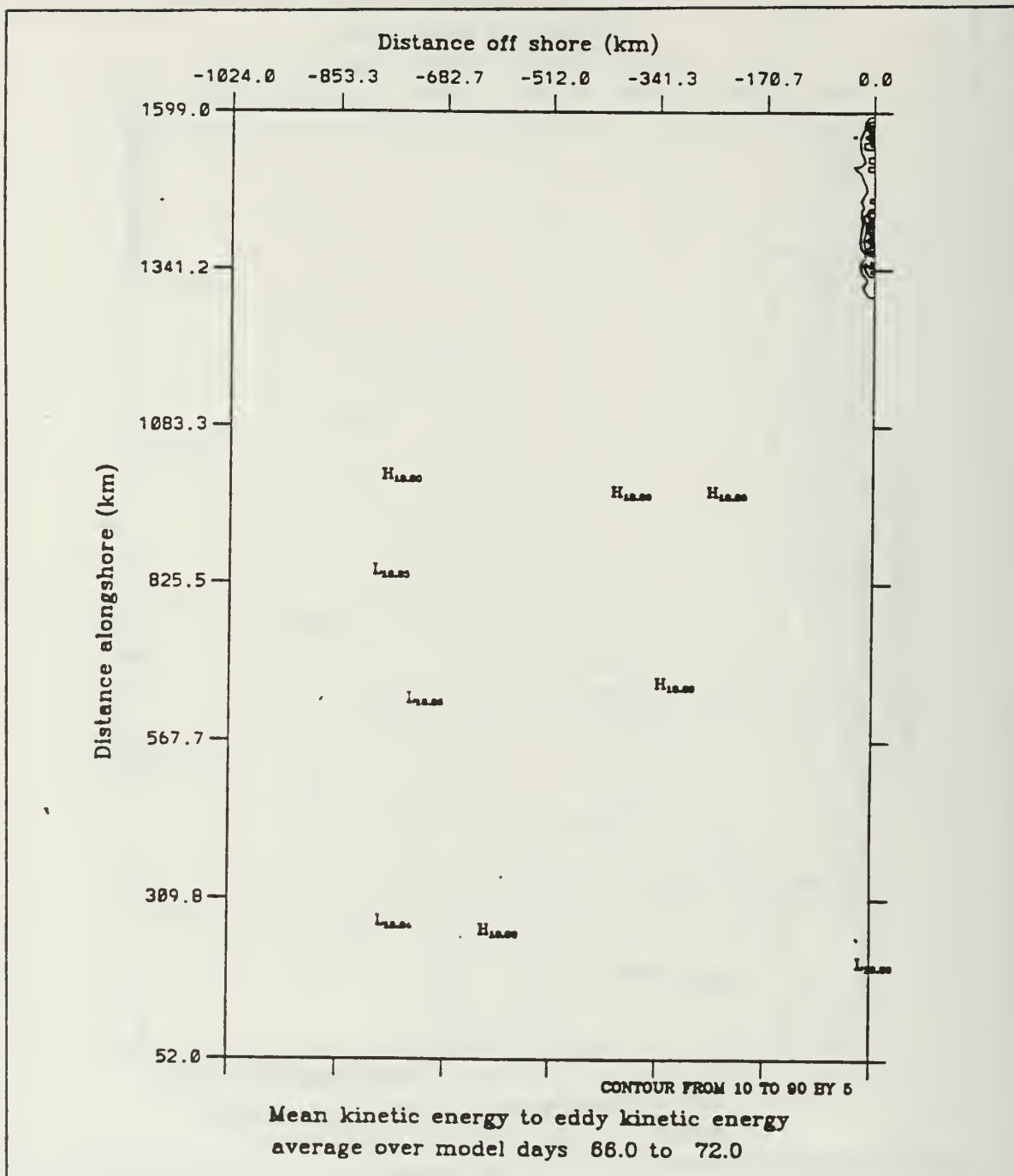


Figure 4.13b) Experiment 5: Barotropic transfer of energy (as defined in equation 3.19) from  $K$  to  $K'$  (mean to eddy kinetic energy). Transfer of energy is averaged over the days 66 to 72 and summed over the upper five layers. The contour interval is  $5 \text{ ergs cm}^{-3} \text{ s}^{-1}$ .

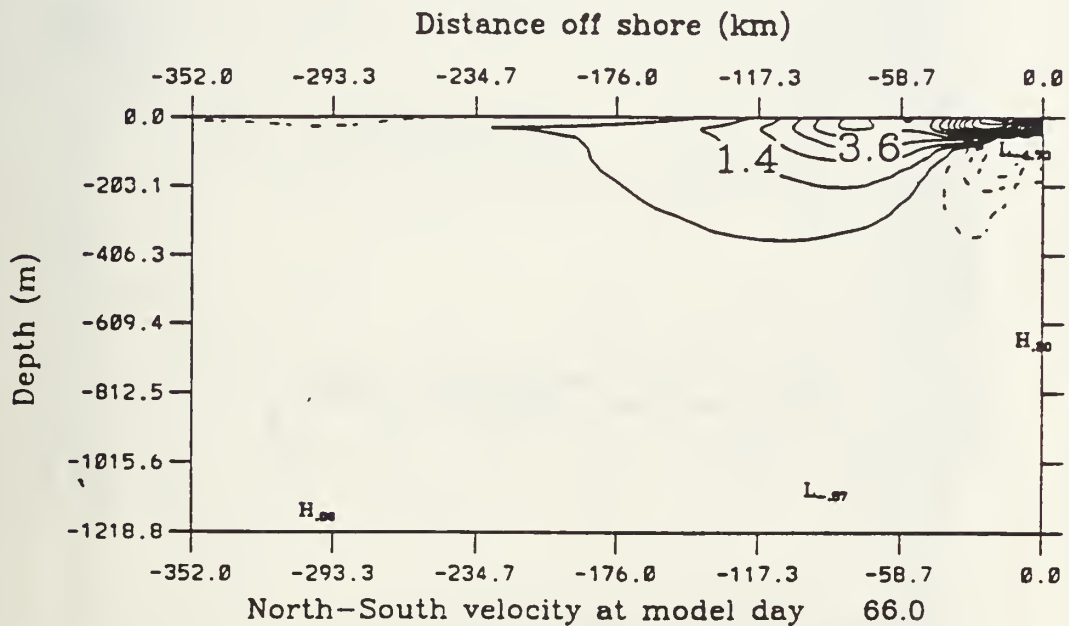


Figure 4.14 Experiment 5: Cross-section of meridional velocity contours at approximately 47°N at day 66. Solid lines indicate northward flow. Dashed lines indicate equatorward flow. Contour interval is 1.1 cm s<sup>-1</sup>.



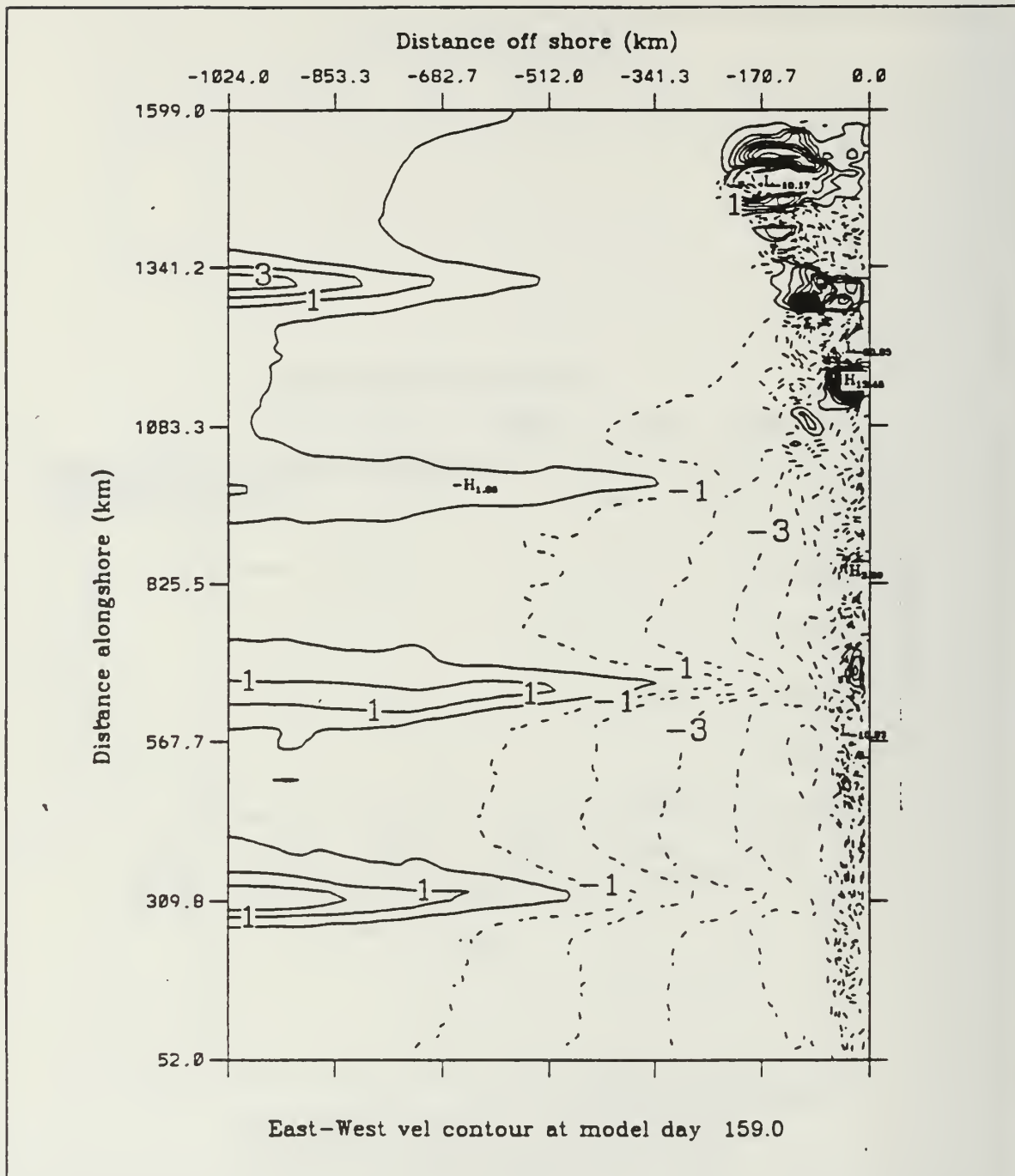


Figure 4.15a) Experiment 5: Surface zonal velocity contours at day 159. Contour interval is  $1 \text{ cm s}^{-1}$ . Dashed lines indicate offshore flow.

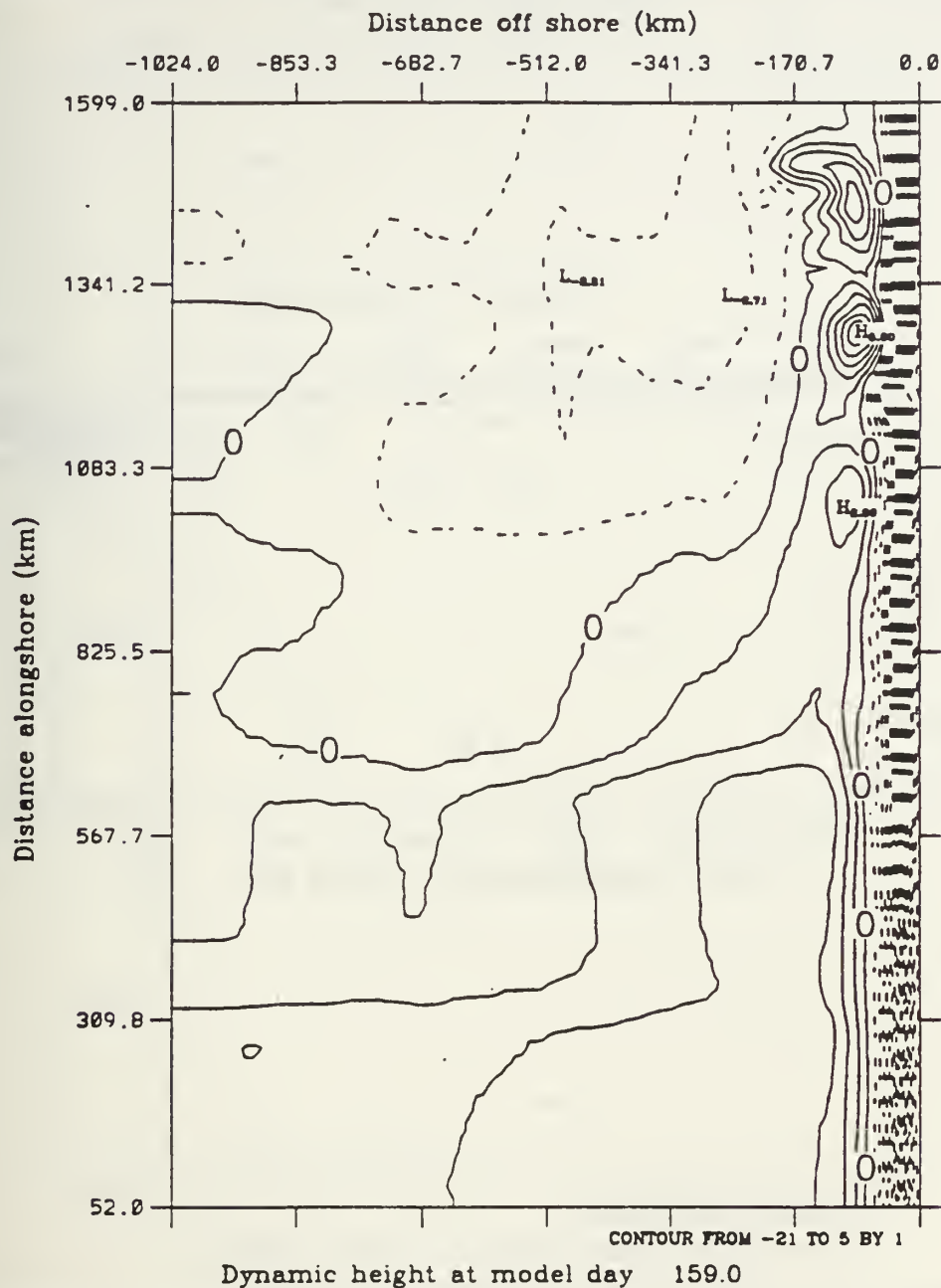


Figure 4.15b) Experiment 5: Surface dynamic height (relative to 2500 m) contours at day 159. Dashed lines indicate negative dynamic heights. Contour interval is 1 cm.

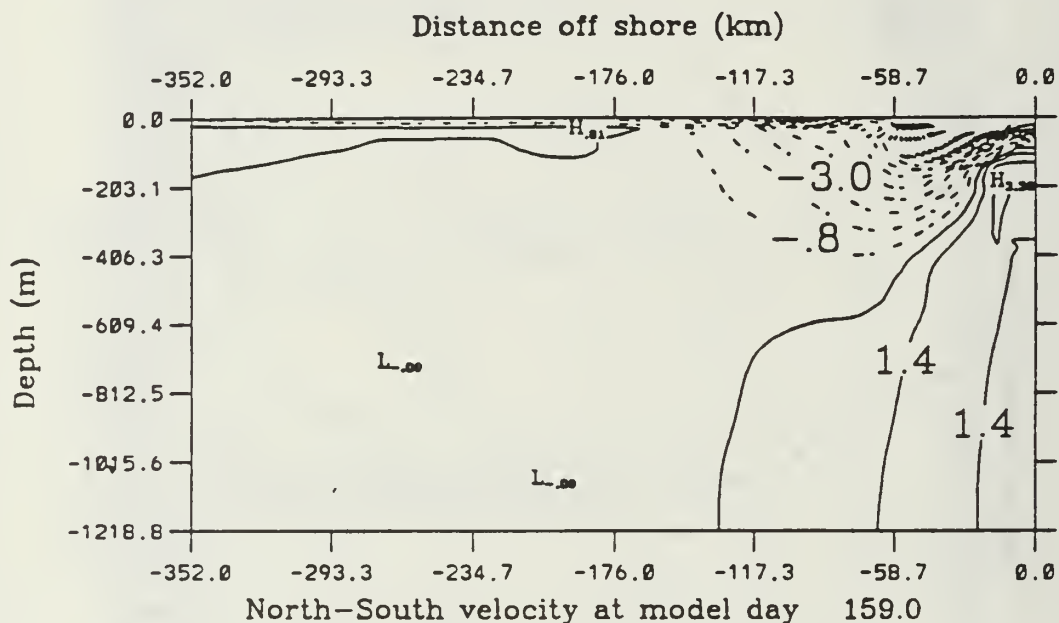


Figure 4.16 Experiment 5: Cross-section of meridional velocity contours at approximately  $41^{\circ}\text{N}$  at day 159. Dashed lines indicate southward flow and show the equatorward surface current. Solid lines indicate northward flow and indicate the poleward undercurrent. Contour interval is  $1.1 \text{ cm s}^{-1}$ . Maximum values shown are  $\pm 25 \text{ cm s}^{-1}$ .

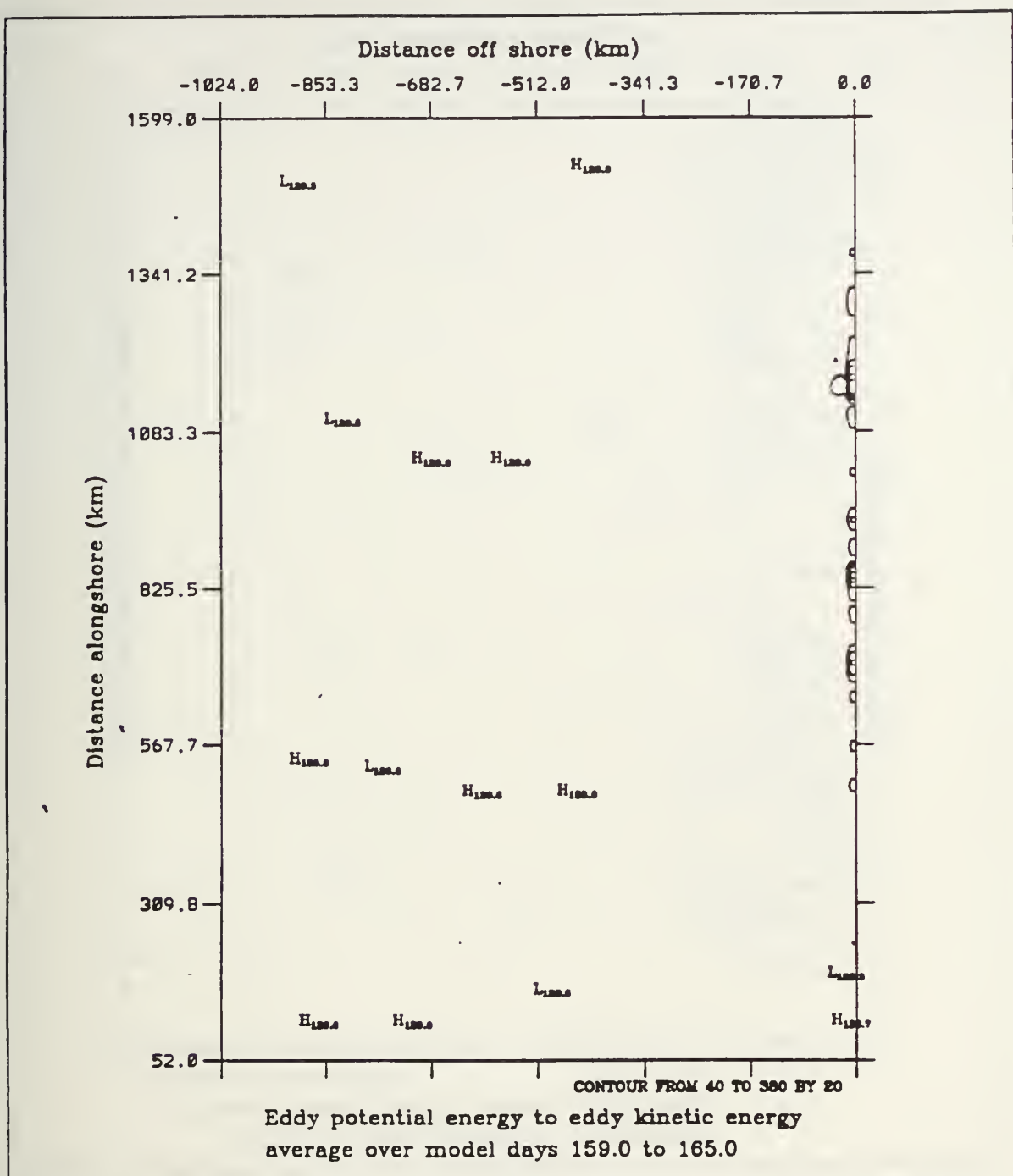


Figure 4.17a) Experiment 5: Baroclinic transfer of energy (as defined in equation 3.18) from  $P'$  to  $K'$  (eddy available to eddy kinetic energy). Transfer is averaged over days 159 to 165 and summed over the upper five layers. The contour interval is  $20 \text{ ergs cm}^{-3} \text{ s}^{-1}$ .

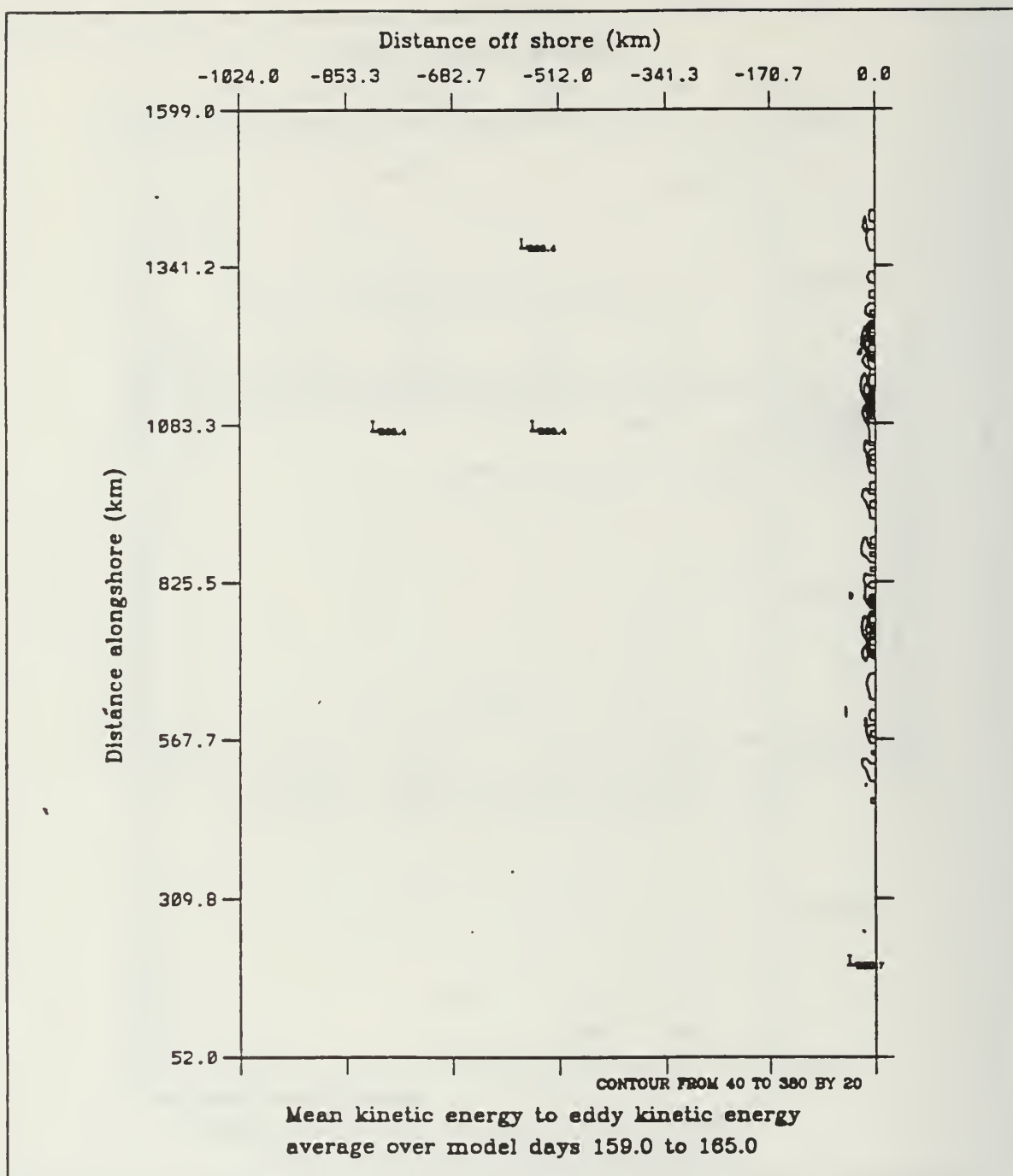


Figure 4.17b) Experiment 5: Barotropic transfer of energy (as defined in equation 3.19) from K to K' (mean to eddy kinetic energy). Transfer of energy is averaged over the days 159 to 165 and summed over the upper five layers. The contour interval is 20 ergs  $\text{cm}^{-3} \text{ s}^{-1}$ .





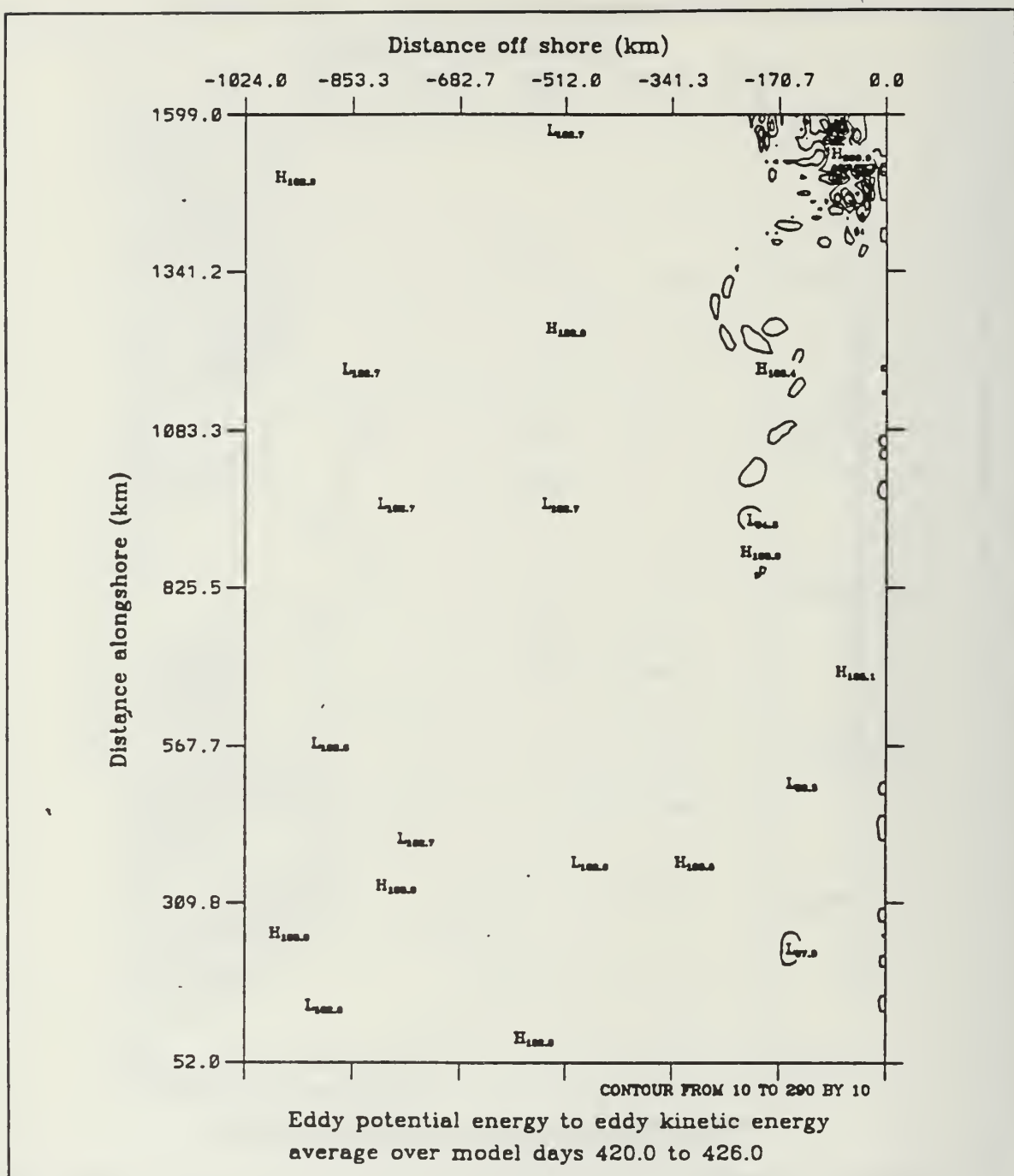


Figure 4.19a) Experiment 6: Baroclinic transfer of energy (as defined in equation 3.18) from  $P'$  to  $K'$  (eddy available to eddy kinetic energy). Transfer is averaged over days 60 to 66 and summed over the upper five layers. The contour interval is  $10 \text{ ergs cm}^{-3} \text{ s}^{-1}$ .

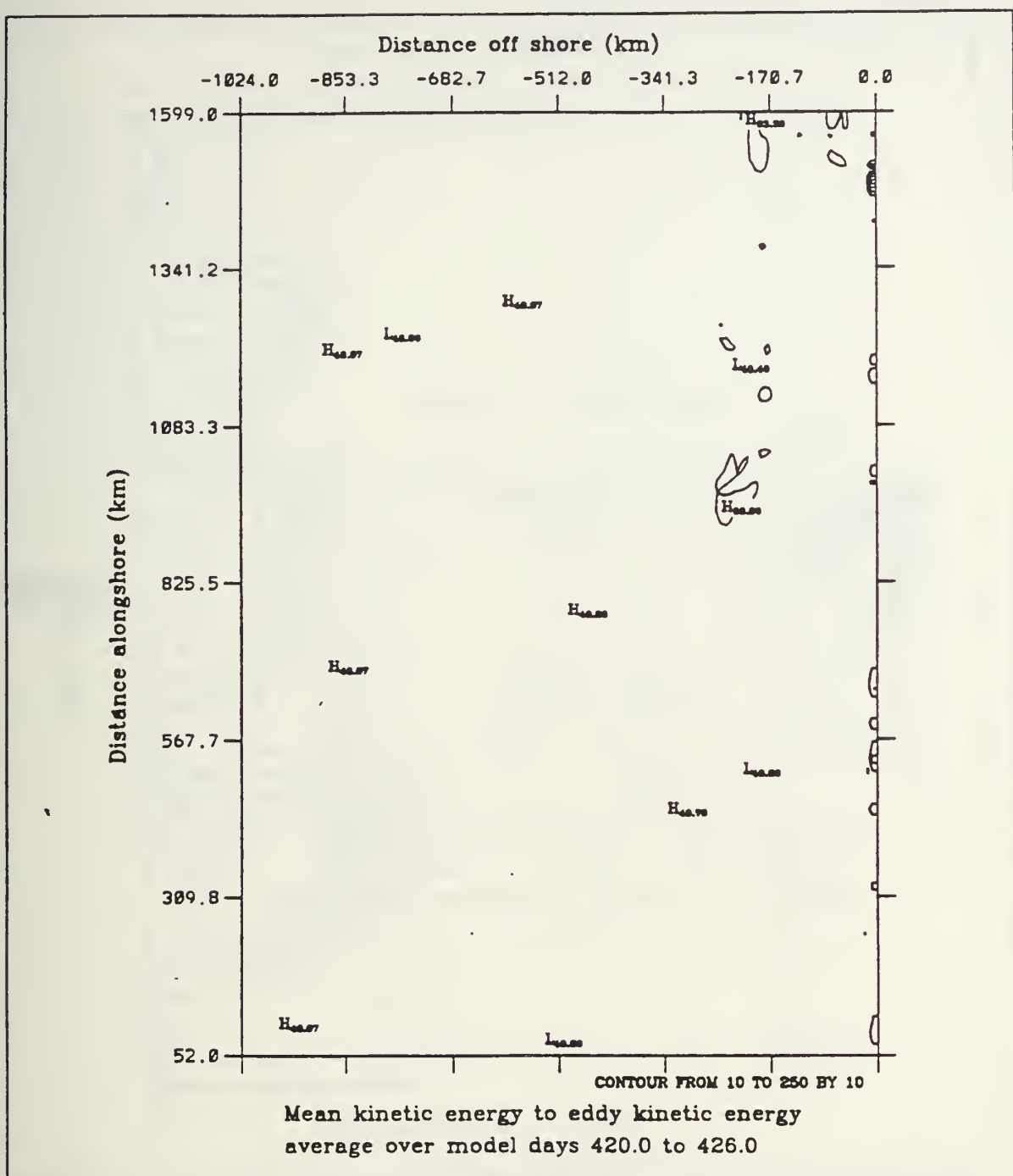


Figure 4.19b) Experiment 6: Barotropic transfer of energy (as defined in equation 3.19) from  $K$  to  $K'$  (mean to eddy kinetic energy). Transfer of energy is averaged over the days 60 to 66 and summed over the upper five layers. The contour interval is  $10 \text{ ergs cm}^{-3} \text{ s}^{-1}$ .

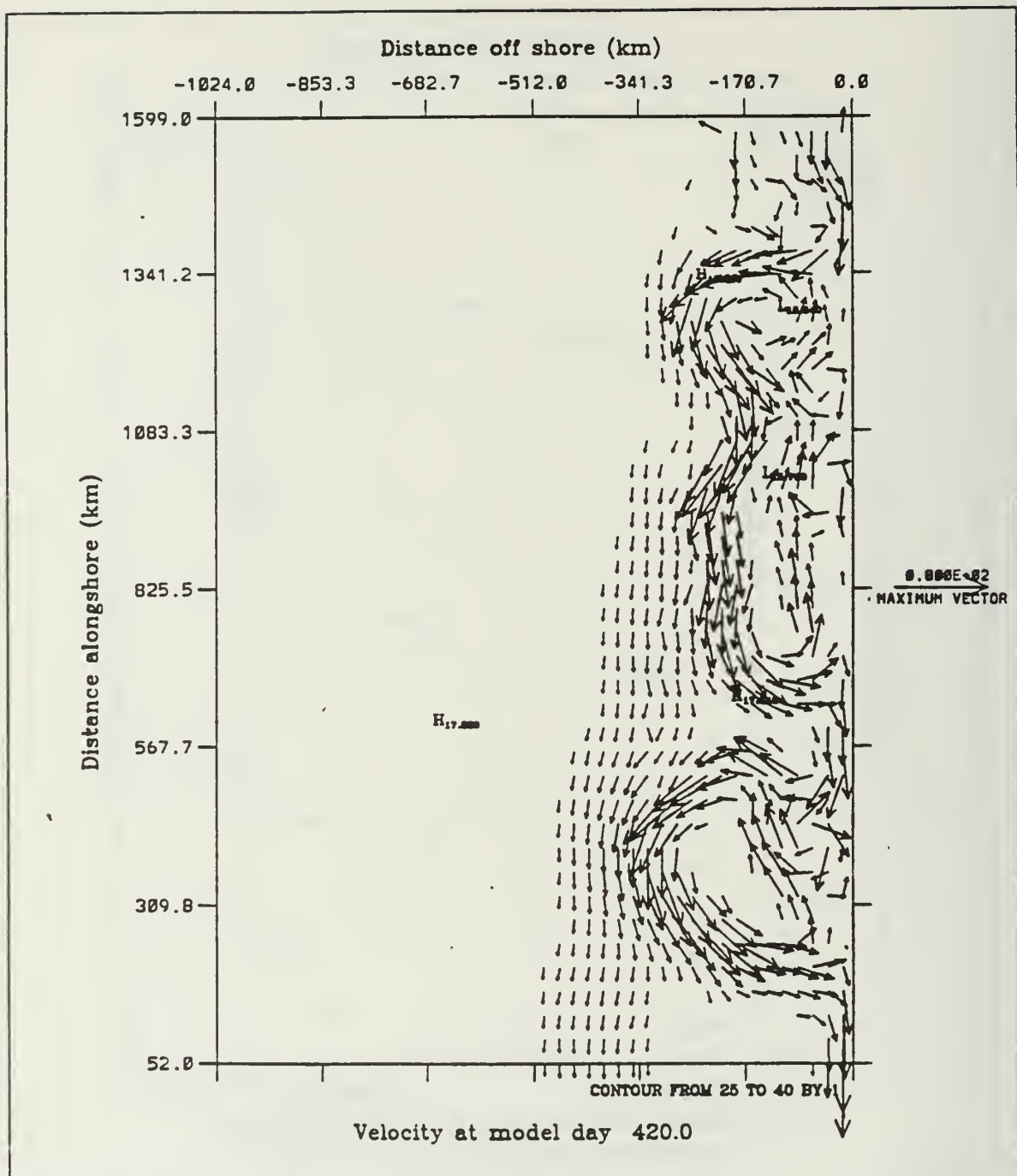


Figure 4.20 Experiment 6: Surface velocity in  $\text{cm s}^{-1}$  at day 60. As in Fig. 4.2a.

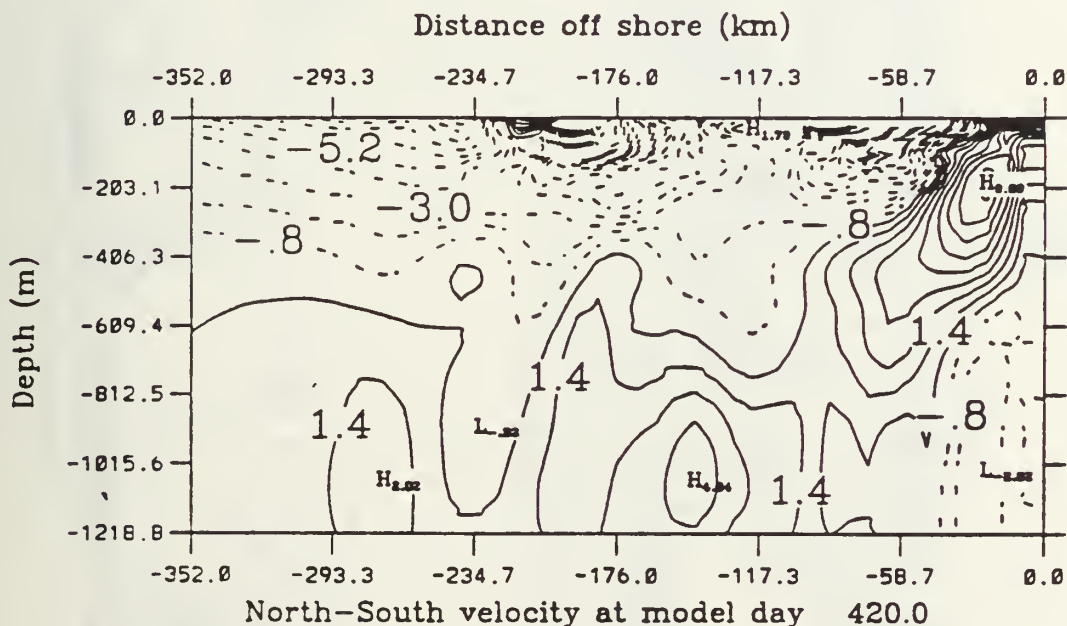


Figure 4.21 Experiment 6: Cross-section of meridional velocity contours at approximately 47°N at day 60. Dashed lines indicate southward flow and show the equatorward surface current. Solid lines indicate northward flow and indicate the poleward currents. Contour interval is 1.1 cm s<sup>-1</sup>. Maximum values shown are +/- 25 cm s<sup>-1</sup>.



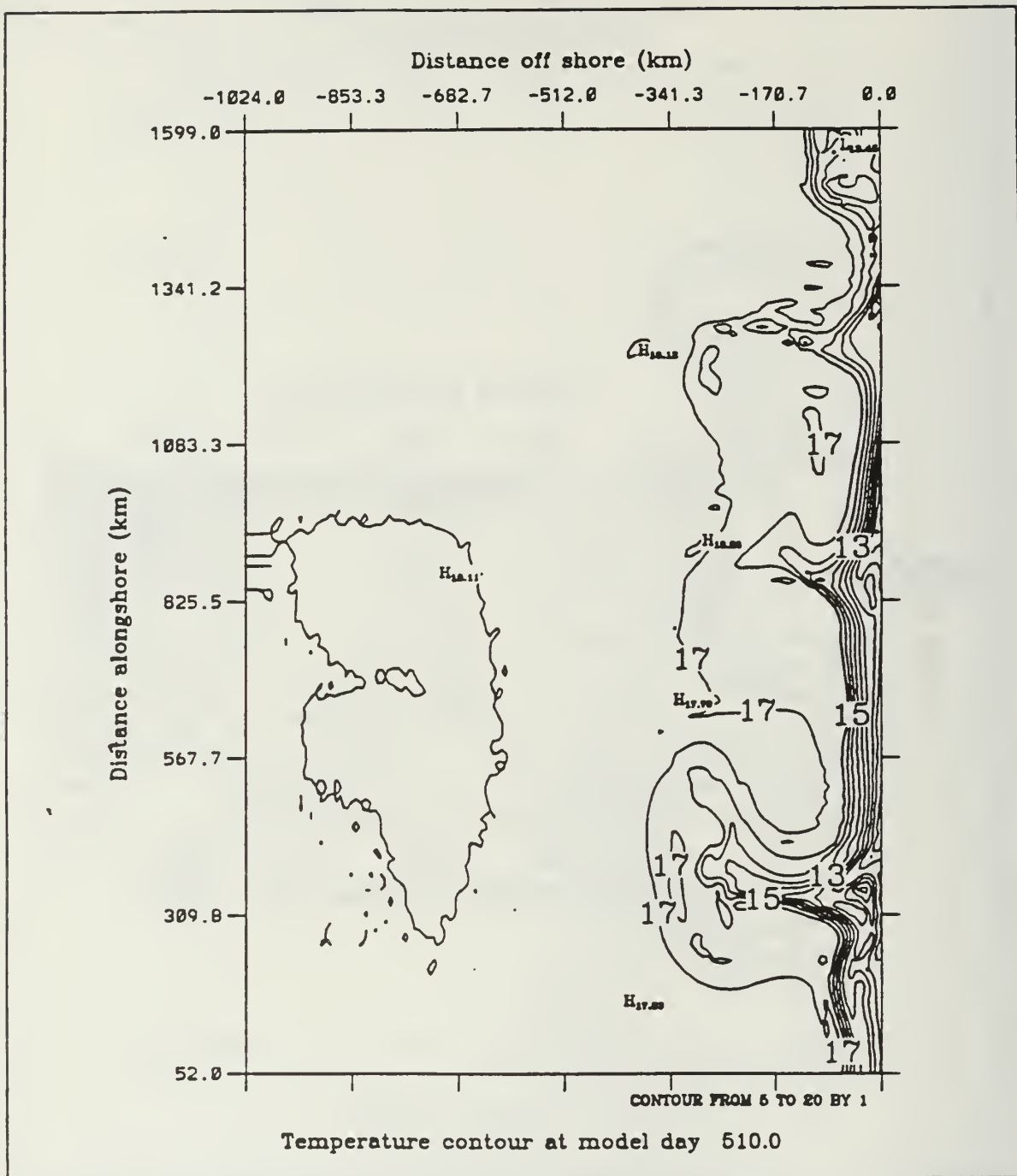


Figure 4.22a Experiment 6: Surface temperature contours at day 150. Contour interval is 1°C.

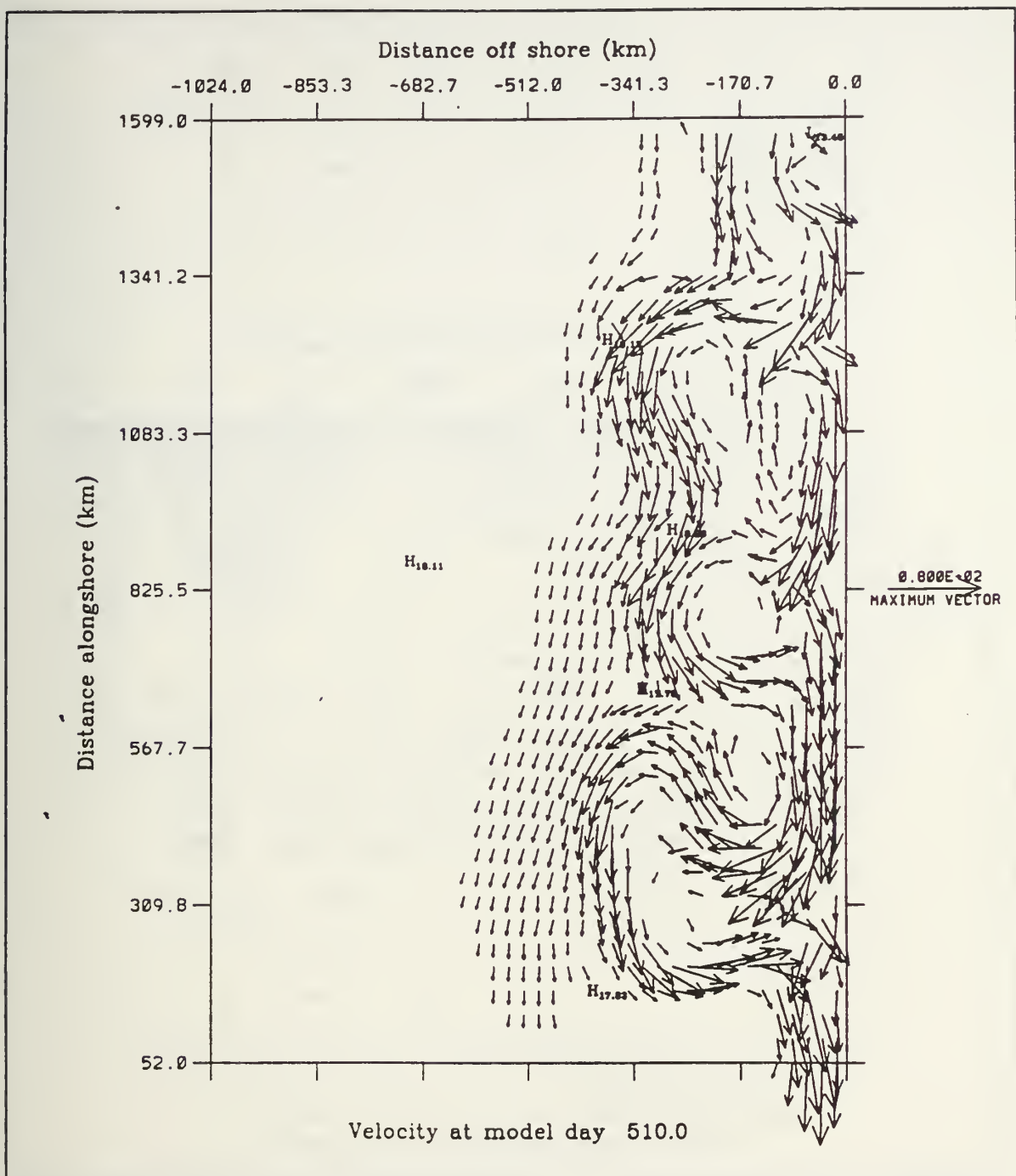


Figure 4.22b Experiment 6: Surface velocity in  $\text{cm s}^{-1}$  at day 150. As in Fig. 4.2a.

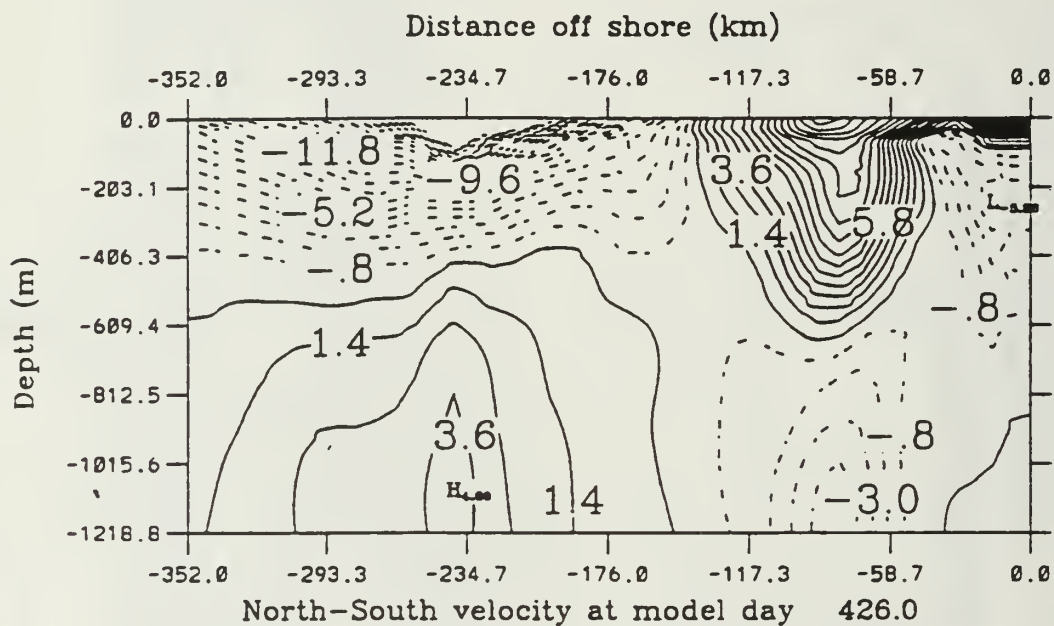


Figure 4.23 Experiment 7: Cross-section of meridional velocity contours at approximately  $45^{\circ}\text{N}$  at day 66. Dashed lines indicate southward flow and show the offshore equatorward surface current. Solid lines indicate northward flow and show the poleward currents. Contour interval is  $1.1 \text{ cm s}^{-1}$ . Maximum values shown are  $\pm 25 \text{ cm s}^{-1}$ .

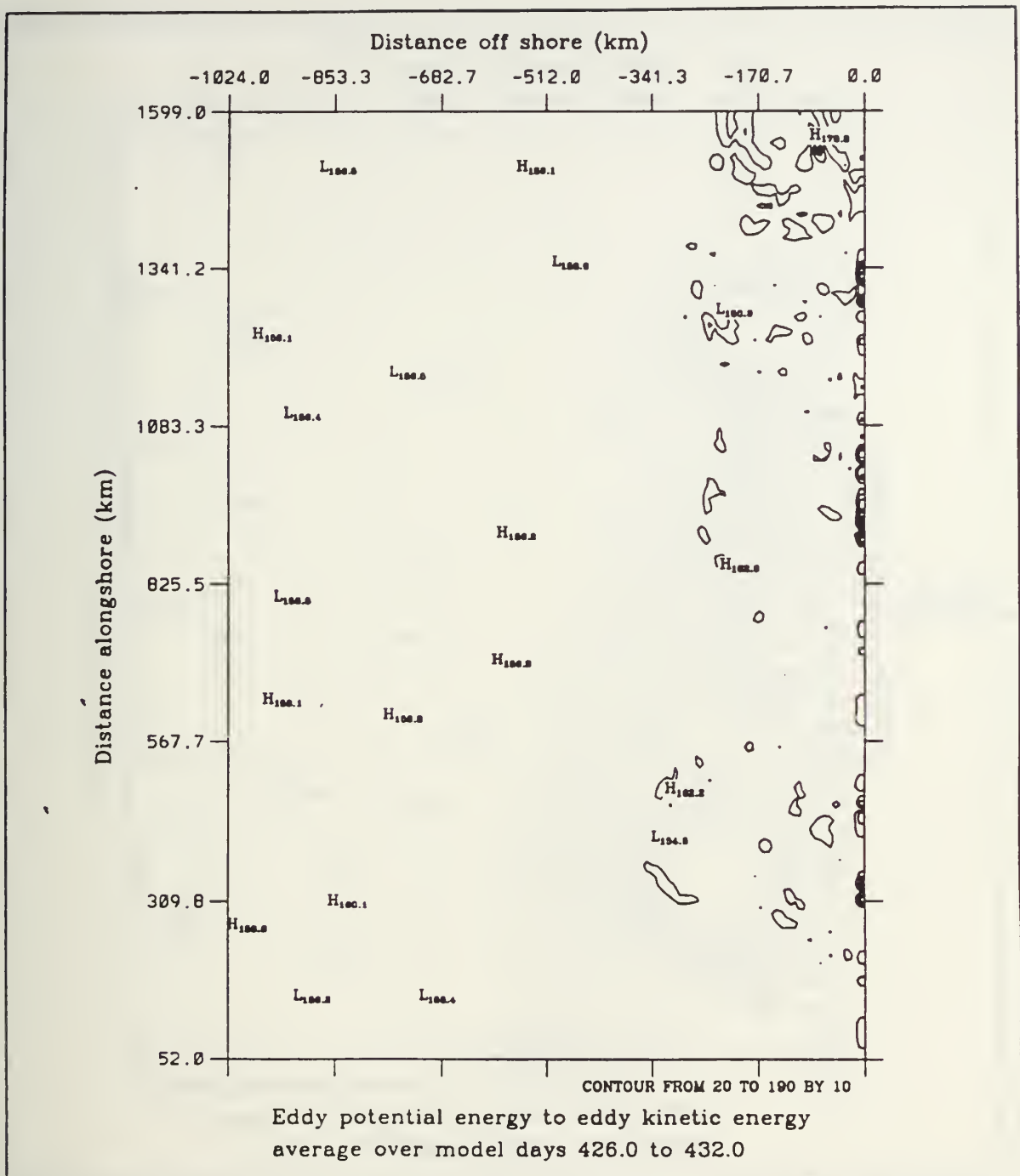


Figure 4.24a) Experiment 6: Baroclinic transfer of energy (as defined in equation 3.18) from  $P'$  to  $K'$  (eddy available to eddy kinetic energy). Transfer is averaged over days 60 to 66 and summed over the upper five layers. The contour interval is  $10 \text{ ergs cm}^{-3} \text{ s}^{-1}$ .

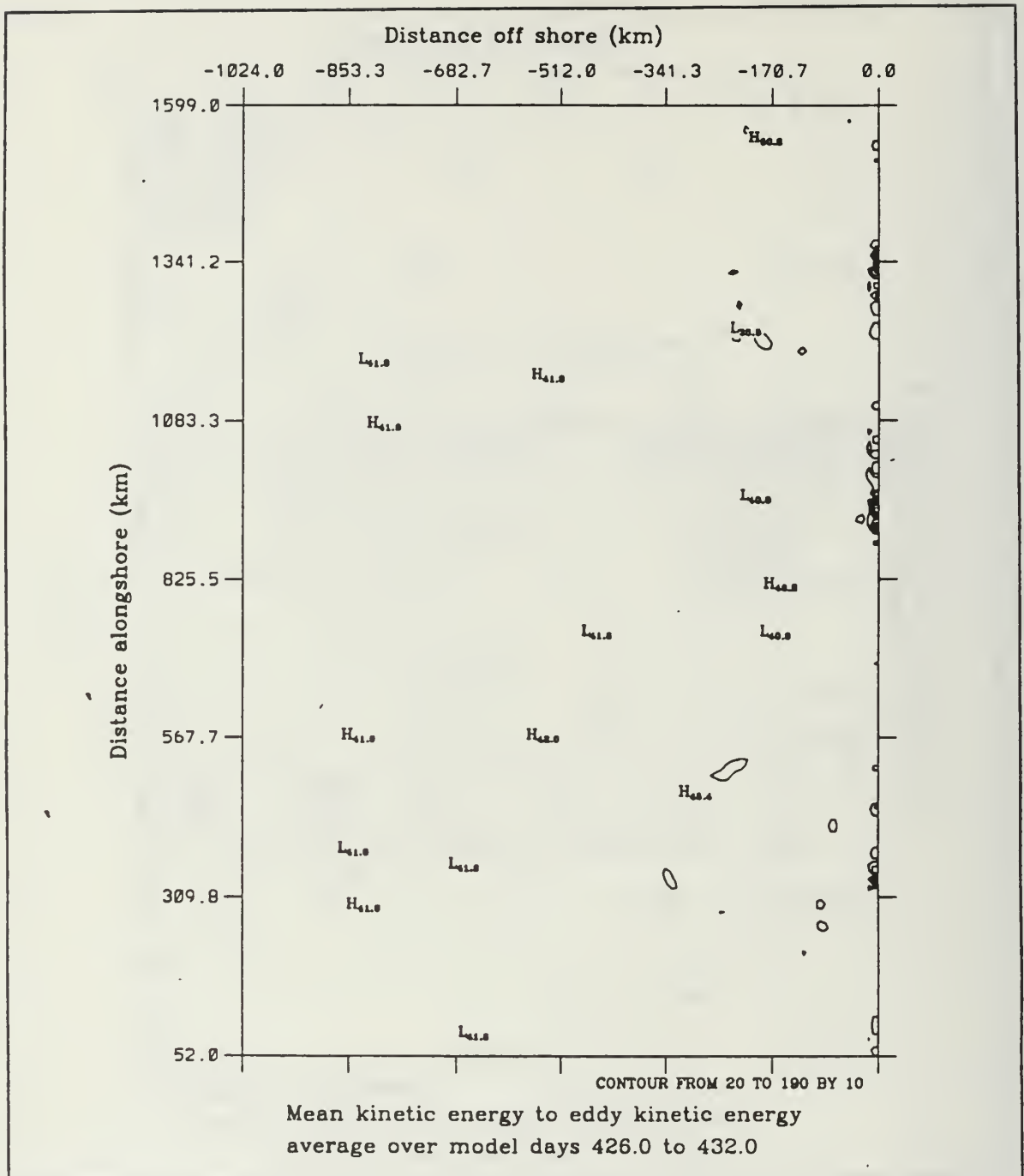


Figure 4.24b) Experiment 6: Barotropic transfer of energy (as defined in equation 3.19) from K to K' (mean to eddy kinetic energy). Transfer of energy is averaged over the days 60 to 66 and summed over the upper five layers. The contour interval is  $10 \text{ ergs cm}^{-3} \text{ s}^{-1}$ .



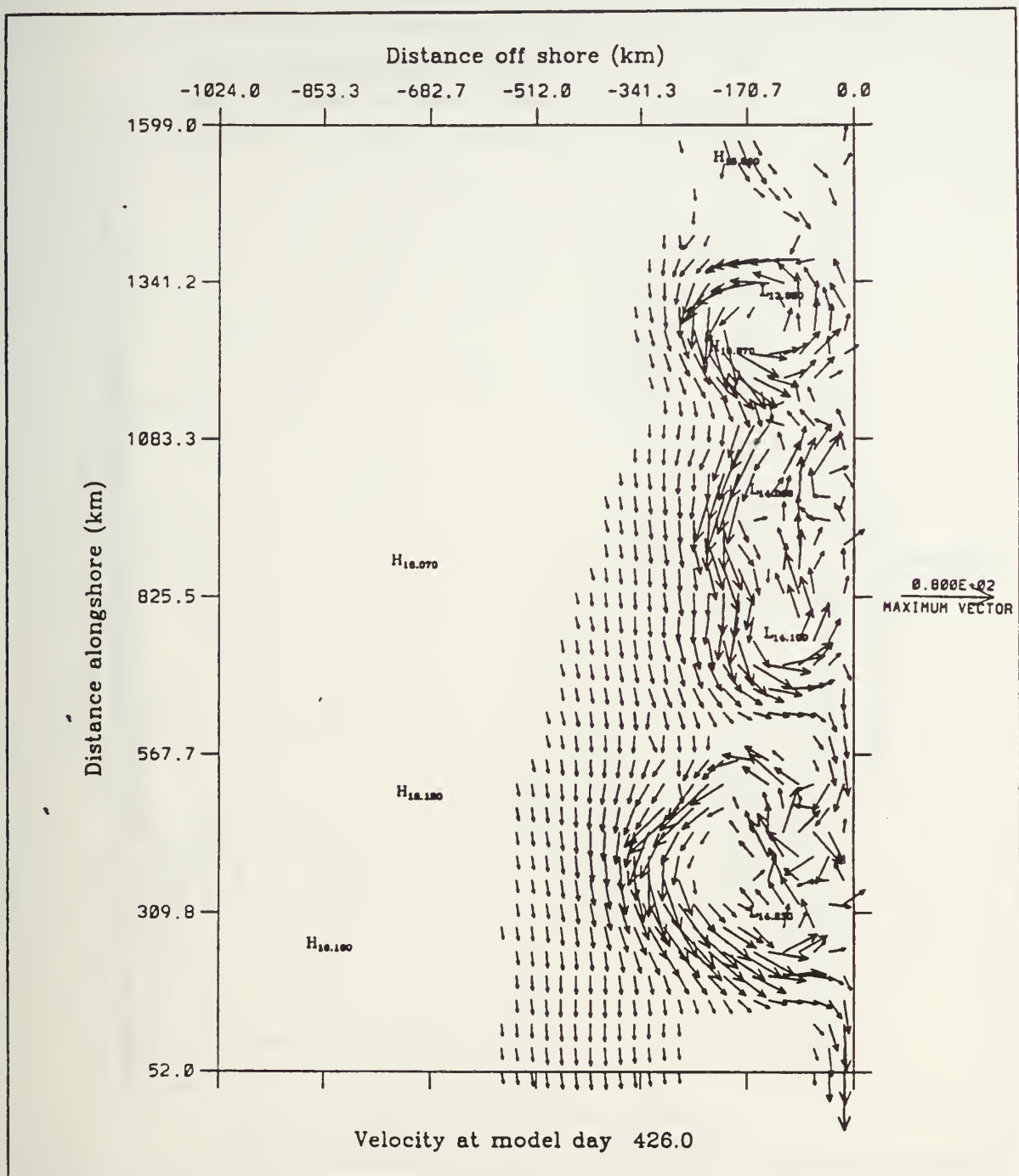


Figure 4.25 Experiment 7: Surface velocity in  $\text{cm s}^{-1}$  at day 66. As in Fig. 4.2a.

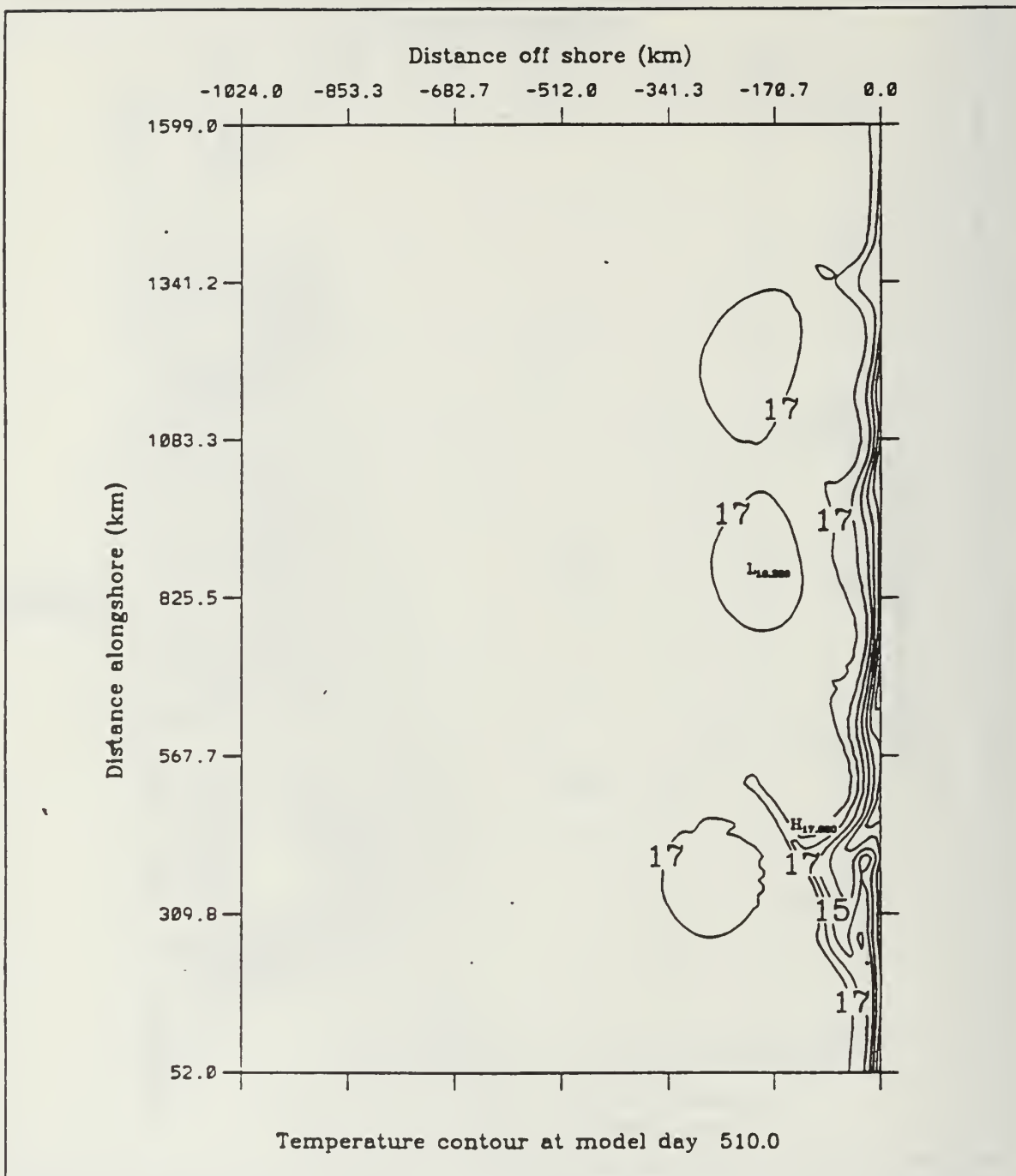


Figure 4.26a) Experiment 7: Surface temperature contours at day 150. Contour interval is  $1^{\circ}\text{C}$ .

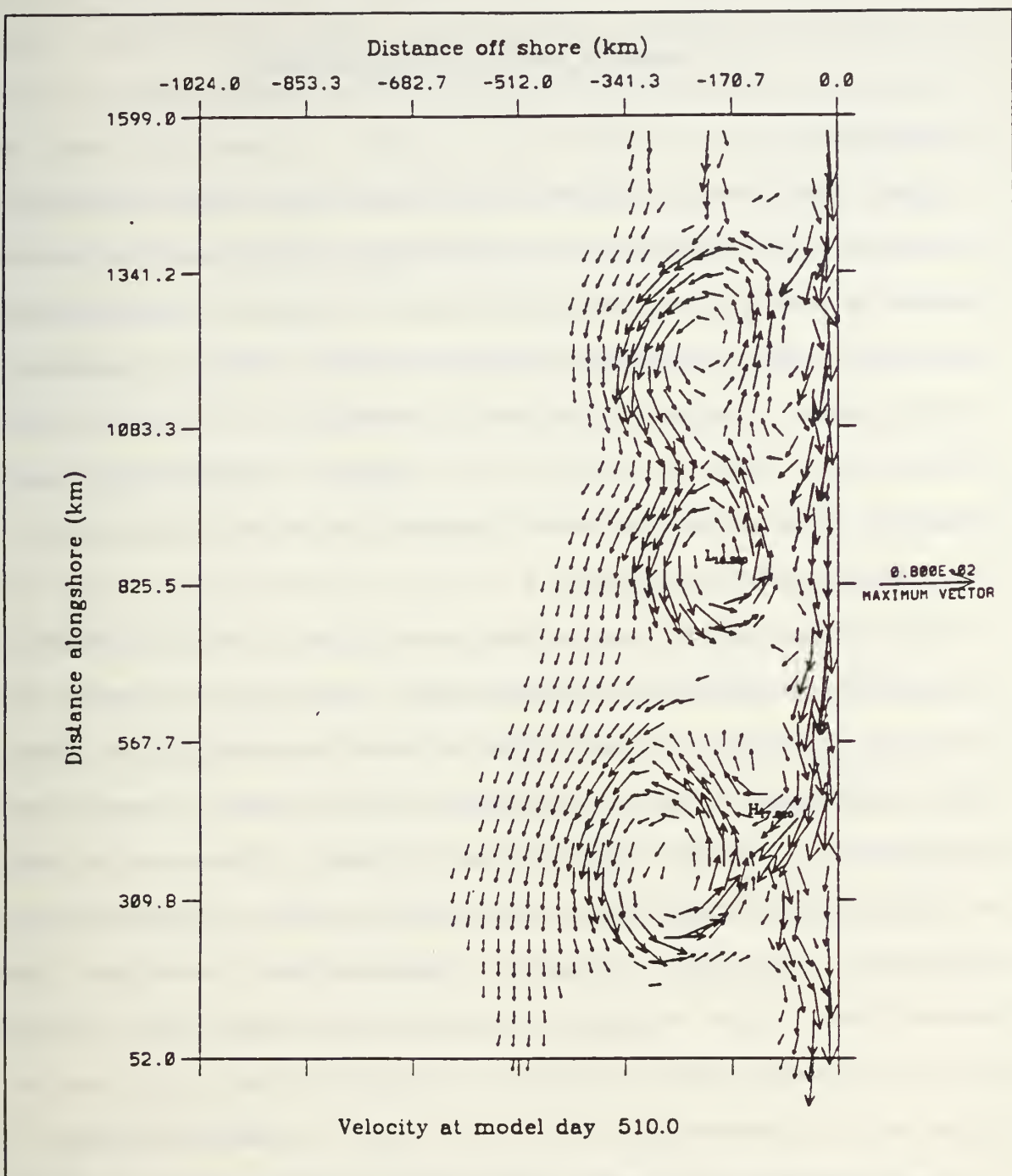


Figure 4.26b) Experiment 7: Surface velocity in  $\text{cm s}^{-1}$  at day 150. As in Fig. 4.2a.

## V. SUMMARY AND RECOMMENDATIONS

### A. SUMMARY

This study used a high-resolution primitive equation model to isolate the effects of interannual differences in wind forcing on current and eddy generation in the CCS. Wind fields were used to force an idealized, flat-bottom eastern boundary current model in seven experiments. Baroclinic and barotropic analyses were made to describe the types of instability that occurred. Model results were compared to each other and to observations of the CCS.

Five experiments were initialized from a state of rest. The results for 1980-1982 (Experiments 2 through 4) were very similar to those for a climatological average (1980-1989) wind field (Experiment 1), suggesting that these years are representative of the "mean" state of the CCS. The results for the 1983 winds (Experiment 5), however, were dramatically different, and are at least qualitatively similar to observations taken during a CCS El Niño event. This is a strong indication that anomalous atmospheric forcing plays a large role in generating an El Niño event in the CCS region.

Two experiments (6 and 7) were run with the 1980 and 1983 wind forcing applied to the velocity and temperature fields saved at day 360 from the climatological average wind forcing experiment. The results of these experiments were more similar

to observations than the experiments that were started from rest. They were the only experiments to display evidence of cold filaments extending out from the California coast during the upwelling season. The cyclonic eddies generated by the 1980 winds were larger than those in 1983, due to the longer duration of the equatorward winds in the non-El Niño year. The anomalies in 1983 were not as strong in the experiment started from existing eddy fields, apparently because the poleward winds early in the year had to work against an existing equatorward surface current.

Qualitative features of the 1982-1983 Californian El Niño were seen in experiments 5 and 7. A comparison of temperature fields during the upwelling season in 1980 (Experiment 6) and 1983 (Experiment 7) does show a positive surface temperature anomaly during the El Niño (1983) year, even though the temperature forcing used in the model is highly simplified and there is no remote temperature forcing. The current system also appeared to be weaker throughout the year in 1983 than in 1980, and there was evidence of enhanced poleward flow and onshore advection at the surface in 1983.

## **B. RECOMMENDATIONS**

Future studies should incorporate bottom topography and an irregular coastline in order to study the role of topographic steering of the currents and the possibility of preferred locations for eddy generation. A continental shelf/slope



should also result in a more realistic undercurrent. For process-oriented studies, it is easier to analyze factors such as time of initial eddy formation by starting the model from rest, but more realistic (when compared with observations) results are obtained by starting the model with an existing eddy field. Therefore, either method may be used depending on the objectives of the study.

In order to study El Niño events, a more realistic temperature forcing term should be used in the model, and remote temperature forcing and a salinity forcing term should also be considered. In order to model smaller scale and short term effects such as local wind relaxations during the upwelling season, winds that are higher in spatial and temporal resolution should be used to force the model.

The overall objective of this study is to demonstrate the hypothesis that wind variability in the coastal upwelling region is a critical element in the formation and maintenance of currents and eddies, with the specific objective of assessing the role of interannual wind forcing in the CCS by comparing model results from non-El Niño years (e.g., 1980) with those from El Niño years (e.g., 1983). Since dramatically different results were obtained by varying the wind forcing only, it may be concluded that anomalous wind forcing plays a major role in the generation of a Californian El Niño event.

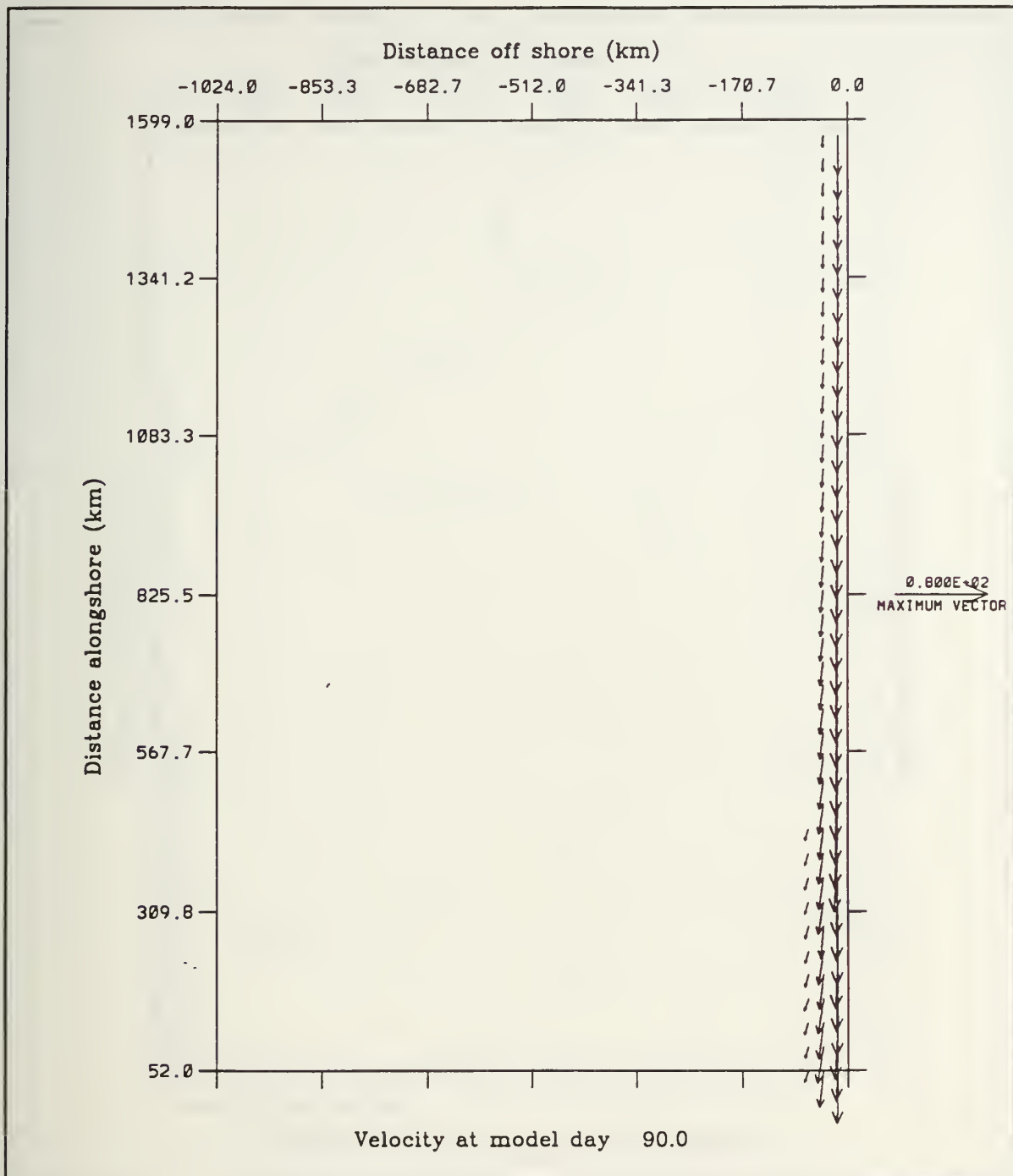


Figure A.1 Experiment 2: Surface velocity in  $\text{cm s}^{-1}$  at day 90. Values for every third gridpoint are plotted. Minimum vector plotted is  $25 \text{ cm s}^{-1}$

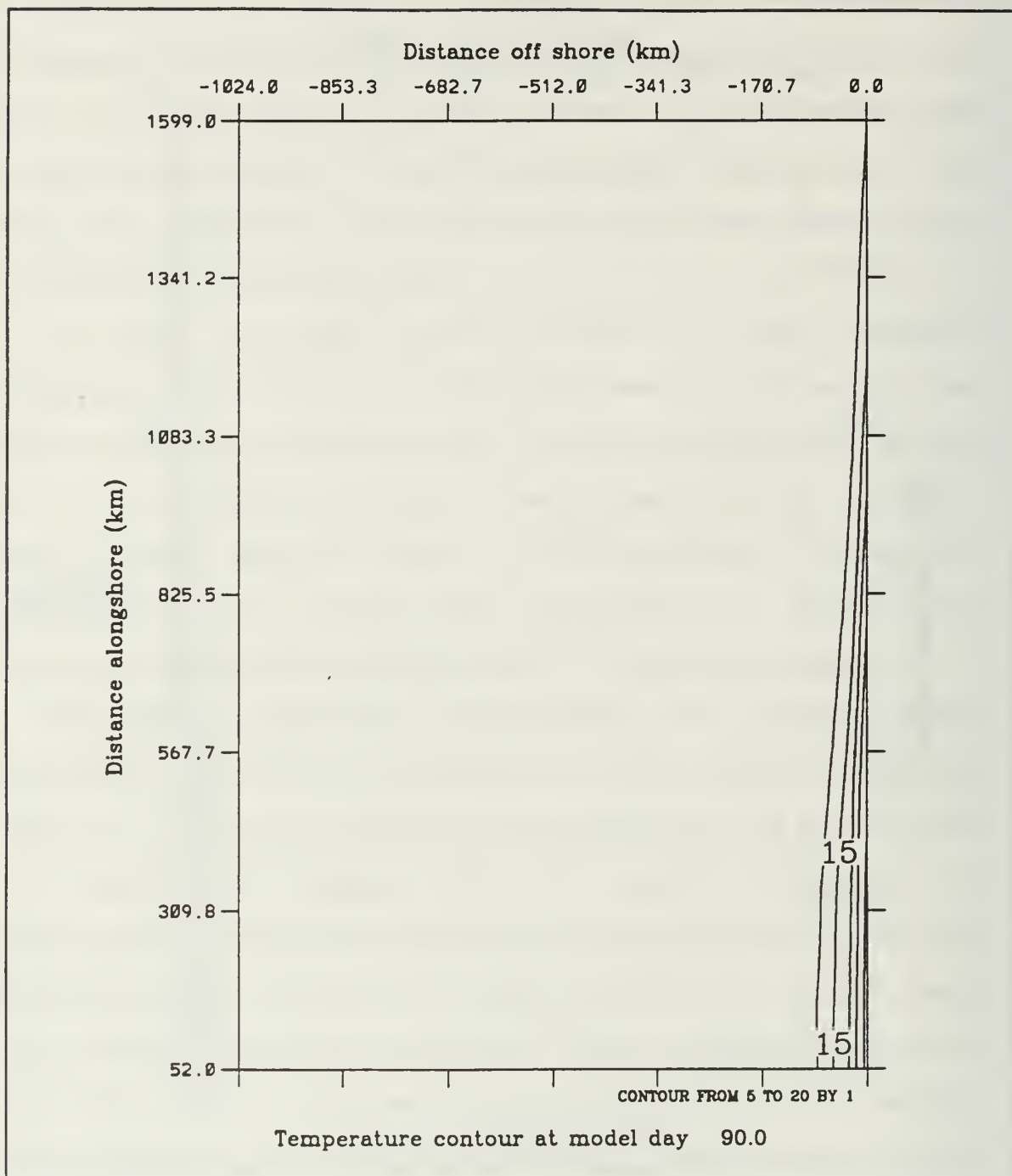


Figure A.2 Experiment 2: Surface temperature contours at day 90. The contour interval is 1°C. The temperature decreases toward the coast.

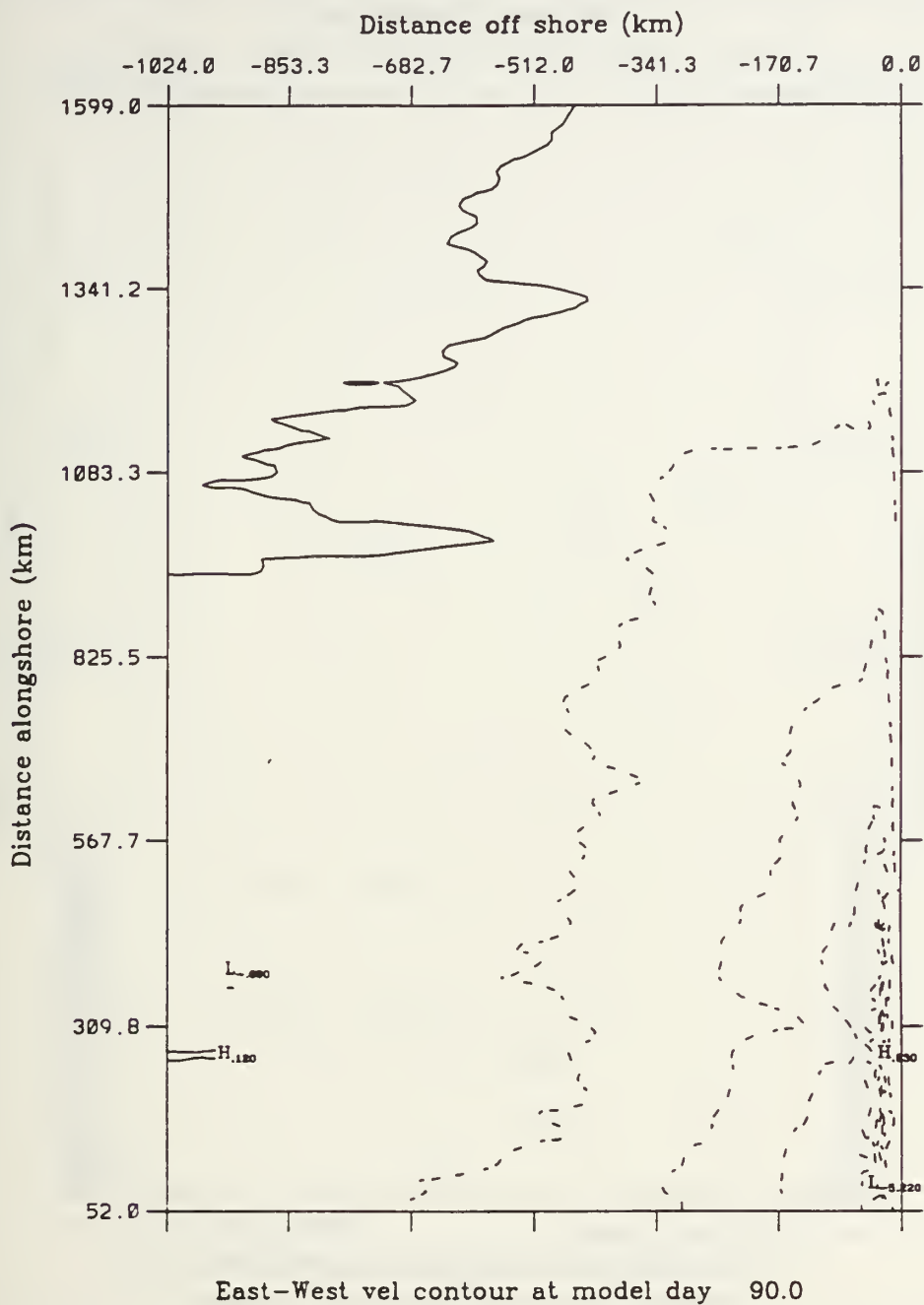


Figure A.3 Experiment 2: Surface zonal velocity contours at day 90. The contour interval is  $1 \text{ cm s}^{-1}$ . Dashed lines indicate offshore velocities.

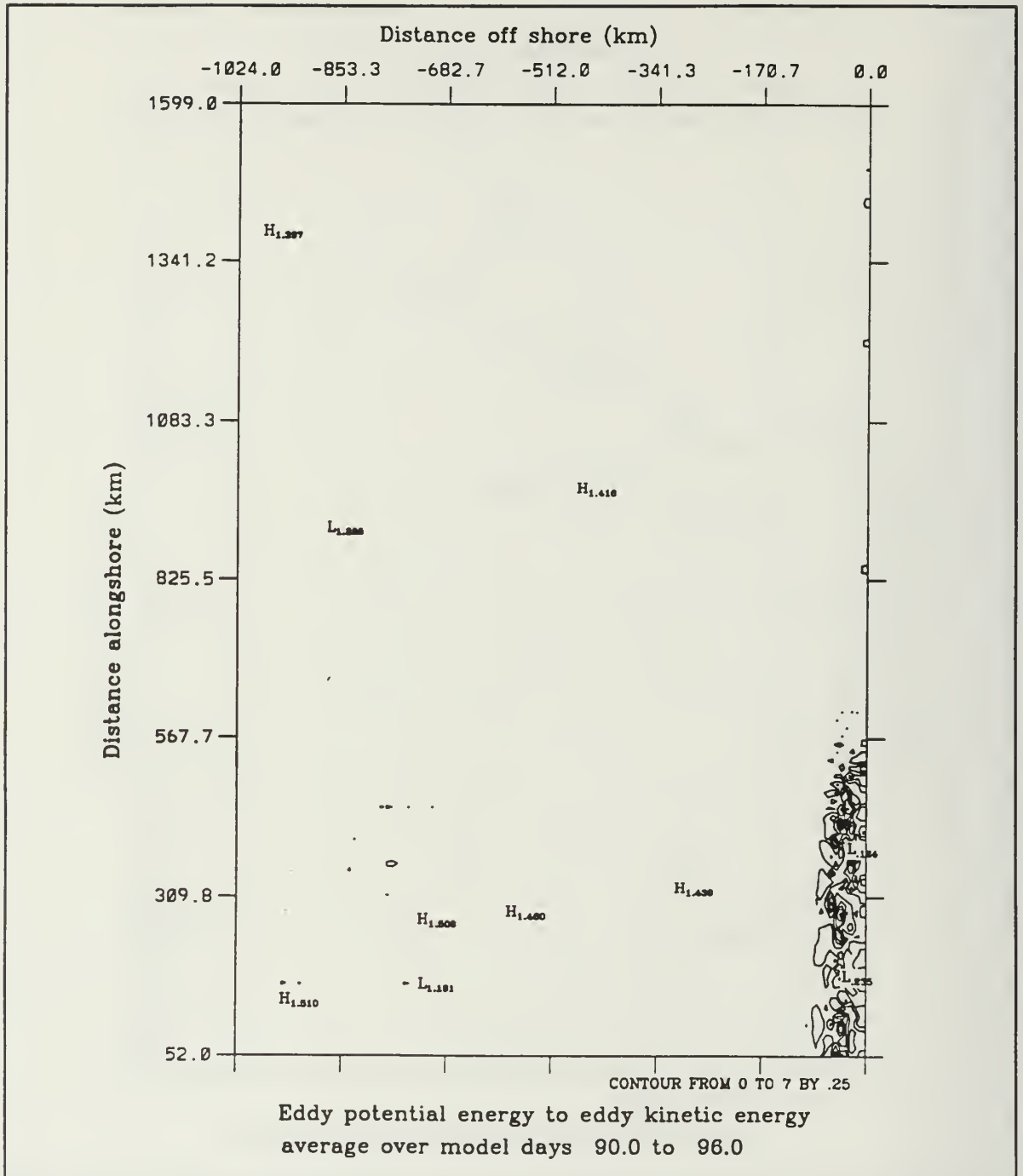


Figure A.4 Experiment 2: Baroclinic transfer of energy (as defined in equation 3.18) from P' to K' (eddy available to eddy kinetic energy). Transfer is averaged over days 90 to 96 and summed over the upper five layers. The contour interval is 0.25 ergs cm<sup>-1</sup> s<sup>-1</sup>.



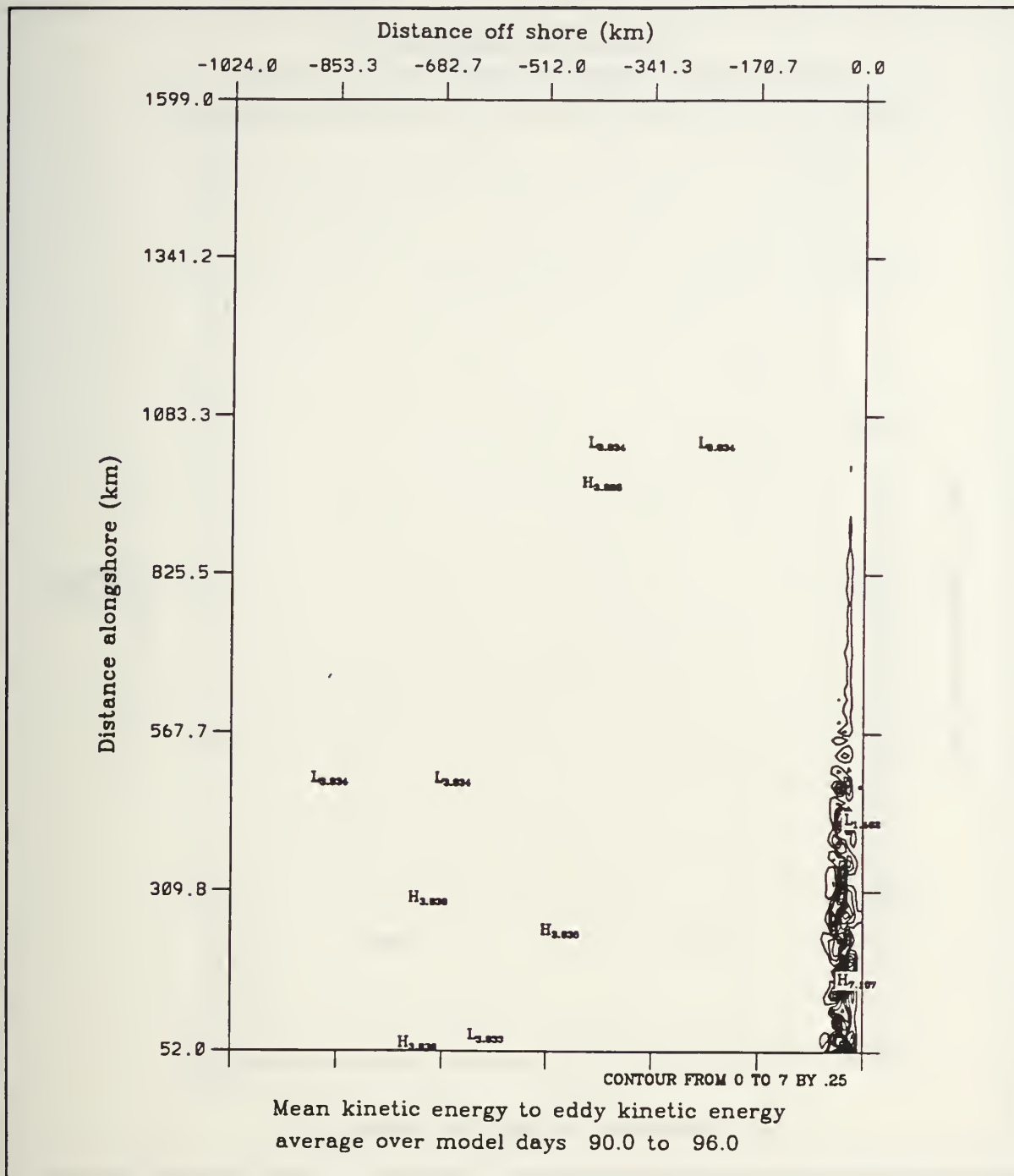


Figure A.5 Experiment 2: Barotropic transfer of energy (as defined in equation 3.19) from K to K' (mean to eddy kinetic energy). Transfer of energy is averaged over the days 90 to 96 and summed over the upper five layers. The contour interval is  $0.25 \text{ ergs cm}^{-2} \text{ s}^{-1}$ .

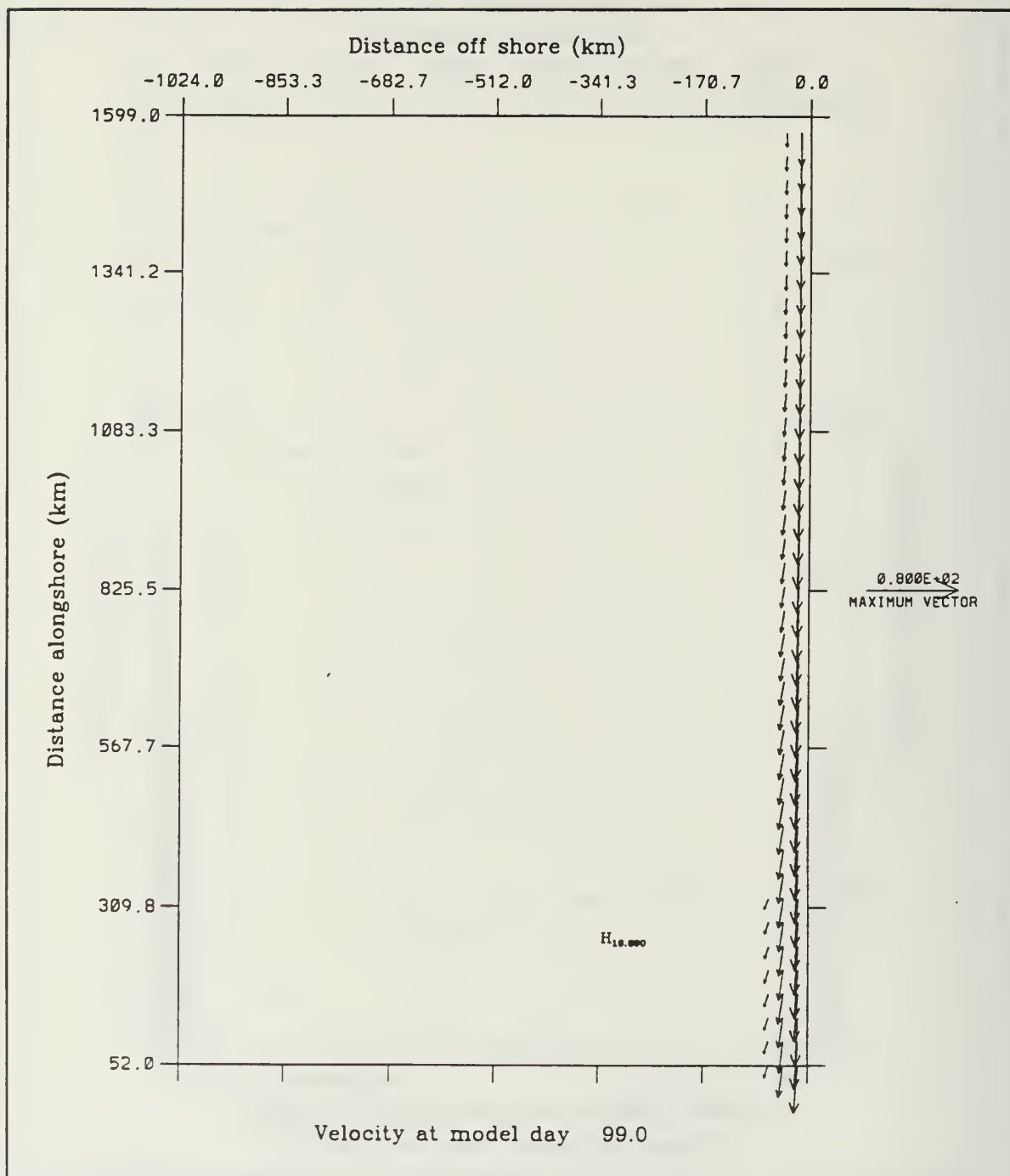


Figure A.6 Experiment 3: Surface velocity in  $\text{cm s}^{-1}$  at day 99. Values for every third gridpoint are plotted. Minimum vector plotted is  $25 \text{ cm s}^{-1}$ .

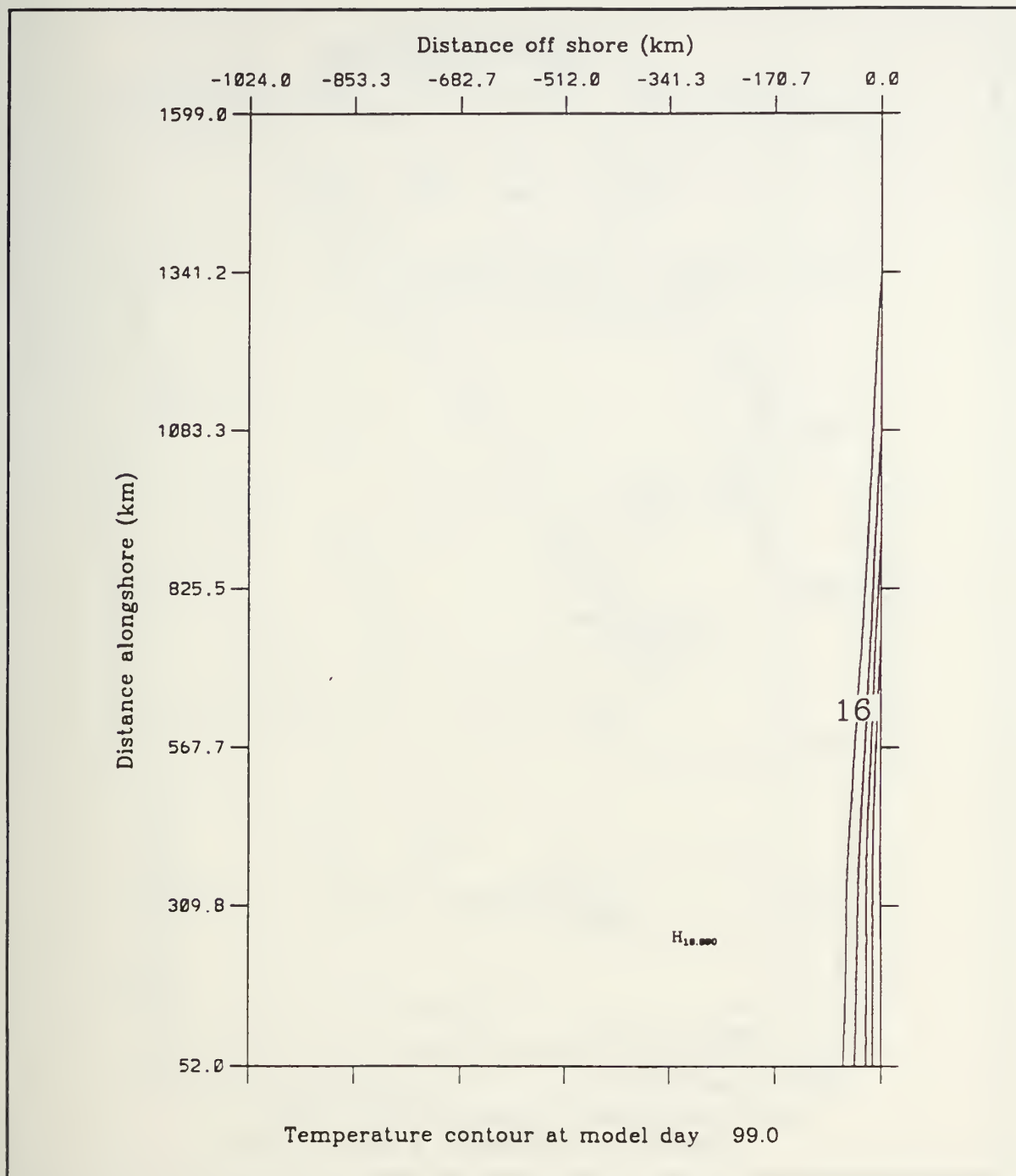


Figure A.7 Experiment 3: Surface temperature contours at day 99. The contour interval is 1°C. The temperature decreases toward the coast.

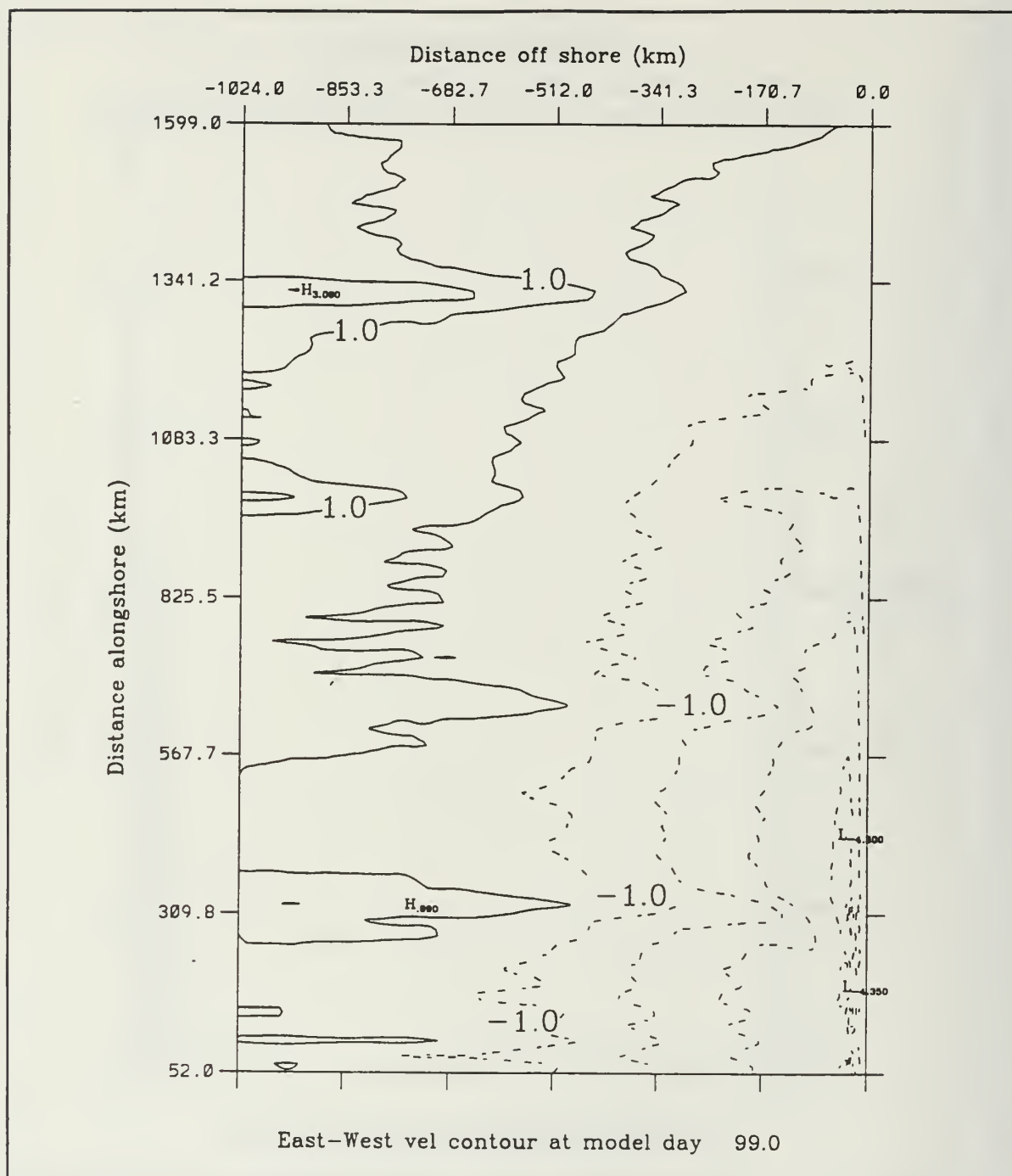


Figure A.8 Experiment 3: Surface zonal velocity contours at day 99. The contour interval is  $1 \text{ cm s}^{-1}$ . Dashed lines indicate offshore velocities.

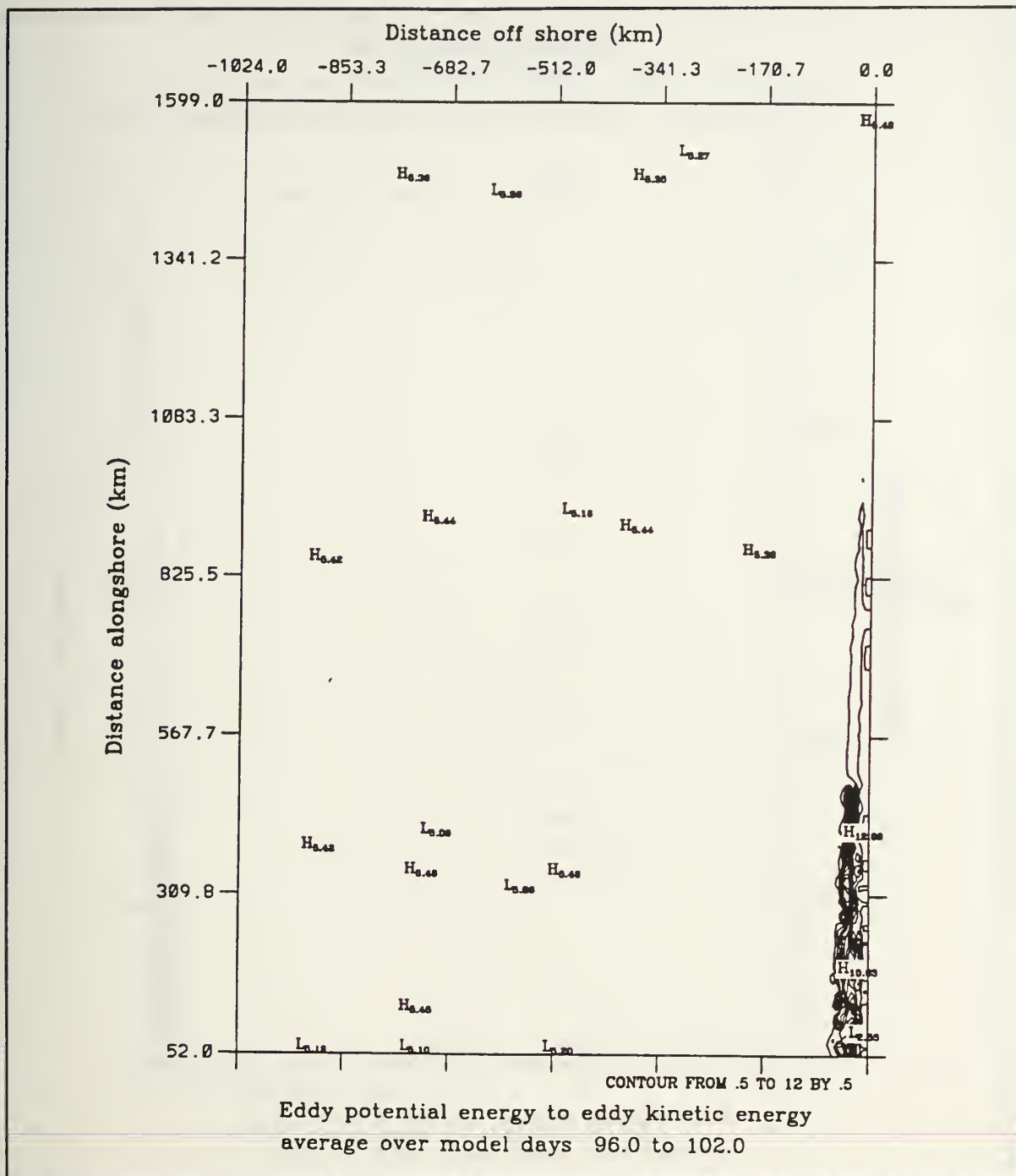


Figure A.9 Experiment 3: Baroclinic transfer of energy (as defined in equation 3.18) from  $P'$  to  $K'$  (eddy available to eddy kinetic energy). Transfer is averaged over days 96 to 102 and summed over the upper five layers. The contour interval is  $0.5 \text{ ergs cm}^{-1} \text{ s}^{-1}$ .



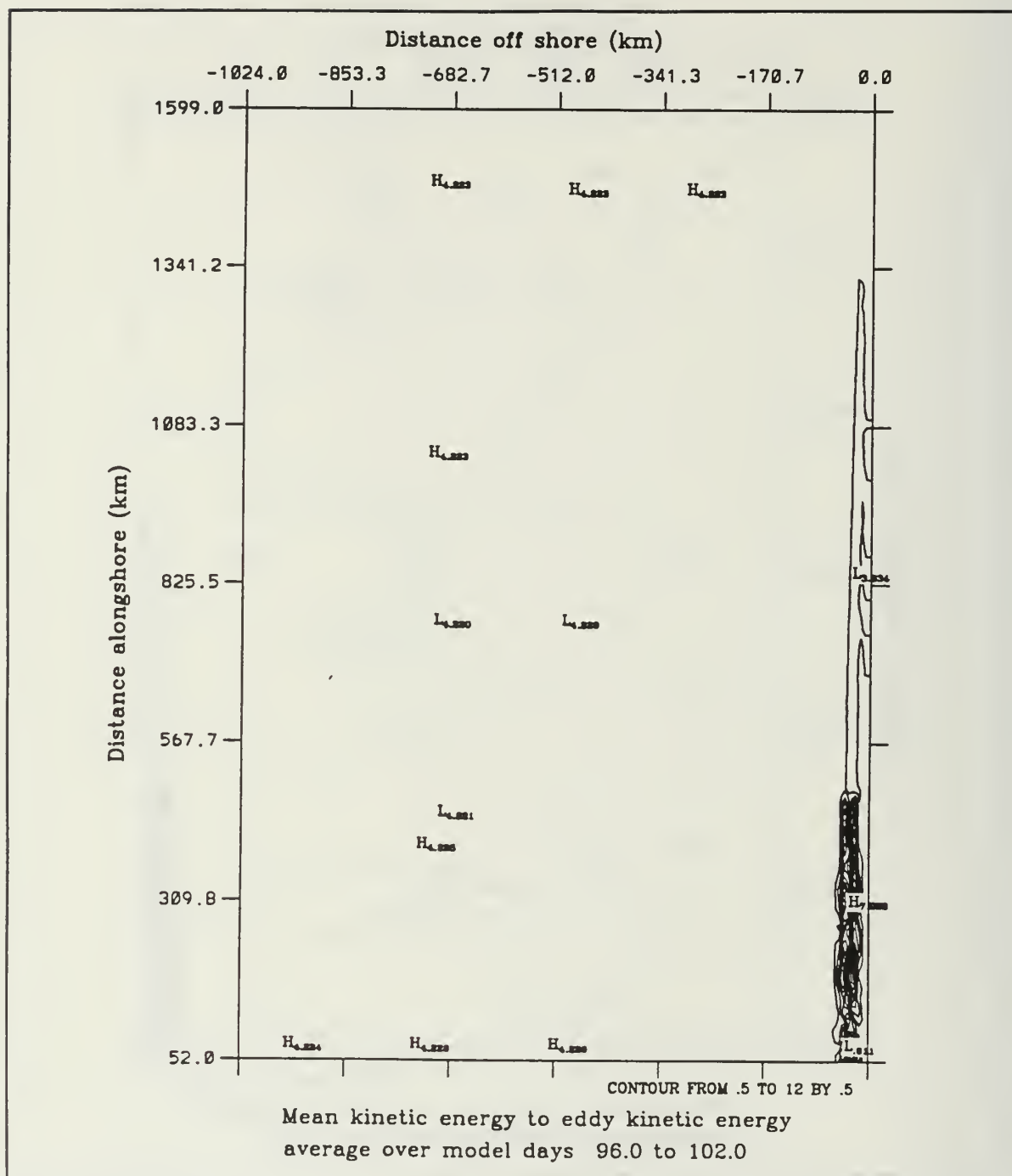


Figure A.10 Experiment 3: Barotropic transfer of energy (as defined in equation 3.19) from K to K' (mean to eddy kinetic energy). Transfer of energy is averaged over the days 96 to 102 and summed over the upper five layers. The contour interval is 0.5 ergs cm<sup>-2</sup> s<sup>-1</sup>.

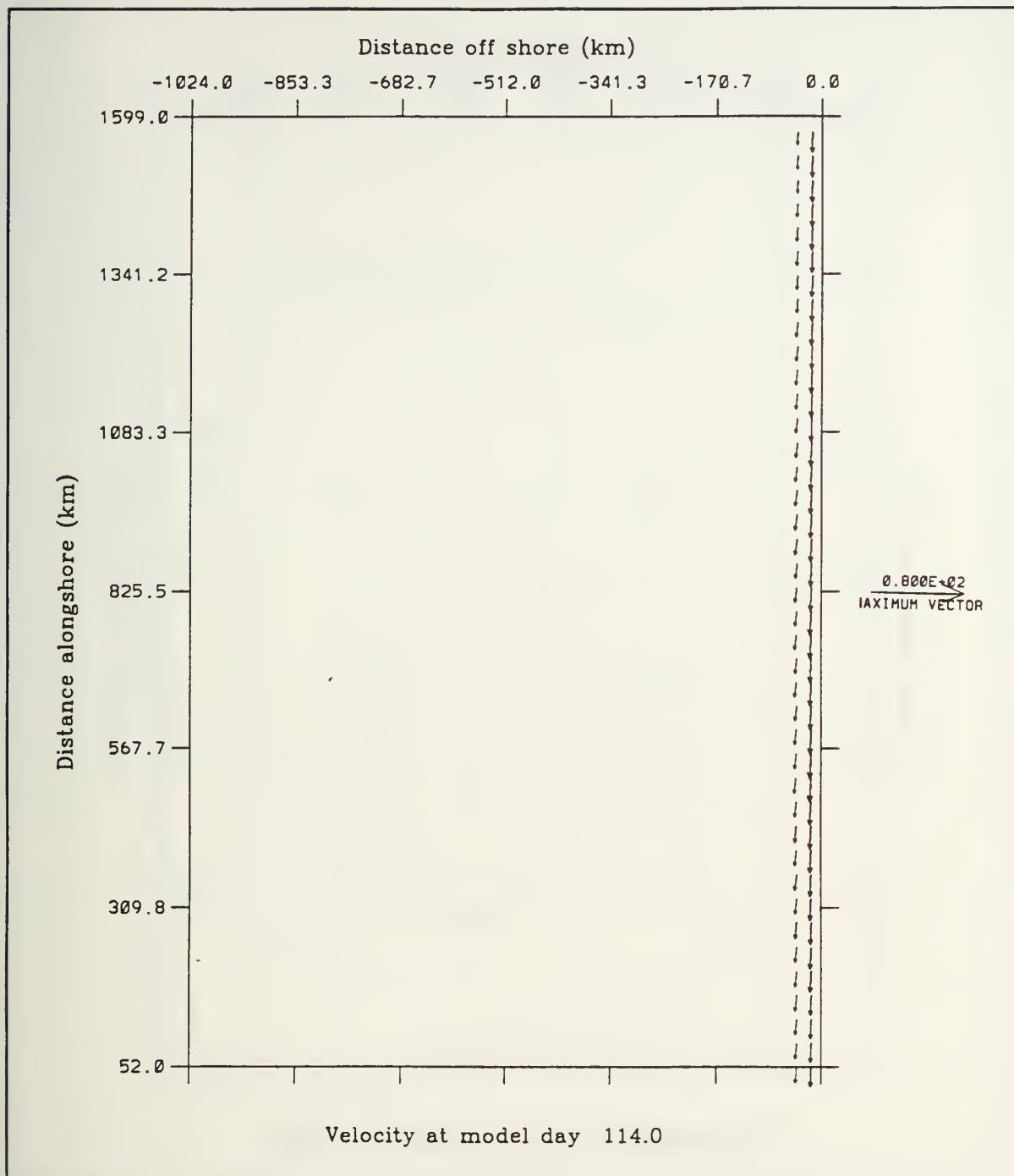


Figure A.11 Experiment 4: Surface velocity in  $\text{cm s}^{-1}$  at day 114. Values for every third gridpoint are plotted. Minimum vector plotted is  $25 \text{ cm s}^{-1}$ .

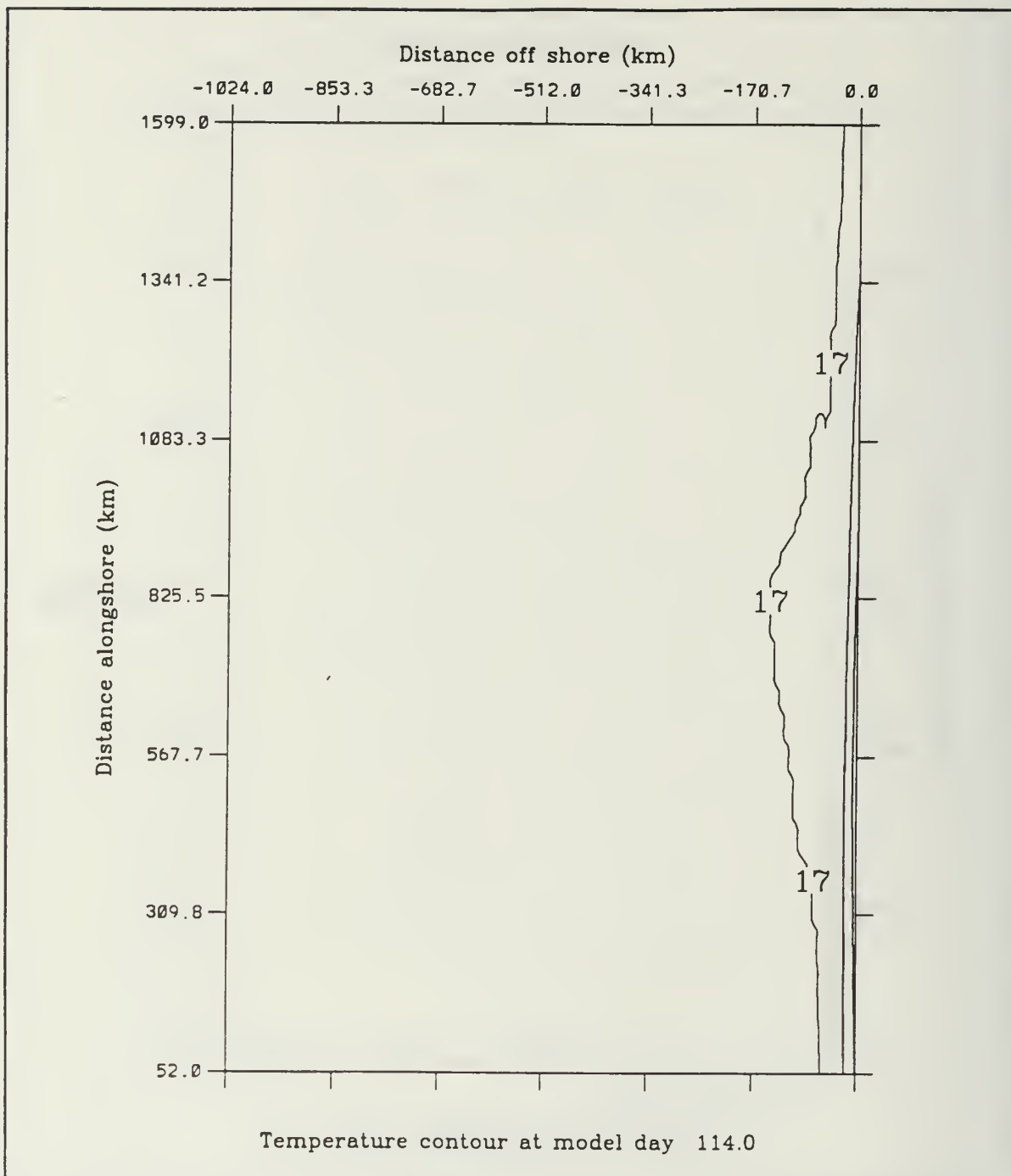


Figure A.12 Experiment 4: Surface temperature contours at day 114. The contour interval is  $1^{\circ}\text{C}$ . Temperature decreases toward the coast.

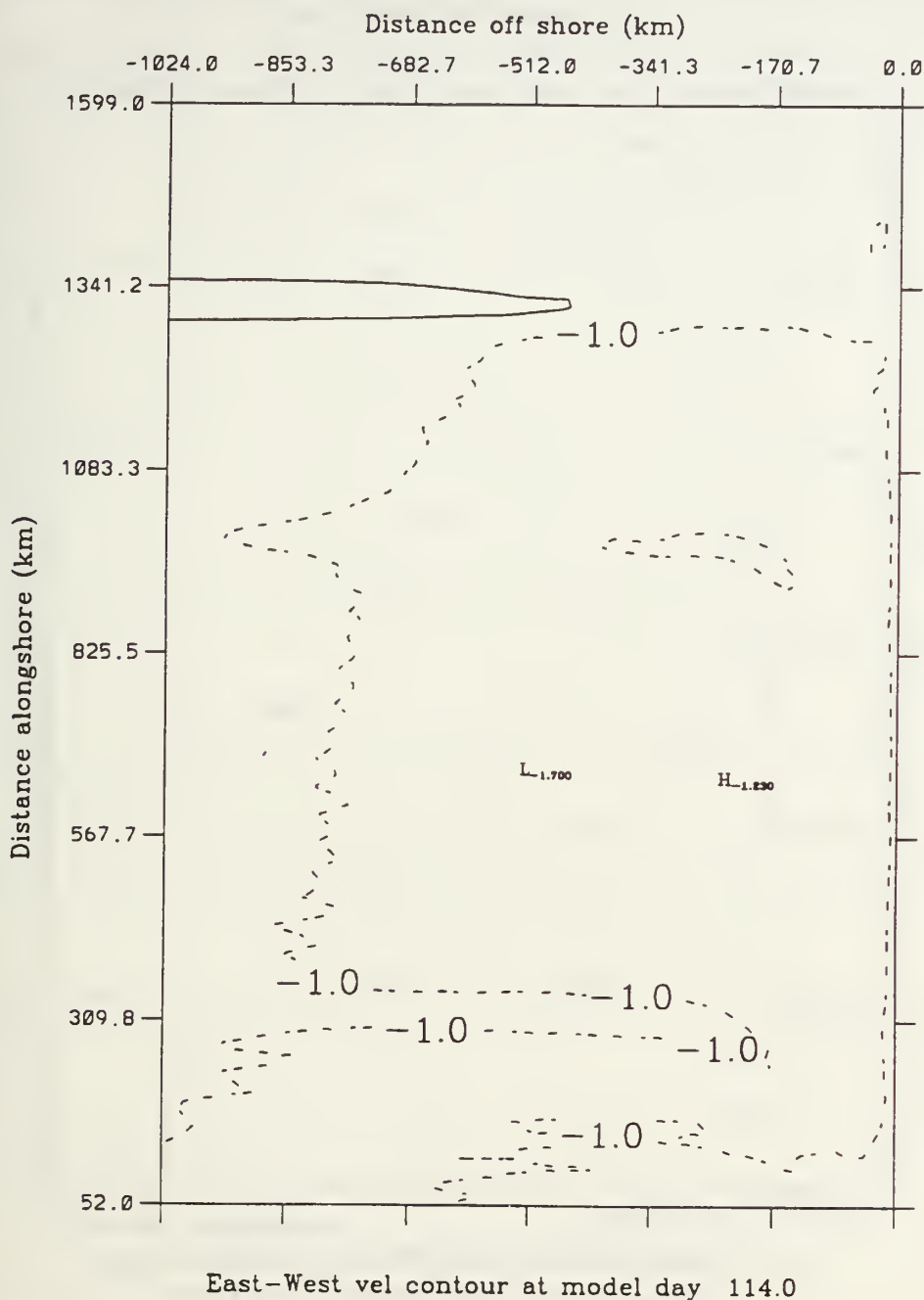


Figure A.13 Experiment 4: Surface zonal velocity contours at day 114. The contour interval is  $1 \text{ cm s}^{-1}$ . Dashed lines indicate offshore velocities.

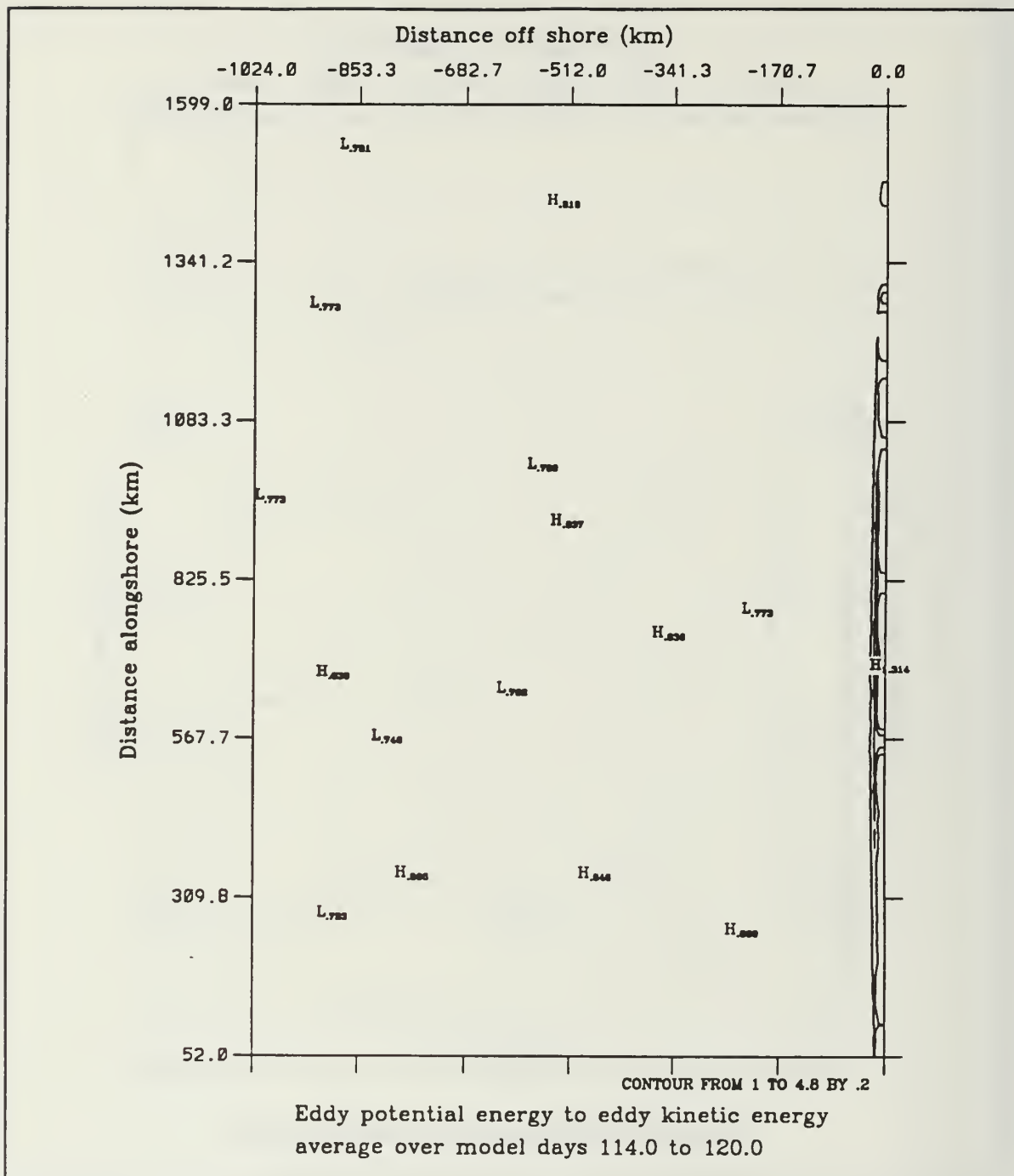


Figure A.14 Experiment 4: Baroclinic transfer of energy (as defined in equation 3.18) from P' to K' (eddy available to eddy kinetic energy). Transfer is averaged over days 114 to 120 and summed over the upper five layers. The contour interval is  $0.2 \text{ ergs cm}^{-2} \text{ s}^{-1}$ .



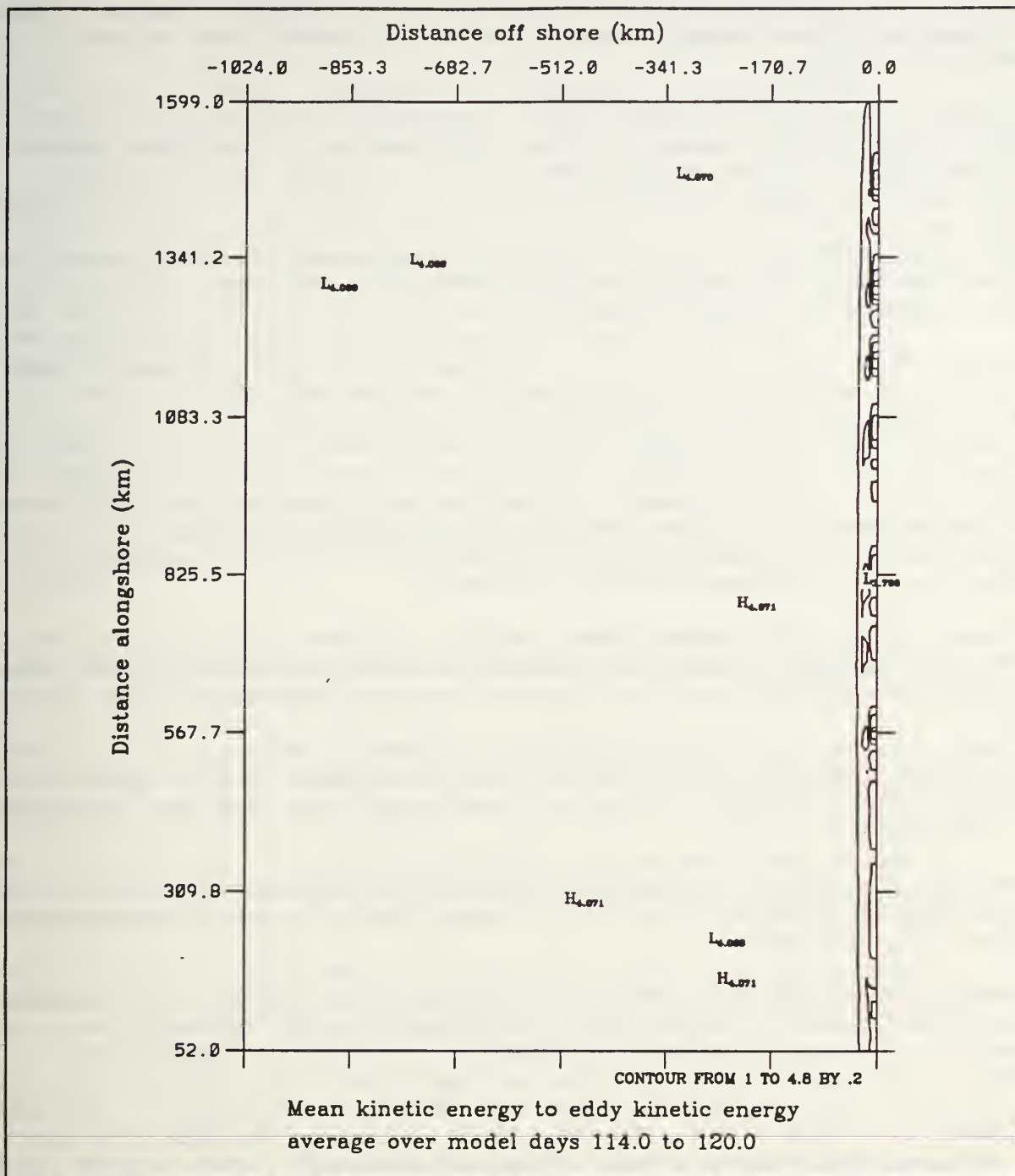


Figure A.15 Experiment 4: Barotropic transfer of energy (as defined in equation 3.19) from  $K$  to  $K'$  (mean to eddy kinetic energy). Transfer of energy is averaged over the days 114 to 120 and summed over the upper five layers. The contour interval is  $0.2 \text{ ergs cm}^{-1} \text{ s}^{-1}$ .

## LIST OF REFERENCES

- Adamec, D. R.L. Elsberry, R.W. Garwood, Jr. and R.L. Haney, 1981: An embedded mixed layer-ocean circulation model. *Dyn. Atmos. Oceans*, 5, 69-96.
- Arakawa, A. and V.R. Lamb, 1977: Computational design of the basic dynamical processes of the UCLA general circulation model. In, *Methods in Computational Physics*, J. Chang, ed., Academic Press, 17, 173-265.
- Bakun, A., and C.S. Nelson, 1991: The seasonal cycle of wind stress curl in subtropical eastern boundary current regions. *J. Phys. Oceanogr.*, 21, 1815-1834.
- Batteen, M.L., R.L. Haney, T.A. Tielking, and P.G. Renaud, 1989: A numerical study of wind forcing of eddies and jets in the California Current System. *J. Mar. Res.*, 47, 493-523.
- Batteen, M.L., 1989: Model simulations of a coastal jet and undercurrent in the presence of eddies and jets in the California Current System. In, *Poleward Flows Along Eastern Ocean Boundaries*, S.J. Neshyba, C.N.K. Mooers, R.L. Smith and R.T. Barber, eds., Springer-Verlag, 263-279.
- Batteen, M.L., M.J. Rutherford and E.J. Bayler, 1992: A numerical study of wind- and thermal-forcing effects on the ocean circulation off Western Australia. *J. Phys. Oceanogr.*, 22, 1406-1433.
- Bernstein, R.L., L.C. Breaker, and R. Whritner, 1977: California Current eddy formation: ship, air and satellite results. *Science*, 195, 353-359.
- Bjerknes, J., 1966: A possible response of the atmospheric Hadley circulation to equatorial anomalies of ocean temperature. *Tellus*, 18, 820-829.
- Blumberg, A.F. and G.L. Mellor, 1987: A description of a three-dimensional coastal ocean circulation model. In, *Three-dimensional Ocean Models*, N. Heaps, ed., American Geophysical Union, 4, 1-16.
- Breaker, L.C. and C.N.K. Mooers, 1986: Oceanic variability off the central California coast. *Prog. in Oceanogr.*, 17, 61-135.
- Brink, K.H. and T.J. Cowles, 1991: The Coastal Transition Zone Program. *J. Geophys. Res.*, 96, 14,637-14,647.
- Brink, K.H., R.C. Beardsley, P.P. Niiler, M. Abbott, A. Huyer, S. Ramp, T. Stanton, and D. Stuart, 1991: Statistical properties of near-surface flow in the California coastal transition zone, *J.*

*Geophys. Res.*, 96, 14,693-14,706.

Camerlengo, A.L. and J.J. O'Brien, 1980: Open boundary conditions in rotating fluids. *J. Comput. Physics*, 35, 12-35.

Chelton, D.B., 1984: Seasonal variability of alongshore geostrophic velocity off central California. *J. Geophys. Res.*, 89, 3473-3486.

Chelton, D.B., A.W. Bratkovich, R.L. Bernstein, and P.M. Kosro, 1988: Poleward flow off Central California during the spring and summer of 1981 and 1984. *J. Geophys. Res.*, 93, 10,604-10,620.

Davis, R.E., 1985: Drifter observations of coastal surface currents during CODE: The method and descriptive view. *J. Geophys. Res.*, 90, 4741-4755.

Edson, R.W., 1989: The effects of climatological and transient wind forcing on eddy generation in the California Current System. M.S. thesis, Naval Postgraduate School, 139 pp.

Freitag, H.P. and D. Halpern, 1981: Hydrographic observations off Northern California during May 1977. *J. Geophys. Res.*, 86, 4248-4252.

Halliwel, Jr., G.R. and J.S. Allen, 1987: The large-scale coastal wind field along the west coast of North America, 1981-1982. *J. Geophys. Res.*, 92, 1861-1884.

Halpern, D. 1976: Measurements of near-surface wind stress over an upwelling region near the Oregon coast. *J. Phys. Oceanogr.*, 6, 108-112.

Haney, R.L. 1974: A numerical study of the response of an idealized ocean to large-scale surface heat and momentum flux. *J. Phys. Oceanogr.*, 4, 145-167.

Haney, R.L., W.S. Shriver and K.H. Hunt, 1978: A dynamical-numerical study of the formation and evolution of large-scale ocean anomalies. *J. Phys. Oceanogr.*, 8, 952-969.

Haney, R.L., 1985: Midlatitude sea surface temperature anomalies: A numerical hindcast. *J. Phys. Oceanogr.*, 15, 787-799.

Hickey, B.M., 1979: The California Current System - hypothesis and facts. *Prog. in Oceanogr.*, 8, 191-279.

Holland, W.R. and M.L. Batteen, 1986: The parameterization of subgrid scale heat diffusion in eddy-resolved ocean circulation models. *J. Phys. Oceanogr.*, 16, 200-206.

- Holland, W.R., 1978: The role of mesoscale eddies in the general circulation of the ocean - numerical experiments using a wind-driven quasigeostrophic model. *J. Phys. Oceanogr.*, 8, 363-392.
- Huyer, A., 1983: Coastal upwelling in the California Current System. *Prog. in Oceanogr.*, 12, 259-284.
- Huyer, A., and P.M. Kosro, 1987: Mesoscale surveys over the shelf and slope in the upwelling region near Point Arena, California. *J. Geophys. Res.*, 89, 1655-1681.
- Huyer, A., P.M. Kosro, S.J. Lentz, and R.C. Beardsley, 1989: Poleward flow in the California Current System. In, *Poleward Flows on Eastern Boundaries*, S. Neshyba, C.N.K. Mooers, R.L. Smith and R.T. Barber, eds., Lecture Notes on Coastal and Estuarine Studies, Springer-Verlag, 142-159.
- Kosro, P.M., 1987: Structure of the coastal current field during the coastal ocean dynamics experiment. *J. Geophys. Res.*, 92, 1637-1654.
- Kosro, P.M. and A. Huyer, 1986: CTD and velocity surveys of seaward jets off Northern California, July 1981 and 1982. *J. Geophys. Res.*, 91, 7680-8690.
- Lynn, R.J. and J.J. Simpson, 1987: The California Current System: The seasonal variability of its physical characteristics. *J. Geophys. Res.*, 92, 947-966.
- Lynn, R.J., K. Bliss and L.E. Eber, 1982: Vertical and horizontal distributions of seasonal mean temperature, salinity, sigma-t, stability, dynamic height, oxygen, and oxygen saturation in the California Current, 1950-1978. *CalCOFI Atlas 30, State of Calif. Mar. Res. Comm., La Jolla*, 513 pp.
- McCreary, J.P., 1981: A linear stratified ocean model of the coastal undercurrent. *Phil. Trans. R. Soc. Lond. A*. 302, 385-413.
- McCreary, J.P., P.K. Kundu and S.-Y. Chao, 1987: On the dynamics of the California Current System. *J. Mar. Res.*, 45, 1-32.
- Mitchell, R.P., 1993: A numerical study of seasonal wind forcing effects on the California Current System. M.S. Thesis, Naval Postgraduate School, 113 pp.
- Mooers, C.N.K. and A.R. Robinson, 1984: Turbulent jets and eddies in the California Current and inferred cross-shore transports. *Science*, 223, 51-53.
- Nelson, C.S., 1977: Wind stress and wind stress curl over the California Current. *NOAA Tech. Rep. NMFS SSFR-714*, U.S. Dept. Commerce, 155 pp.



- Nelson, C.S. and D.M. Husby, 1983: Climatology of surface heat fluxes over the California Current Region. *NOAA Tech. Rep. NMFS SSRF-714*, U.S. Dept. Commerce, 155 pp.
- Pares-Sierra, A. and O'Brien, J.J., 1989: The seasonal and interannual variability of the California Current System: A numerical model. *J. Geophys. Res.*, 94, 3159-3180.
- Paulson, C.A. and J.J. Simpson, 1977: Irradiance measurements in the upper ocean. *J. Phys. Oceanogr.*, 7, 952-956.
- Philander, S.G.H., 1990: The Southern Oscillation: variability of the tropical atmosphere. In, *El Niño, La Niña, and the Southern Oscillation*. Academic Press, Inc., 9-57.
- Philander, S.G.H. and J.-H. Yoon, 1982: Eastern boundary currents and coastal upwelling. *J. Phys. Oceanogr.*, 12, 862-879.
- Reed, R.K. and D. Halpern, 1976: Observations of the California Undercurrent off Washington and Vancouver Island. *Limnol. Oceanogr.*, 21, 389-398.
- Reid, J.L. 1962: Measurements of the California Countercurrent at a depth of 250 meters. *J. Mar. Res.*, 20, 134-137.
- Reid, J.L., 1988: Physical oceanography, 1947-1987. *Calif. Coop. Oceanic Fish. Invest. Rep.*, 29, 42-65.
- Reinecker, M.M. and C.N.K. Mooers, 1984: The 1982-1983 El Niño signal off northern California. *J. Geophys. Res.*, 91, 6597-6608.
- Semtner, A.J. and Y. Mintz, 1977: Numerical simulation of the Gulf Stream and midocean eddies. *J. Phys. Oceanogr.*, 1, 208-230.
- Simpson, J.J., 1983: Large-Scale thermal anomalies in the California Current during the 1982-1983 El Niño. *Geophys. Res. Letters*, 10, 937-940.
- Simpson, J.J., 1984: El Niño-induced onshore transport in the California Current during 1982-1983. *Geophys. Res. Letters*, 11, 241-242.
- Smith, R.L. 1968: Upwelling. *Oceanography and Marine biology reviews*, 6, 11-46.
- Strub, P.T., J.S. Allen, A. Huyer, and R.L. Smith, 1987: Large-scale structure of the spring transition in the coastal ocean off western North America. *J. Geophys. Res.*, 92, 1527-1544.
- Trenberth, K.E., J.G. Olson and, and W.G. Large, 1989: A global ocean wind stress climatology based on ECMWF analyses. *NCAR Tech. Note NCAR/TN-338+STR*, 93 pp.



Trenberth, K.E., W.G. Large, and J.G. Olson, 1990: The mean annual cycle in global ocean wind stress, *J. Phys. Oceanogr.*, 20, 1742-1760.

Weatherly, G.L., 1972: A study of the bottom boundary layer of the Florida Current. *J. Phys. Oceanogr.*, 2, 54-72.

Wickham, J.B., A.A. Bird, and C.N.K. Mooers, 1987: Mean and variable flow over the central California continental margin, 1978-1980. *Cont. Shelf Res.*, 7, 827-849.

# INITIAL DISTRIBUTION LIST

	No. Copies
1. Defense Technical Information Center Cameron Station Alexandria, VA 22304-6145	2
2. Library, Code 52 Naval Postgraduate School Monterey, CA 93943-5002	2
3. Chairman (Code OC/Co) Naval Postgraduate School Monterey, CA 93943-5000	1
4. Chairman (Code MR/Hy) Naval Postgraduate School Monterey, CA 93943-5000	1
5. Dr. M. L. Batteen (Code OC/Bv) Naval Postgraduate School Monterey, CA 93943-5000	2
6. Dr. J. L. McClean (Code OC/Mn) Naval Postgraduate School Monterey, CA 93943-5000	1
7. LT R. T. Haines International Ice Patrol 1082 Shennecossett Rd. Groton, CT 06340	2
8. Commandant (G-PO-2) U.S. Coast Guard Washington, DC 20593	1
9. Dr. T. Kinder Physical Oceanography Division Office of Naval Research 800 N. Quincy Street Arlington, VA 22217	1

- |     |  |   |
|-----|--|---|
| 10. | Dr. L. Goodman<br>Physical Oceanography Division<br>Office of Naval Research<br>800 N. Quincy Street<br>Arlington, VA 22217  | 1 |
| 11. | Dr. M. Fiadeiro<br>Physical Oceanography Division<br>Office of Naval Research<br>800 N. Quincy Street<br>Arlington, VA 22217 | 1 |
| 12. | Superintendent (ds)<br>U.S. Coast Guard Academy<br>15 Mohegan Avenue<br>New London, CT 06320-4195                            | 1 |
| 13. | Library<br>Marine Biological Laboratory<br>Woods Hole, MA 02543  | 1 |
| 14. | Library<br>Moss Landing Marine Lab<br>P.O. Box 450<br>Moss Landing, CA 95039   | 1 |
| 15. | Library<br>Monterey Bay Aquarium Research Institute<br>160 Central Avenue<br>Pacific Grove, CA 93950                         | 1 |















DUDLEY KNOX LIBRARY  
NAVAL POSTGRADUATE SCHOOL  
MONTEREY, CA 93943-5101



DUDLEY KNOX LIBRARY



3 2768 00307507 8